Modeling Deformations of Active Rods, Ribbons, and Plates

Thesis by
Kevin Andreas Korner

In Partial Fulfillment of the Requirements for the
Degree of
Doctor of Philosophy in Mechanical Engineering

CALIFORNIA INSTITUTE OF TECHNOLOGY
Pasadena, California

2022
Defended July 8, 2022

Kevin Andreas Korner
ORCID: 0000-0002-2967-9657

ACKNOWLEDGEMENTS

First and foremost, I would like to thank my advisor, Kaushik Bhattacharya. He has been an inspiration and molded my perspective on mechanics and engineering. He truly embodied the role of an advisor as he pushed me to develop my own thoughts and abilities in order to make me a better, more well rounded researcher. I am grateful for all the knowledge and experience I have gained under Kaushik's advisement.

I would also like to thank my thesis committee: Ruby Fu, Michael Ortiz, and Nadia Lapusta. I am grateful to Ruby for serving on my committee contributing some very insightful questions to my thesis. Over the years I have worked closely with Michael and Nadia in various capacities and I have learned so much about research, teaching, and leadership. Michael always provides thought-provoking discussions and helpful insights during our group meetings. Nadia is truly a figurehead of the department and always inspires me to be more involved.

I would like to extend a huge thank you to the professors at UC Berkeley who inspired me to study the field of continuum mechanics. Oliver O'Reilly and James Casey taught me that engineering could be approached from a much more rigourous perspective and introduced me to much of the topics that I continued to work on in my thesis.

I have been fortunate to work with some excellent collaborators while exploring various topics in slender structures. Basile Audoly was instrumental in teaching me different ways of looking at elastic structures and some of the math involved. My experimental collaborators, such as Alexa Kunstler, Tayler Hebner, Ryan Hayward, Chris Bowman, and Tim White were also incredibly helpful in understanding the true physics of these materials outside of the model. Their practical insight has been extremely useful when studying and developing computational models for active structures.

I gratefully acknowledge the support of the US Office of Naval Research through the MURI grant ONR N00014-18-1-2624. This grant introduced me to a wide variety of researchers from different universities and fields and truly broadened my horizons. In addition, the support of the National Science Foundation Graduate Research Fellowship under Grant No. DGE-1745301 has been extremely helpful in giving me the freedom to research my own interests.

I would like to thank all the members of the Bhattacharya/Ravichandran/Ortiz group for the countless discussions and collaborations through the years, such as Andrew Akerson, Eric Ocegueda, Vatsa Gandhi, Leah Ginsberg, Akshay Joshi, Tomoyuki Oniyama, Jack Weeks, Aakila Rajan, Sathvik Sanagala, Hao Zhou, Ying Shi Teh, Sharan Injeti, Victoria Lee, Paul Mazur, Louisa Avellar, Jin Yang, Paul Plucinsky, Lincoln Collins, Dingyi Sun, Suraj Ravindran, Jean-Michel Scherer, Neda Maghsoodi, Ruobing Bai, Swarnava Ghosh, and Stella Brach. A few colleagues I would like to thank in particular are Paul Plucinsky, Will Schill, Andrew Akerson, and Ruobing Bai for the help and support, especially when my code breaks.

I would also like to thank my friends, both from Caltech and outside. Ben Herren, Kathleen Kennedy, and Sydney Corona were great griends from early on at Caltech as we soldiered through our various courses. Hannah Broido and Andjelija Beukman are some of my closest friends and always attempted to get me to see that a world outside of academia exists.

The admins, especially Jenni Campbell, Lynn Seymour, and Stacie Takase have been instrumental in making the department an amazing place and making sure that the whole department doesn't fall into chaos. Additionally, SOPS (Society of Professional Students) has contributed to improving the department in so many ways, particularly Will Schill, Marcus Lee, Victoria Lee, Leah Ginsberg, Alex Choi, Ellande Tang, and Prithvi Akella.

I would also like to extend lots of love and appreciation to my family: Christian, Wania, and Stephan Korner, for the unwavering support for as long as I can remember and always pushing me to pursue my goals. I would not be the person I am today without any of them.

Finally, my girlfriend, Lua Varner, has been incredibly loving and supportive throughout my PhD. We always find fun places to experience and have had many incredible trips together. I couldn't have asked for anyone better to spend my life with, especially while locked together during Covid.

ABSTRACT

Slender structures are mechanical components which have at least one spatial dimension much smaller than another. Some canonical examples are beams, rods, ribbons, plates, and shells. Although these systems have been studied for many centuries, the focus of development has generally been limited to small strains and the onset of buckling modes. Outside of this regime, both geometric and material non-linearities contribute significant complexity to the analytical and computational techniques which can be applied to these problems. Despite this, large deformations demonstrate tremendous potential in engineering applications, particularly with soft materials. This thesis examines various methods of modeling slender structures. We focus on large strain behaviors, often accentuated by spontaneous strains generated with active materials. These systems demonstrate a wide range of interesting and useful behaviors, such as bifurcations, snap-through, and cyclic deformations.

A particular focus of this thesis is slender structures made of liquid crystal elastomers. These are elastomers embedded with nematic mesogens that undergo temperature-induced phase transitions accompanied by large spontaneous strain. By embedding photo-reactive molecules, like azobenzene, in these materials, it is possible to make these materials deform by light.

Rolling and flapping behaviors of beams of photo-reactive liquid crystal elastomers have been demonstrated through experimental works. We derive an equation for the evolution of spontaneous curvature in the presence of illumination, then use that to investigate various configurations of photo-mechanical beams. We demonstrate rolling, flapping, and a triggered snap-through computationally and demonstrate consistency with experimental work.

We then study large deformations of beams and ribbons. In order to do so, we develop a novel computational method which builds on the discrete elastic formulation. We define discrete deformation measures which directly calculate the strain gradient. This formulation has the benefit of having explicit first and second derivatives, allowing for efficient calculation of the gradient and hessian. We use this to study a variety of different physical systems, from a twisting pseudo-ribbon, the folding of an overcurved ring, and the shape of a Möbius strip. Each of these systems is formulated using the methods described in the manuscript and compared to external data.

Plates of liquid crystal elastomers also demonstrate strange phenomena. In particular, we discover a configuration of laminated sheets which, when placed on a hot plate, jumps many times the thickness of the sheet. We identify the mechanism of the jump to be the transience of heat absorption through the thickness and interaction with the varying spontaneous stretches. In order to model this system, we develop numerical methods which naturally allows for inclusion of energies with second derivatives. Experimental work is used to corroborate the computational findings and explore the design space.

PUBLISHED CONTENT AND CONTRIBUTIONS

[1] Kevin Korner, Basile Audoly, and Kaushik Bhattacharya. "Simple deformation measures for discrete elastic rods and ribbons". In: *Proceedings of the Royal Society A* 27 (Dec. 2021), pp. 1–63. ISSN: 1364-5021. DOI: 10.1098/RSPA.2021.0561. URL: https://royalsocietypublishing.org/doi/abs/10.1098/rspa.2021.0561.
K.K. helped design the research, formulated the theory, performed computation, analyzed data, and helped write the manuscript.

[2] Kevin Korner et al. "A nonlinear beam model of photomotile structures". In: *Proceedings of the National Academy of Sciences* (Apr. 2020). ISSN: 0027-8424. DOI: 10.1073/PNAS.1915374117. URL: https://www.pnas.org/content/early/2020/04/15/1915374117.
K.K. helped design the research, formulated the theory, performed computation, analyzed data, and helped write the manuscript.

TABLE OF CONTENTS

LIST OF ILLUSTRATIONS

LIST OF TABLES

Chapter 1

INTRODUCTION

> "*For almost two centuries, the primary motivation underlying developments in rods, plates and shells derived from the need to have quantitative methods to analyse man-made structures—buildings, bridges, dams, aircraft, etc. As a consequence, there was relatively little motivation to understand problems involving dramatic geometry changes such as a rod curling about itself or a hemispherical shell turned inside out. Such behavior falls well outside the envelope of permissible deformations for conventional structures. Thus, while non-linear geometry does play an important role in the buckling of conventional structures, the research focus was almost always directed to questions such as the maximum load-carrying capacity of a structure and not, for example, its collapsed shape. And, usually, the shape at maximum load differs only slightly from the initial shape. In recent decades, new motivations began surfacing in fields such as bio-physics and bio-mechanics where extreme deformation shapes and patterns constitute normal behavior. Nature is replete with examples, at the molecular scale and above.*" John Hutchinson in the Forward to [1]

This quote perfectly describes the goal of this work. Slender structures demonstrate tremendous potential in the areas of medicine, soft robotics, and mechanics due to their ability to undergo large, reversible deformations well outside of the linear regime; however, this brings complexity. Some of complexity is the inherent geometric non-linearity of such systems, the dependence of the energy on curvatures, and non-convex energy landscapes that present multiple solutions. The goal of this manuscript is to develop methods to study the complex behaviors of slender engineering structures, particularly systems that evolve with spontaneous strains and curvatures. We explore various types of slender structures and discuss their behaviors, such as bifurcations and snap-through instabilities. This work utilizes a variety of methods when discussing and analyzing slender structures as the the methods developed are theoretical, computational, and (through collaboration) experimental. The models and methods developed and utilized in this work greatly expands our ability to study slender structures and deploy them in practical engineering systems.

1.1 Slender structures

Slender structures, such as those described in the previous statement, can generally be described as systems where at least one spatial dimension is much smaller than the others. In two dimensions, this describes beams, where the length of the beam is vastly greater than the width of the beam. One way to write this is $L_1 \ll L_2$, where L_1 and L_2 represent the length scales along different dimensions of the system. This states that the body of the system will have one dimension that is small compared to another.

In three dimensions, there are more ways this dimensional discrepancy can be realized. If two of the dimensions are small compared to the third, i.e. $L_1 \approx L_2 \ll L_3$, we arrive at descriptions of rods. These follow the theory of elastica, and there is a rich history in the study of such systems dating back to the 13th century [2] and has been worked on by many, including Galileo, the Bernoullis, and Euler. The study of elastica was fundamental in the development of mathematics and mechanics.

If one of the dimensions is small compared to the other two, $L_1 \ll L_2 \approx L_3$, we describe this as a membrane, plate, or shell. A membrane is generally when the thin dimension is so small that we can generally neglect energetic contributions of bending. Systems where the bending energy/forcing plays a role are referred to as a plate or a shell. A plate is generally when the stress-free or reference configuration is a flat plane and a shell is when it is curved. All three of these exhibit a large range of interesting behaviors.

An additional type of structure is when $L_1 \ll L_2 \ll L_3$. In this case, we have three different orders of magnitude for length scale. The three different length scales allow for something that behaves somewhere in-between a rod and a sheet. One particular structure that satisfies this dimensional mismatch is a ribbon. Sadowsky [3] derived a 1D model of thin ribbons and Wunderlich [4] extended it to finite width. Both of these models pose the ribbon as a generalized elastica with a developability constraint. Dias et. al. [5] derived a model of ribbons from plate theories which permit for non-straight ribbons and incorporated effects such as striction, which is a common behavior in ribbons. The Möbius band, which is a ribbon that is inverted and closes in on itself, is a system that has long been studied as a quintessential example for ribbon theories.

Structural systems with dimensional mismatches demonstrate a particularly useful property that small strains can translate to extremely large deformations. This large deformation can then change the nature of the actuation conditions. This coupling

between deformation and its environment produces a non-linear effect which can be utilized to produce a variety of interesting behaviors.

The most promising way to generation deformation and movement in slender structures is to make them out of an active material itself. In contrast to traditional mechanical systems, where actuators and motors generate work and stiff structures provide rigidity, we can create more complex motions and tools by using the work-producing components as the structure itself. The most popular of these active materials are liquid crystal elastomers (LCE) which are easy to produce, demonstrate large, reversible deformations even at the local level, and can be tailored to specific applications.

1.2 Liquid crystal elastomers

Liquid crystals are generally long rodlike molecules, often refered to as mesogens, which demonstrate a steric interaction depending on its own properties and interaction with the environment. The classical way to control this material is by changing the temperature. At low temperatures, the mesogens tend to align, creating nematic order with a director described by a unit vector in $\mathbb{R}^3$. At high temperatures, thermal fluctuations drive a nematic-to-isotropic transition where the nematic order is lost and the mesogens become randomly oriented. There are also smectic, having a layered molecular structure, and cholesteric, having a twisted and chiral arrangement in some materials. Each of these forms has different properties.

An elastomer is a rubbery material composed of long chainlike molecures that are capable of recovering their original shape after being stretched to great extents. By embedding mesogens within the elastomer network (either along the main chain or attached as a side chain), we can combine the properties of liquid crystals with elastomers, creating a new class of material. *Liquid crystal elastomers* were originally envisioned in by P-G. de Gennes as he asked whether topological properties of liquid crystals can be added into a conventional crosslinked polymer [6].

Nematic liquid crystal elastomers are generally studied due to their nematic-to-isotropic transition. As stated before, the liquid crystals can spontaneously reorient themselves due to a change in local environment. When embedded in the elastomer network, this reorientation can cause spontaneous strains aligned with the nematic director direction, as shown in Figure 1.1. Although this transition has traditionally been controlled by changing the temperature, other triggers can be used.

This nematic-to-isotropic transition can occur due to changes in temperature [7] and

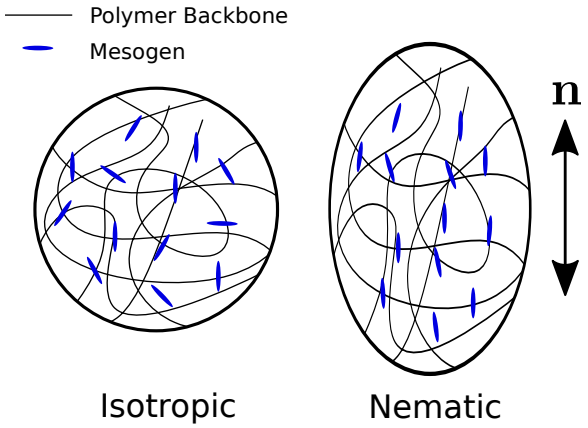

Figure 1.1: Illustration of a liquid crystal elastomer. The polymer backbone provides the elasticity while the mesogens maintain their liquid crystal behavior. The combination of these effects allows for behaviors such as a shape memory effect and very large deformations. The nematic state has a directional order in direction **n**.

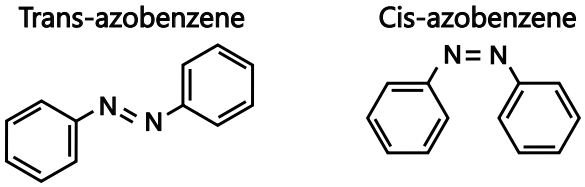

Figure 1.2: Molecular structure of Azobenzene in the trans and cis phases.

even stress [8, 9]. Additionally, we can embed other molecules within the system to induce the phase transition. One particular method of interest, as demonstrated in [10, 11, 12], is to include azobenzenes in the mix. Azobenzene is a molecule which has two main conformations, a trans (long and rodlike) and a cis phase (kinked). The molecular structure of azobenzene in both phases is given in Figure 1.2. In the low energy state, the molecule is in the trans state, and, when given a sufficient energetic impulse, such as a photon, the molecule kinks and transforms into a cis state. By embedding these molecules in tandem with the liquid crystal elastomer network, the transition from trans to cis converts the azobenzene molecule from a mesogen to a dopant. When in the trans phase, the azobenzene acts as a mesogen. Therefore, by shining light onto the LCE, the azobenzene transforms into the cis form (acting as a dopant) and disrupts the nematic order of the elastomer, thus inducing the nematic-to-isotropic transition, and changing the shape of the underlying material as a result. Light as an actuation mechanism presents significant benefits: objects can

be actuated from a distance, distinct frequencies can be used to actuate and control distinct modes with minimal interference, and significant power can be transmitted over long distances through corrosion-free, lightweight fiber optic cables.

1.3 Bifurcations and snap-through instability

Bifurcations are a long studied phenomenon that was first studied when looking at the nature of solutions of differential equations. A bifurcation occurs when a small smooth change to a system parameter causes a sudden "qualitative" or topological change in its behavior [13]. This sudden change in behavior can be studied and utilized in complex engineering systems.

We may have a situation where the equilibrium equation

$$\delta U(\bar{y}, \lambda) = 0$$

has multiple solutions $\bar{y}$ depending on the parameter λ, where U is the potential energy functional for the system. Bifurcations describe the situation where a solution branch $\bar{y}(\lambda)$ either (a) loses stability or (b) bifurcates into multiple branches at a particular value of λ.

Slender structures often bifurcate. The traditional studies focussed on the critical values of λ where the bifurcation occurs by examining the positive-definiteness of the Hessian $\delta^2 U(\bar{y}(\lambda), \lambda)$ along a solution branch; however, current interest is in understanding all the solution branches.

Generally, solutions track a particular solution branch, as a result, and can be caught in local minima. This means that, despite lower energy solutions existing, the demonstrated solution may track a minimizer which does not have the lowest possible energy. Because of this, we generally want to find the minimizer of U which is "close" to some initial guess. For systems which evolve in time, this is generally the previous time step's solution. Therefore, given an initial solution, we can use a descent algorithm in order to converge to the closest local minimizer. In principle, the algorithm should not matter, however, methods such as random sampling or large initial step sizes may lead to jumps outside of the local energy well and into a different solution branch.

Snap-through instability

Due to non-linearities in a mechanical system, multiple energy minimizers may exist, as discussed above. This multi-stability can arise from many different effects

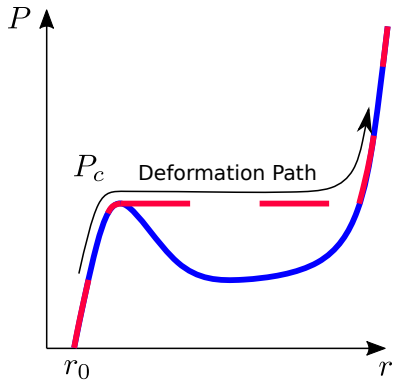

Figure 1.3: Pressure versus radius for a balloon made of hyperelastic material. The red dashed line shows the deformation pathway with the arrow showing the loading direction.

such as geometric or material properties. In many cases, the different solutions may be symmetry related, however this is not a requirement.

Snap-through events occur when the solution to a dynamical system rapidly passes from one solution variant to another. In a quasi-static system, this change occurs instantaneously. This can occur either due to some external forcing or changing parameter set which causes one configuration to become unstable. An example of such a system is with a rubber balloon.

Consider a rubber balloon comprised of a hyperelastic material loaded by increasing the pressure inside the balloon. By solving for the relation between radius and pressure, we can characterize the response of the system. Initially, pressure increases as a function of radius. Eventually, there is an inflection and the pressure for a particular radius begins to decrease (see Figure 1.3). At significantly higher stretches, the pressure rapidly increases due to strain-stiffening. What we see from this is that at any set pressure, there are three potential radii where the radius is at a stationary point. In practice, we start from the low pressure and increase it slowly. Once the radius and pressure hit the critical point (P_c), the radius of the system will very rapidly jump to the highest radius of the three solutions (assuming that we can supply air infinitely fast to maintain the pressure).

The rapid deformation due to instability leads to large energy releases in a short amount of time and allow for generation of work and movement. One example is the work in [14] on creating a liquid crystal elastomer pump utilizing this instability.

Another way to visualize the onset of a snap-through instability is to consider

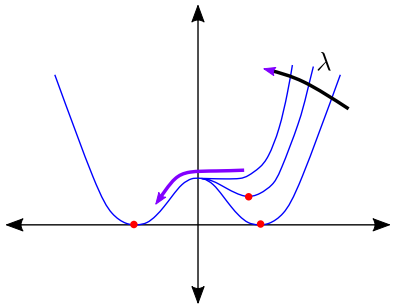

Figure 1.4: Diagram of a snap-through instability where a local minimizer can lose stability and snap through to another configuration. The purple arrow shows the motion of the solution into the new minimizer.

energies as shown in Figure 1.4. Initially, both minimizers are equally favorable, so let's consider being in the right energy well. By changing the parameter λ, we slowly skew the energy such that the well it is currently in becomes less favorable. Despite this, the configuration is locked into that energy well. When the parameter λ becomes large enough, the system becomes unstable and it will snap to the other energy minimizer. This demonstrates how a snap-through can be tied to the parameter λ.

We can also see from Figure 1.4 that the energy difference from before and after the snap can be quite substantial. This rapid transition in energy can be extremely useful because we can slowly accumulate energy over time and release it rapidly.

Pitchfork Bifurcation

One particular bifurcation of interest is the pitchfork bifurcation. This can be identified by a transition from a single stable state, to multiple stable states. The normal form of this type of bifurcation is the differential equation

$$\frac{dx}{dt} = \mu x - x^3 \, .$$

By expanding this equation, we can see that we have three fixed points ($dx/dt = 0$) at $x = 0, \pm\sqrt{\mu}$. From this we can see that there is a transition from a singular solution of $x = 0$ when $\mu < 0$ (as we are not considering imaginary solutions) to three solutions when $\mu > 0$. By conducting a linear stability analysis we can evaluate the stability at all the fixed points. By setting $f(x) = \mu x - x^3$, and looking at the value of the derivative ($df/dx = \mu - 3x^2$) at the fixed points in Table 1.1

Fixed Point	df/dx
$x = -\sqrt{\mu}$	-2μ
$x = 0$	μ
$x = \sqrt{\mu}$	-2μ

Table 1.1: Stability of the fixed points of the pitchfork bifurcation in its normal form.

For this notion of linear stability, we require that $df/dx < 0$. Here we see that for $\mu < 0$, we have one fixed solution $x = 0$. For $\mu > 0$, the solution at $x = 0$ becomes unstable and the two new solutions, $x = \pm\sqrt{\mu}$ become stable. This simple model demonstrates a bifurcation where the set of solutions transforms from a single, stable solution to multiple, stable solutions.

This type of bifurcation is prevalent in the study of sheets with spontaneous in-plane strains and curvatures. Initially, only a flat configuration is stable. Then, with spontaneous stretching and curvature, multiple stable states can be realized. Addtionally, even though the stable states might not have the same potential energy (i.e. there exists one prefered state), the system can be pushed between the states and lock in higher energy modes.

1.4 Organization of Thesis

Chapter 2.2 provides a brief introduction on modeling reduced dimensional structures. This background is helpful to introduce some basic concepts in the fields of rods and plates in order to contextualize the discussions later in the manuscript.

In Chapter 3 we study various configurations of a photomechanical beam being activated by light in various configurations. We develop a local model for the interaction between light and curvature evolution. Using this, we study a circular ring and a doubly clamped beam made of photo-mechanical material. These particular systems demonstrate strange and interesting behaviors. We study these systems for various lighting conditions in order to characterize their response and compare to the experimental literature.

Chapter 4 reformulates the theory of discrete elastic rods by defining a set of discrete deformation measures which are directly related to the continuous deformation measures, compact, and generic to any set of rods. We describe the new strain measures and develop a computational system revolving around these structures. We then use this method to study a variety of rod problems. These range from confirming buckling loads, overcurved rings, stretching ribbons, and the configuration of a

Möbius strip.

In Chapter 5, we study a particular example of LCE sheets where, by designing the through-thickness anisotropy, the sheet will deform in such a way that the sheet will self-induce a snap-through instability and leap off the surface. This is done by layering LCE sheets of varying moduli. The time dependent heat transfer of through the thicness of the sheet creates a deformation pathway which induces an instability, releasing large amounts of energy in short time frames. We model this system by developing an effective model for the spontaneous in-plane strain and curvature due to anisotropic stretch through the thickness, taking into account the potential for dramatically different material properties. Then, using a Föppl-von Karman plate model, we solve for equilibrium behaviors in order to characterize their response.

We summarize the results and findings of this thesis in Chapter 6, followed by a discussion of various possibilities for future avenues of research.

Chapter 2

OVERVIEW OF ROD AND SHEET MODELS

In order to aid in the discussion of the following chapters, it is beneficial to discuss the some classical descriptions of slender structures. In this section we focus on developing a rod model. We then discuss a variational approach to introduce variations, allowing us to find the Euler-Lagrange equations. We follow this with a discussion of the Föppl-von Kármán plate model.

2.1 Beams/Rod theories

A beam or a rod is a body where one space dimension is much greater in length in the two other perpendicular directions. We say 'beam' when the body is confined to a plane and say 'rod' when it is not; so a beam is a special case of a rod. The theory of finite displacements of thin rods has been developed by Kirchhoff and Clebsch; for a detailed historical discussion of this derivation, see the paper by Dill [15]. The theory of rods has seen widespread adoption into engineering applications and a vast variety of fields, from engineering structures, to sub-oceanic cables [16], to DNA [17], to climbing plants [18].

Modern approaches utilize both the center line ($\mathbf{x}(S)$) information together with a set of material frames ($\mathbf{d}_i(S)$), often called Cosserat curves, to describe the deformation and orientation of a curve. For the following discussion, we will generally assume inextensible and unshearable rod. We choose the orientation of the frames in a way that $\mathbf{d}_1$ and $\mathbf{d}_2$ describe the cross-section of the rod, and $\mathbf{d}_3$ is tangent to the

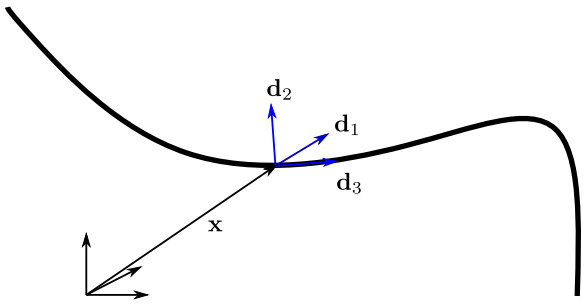

Figure 2.1: Diagram of rod in 3D space. The centerline is given by $\mathbf{x}$ and the directors are $\mathbf{d}_i$ (in blue). The tangent of the centerline is aligned with $\mathbf{d}_3$.

centerline curve as shown in Figure 2.1.

These frames are often constructed such that they remain orthonormal at each S and thus, form a basis at each point. This is known as the Euler-Bernoulli, or Navier-Bernoulii kinematic hypothesis. This condition of orthonormality gives the following relations:

$$\begin{aligned}\mathbf{d}_i'(S)\cdot\mathbf{d}_i(S) &= 0\\ \mathbf{d}_i'(S)\cdot\mathbf{d}_j(S) &= -\mathbf{d}_j'(S)\cdot\mathbf{d}_i(S)\,,\end{aligned}$$

where $(\cdot)' = \dfrac{d(\cdot)}{dS}$. The combination of these two conditions allows us to define an axial vector, also known as the Darboux vector, $\boldsymbol{\kappa}(S)$ such that

$$\mathbf{d}_i'(S) = \boldsymbol{\kappa}(S)\times\mathbf{d}_i(S)\,.$$

Projecting $\boldsymbol{\kappa}$ onto the $\mathbf{d}_i$ basis, we have $\boldsymbol{\kappa}(S) = \kappa_1(S)\mathbf{d}_1(S)+\kappa_2(S)\mathbf{d}_2(S)+\kappa_3(S)\mathbf{d}_3(S)$. Intuitively, κ_1 and κ_2 a are measures of how much the cross section rotates about $\mathbf{d}_1$ and $\mathbf{d}_2$, respectively. These are commonly referred to as bending terms. κ_3 is a measure of the twist (or rather twisting rate) of the rod.

Tracking the orientation of the cross section is extremely important because the rotation of the frame is integral in defining deformation measures which contribute to the energy of the rod. As the components κ_i measure the change in orientation of the rod, they can be seen as the strain/deformation measures for the system.

Given the strain measures, we can begin to define energetic quantities associated with the rod. In the case of the classic Kirchhoff rod, the energy takes the form

$$\mathcal{E}_{\mathrm{K}} = \frac{1}{2}\int_0^L \left(EI_1\kappa_1(S)^2 + EI_2\kappa_2(S)^2 + \mu J\kappa_3(S)^2\right)dS\,,$$

where E is the Young's modulus of the material, I_i are the area moments of inertia, μ is the shear modulus, and J is the polar moment of inertia. This form is a consequence of using a Hookean material model.

For the general case, we can extend the study to systems which are not simply Kirchhoff rods. In order to do so, we introduce a local strain energy function w such that

$$\mathcal{E} = \int_0^L w(\kappa_i(S))dS\,.$$

The function w calculates the stored energy per unit length. By changing the form of w, we can change the physics of the problem we are trying to solve. We will

see examples of this later in the manuscript where we study behaviors of rods with various constitutive models for rods. For static equilibrium problems, we find solutions by minimizing the potential energy of the rod where

$$U = \mathcal{E} - W\,,$$

where W is the work due to external forces.

Variations

We take a variational approach to calculate minimizers of the elastic energy. We consider arbitrary perturbations denoted by the symbol δ. The variation of the potential energy is then given by

$$\delta U = \delta\mathcal{E} - \delta W\,.$$

We can find the variation of the elastic energy as

$$\delta\mathcal{E} = \int_0^L \frac{\partial w}{\partial \kappa_i}(\kappa_i(S))\delta\kappa_i dS\,,$$

where there is implicit summation over the i index. One convenient way to write this is by defining the internal moment as $\mathbf{M}(s) = \dfrac{\partial w}{\partial \kappa_i}(\kappa_i(S))\mathbf{d}_i(S)$ and substituting to get

$$\delta\mathcal{E} = \int_0^L \mathbf{M}(S)\cdot(\delta\kappa_i\mathbf{d}_i)\,dS\,. \tag{2.1}$$

Now, consider a variations with respect to the director field. We have

$$\delta\mathbf{d}_i = \delta\boldsymbol{\phi}\times\mathbf{d}_i\,,$$

where $\delta\phi = \delta\phi_i\mathbf{d}_i$. In order to arrive at this form, we use the same argument as for defining the derivative of the director field. Now, we must relate perturbations to the material frame to the perturbations in the curvature components we found earlier. We do this by noticing that derivatives of the perturbation are equal to perturbations of the derivative:

$$\begin{aligned}
\delta(\mathbf{d}_i') &= (\delta\mathbf{d}_i)'\\
\delta(\boldsymbol{\kappa}\times\mathbf{d}_i) &= (\delta\boldsymbol{\phi}\times\mathbf{d}_i)'\\
\delta\boldsymbol{\kappa}\times\mathbf{d}_i + \boldsymbol{\kappa}\times(\delta\boldsymbol{\phi}\times\mathbf{d}_i) &= \delta\boldsymbol{\phi}'\times\mathbf{d}_i + \delta\boldsymbol{\phi}\times(\boldsymbol{\kappa}\times\mathbf{d}_i)\,.
\end{aligned}$$

Using the Jacobi identity and noting this is true for all i, we arrive at

$$\delta\boldsymbol{\kappa} - \delta\boldsymbol{\phi}\times\boldsymbol{\kappa} = \delta\boldsymbol{\phi}'\,.$$

This equation provides a compatibility condition between perturbations to the material frame and perturbations to the curvatures. Expanding the left hand side of this equation, we have

$$\delta\kappa_i \mathbf{d}_i + \delta\boldsymbol{\phi} \times \boldsymbol{\kappa} - \delta\boldsymbol{\phi} \times \boldsymbol{\kappa} = \delta\kappa_i \mathbf{d}_i \,.$$

Using this result in the variation of strain energy in Equation 2.1, we have

$$\delta\mathcal{E} = \int_0^L \mathbf{M}(S) \cdot \frac{d\boldsymbol{\phi}}{dS}(S) dS \,.$$

Using integration by parts, we can move the derivative to the moment as

$$\delta\mathcal{E} = [\mathbf{M}(S) \cdot \delta\boldsymbol{\phi}(S)]_0^L - \int_0^L \mathbf{M}(S)' \cdot \delta\boldsymbol{\phi}(S) dS \,,$$

where the bracket notation indicates evaluation of these functions at the boundaries.

Variations in the work done by external forces takes the form

$$\begin{aligned}\delta W =& \mathbf{P}(0) \cdot \delta\mathbf{x}(0) + \mathbf{Q}(0) \cdot \delta\boldsymbol{\phi}(0) + \mathbf{P}(L) \cdot \delta\mathbf{x}(L) + \mathbf{Q}(L) \cdot \delta\boldsymbol{\phi}(L) \\ &+ \int_0^L \left(\mathbf{p}(S) \cdot \delta\mathbf{x}(S) + \mathbf{q}(S) \cdot \delta\boldsymbol{\phi}(S)\right) dS \,,\end{aligned}$$

where $\mathbf{P}$ and $\mathbf{p}$ are the end and distributed forces, respectively, and $\mathbf{Q}$ and $\mathbf{q}$ are the end and distributed moments, respectively.

A complication is that we must satisfy that the tangent to the center line is aligned with $\mathbf{d}_3$. As before, this is written as $\mathbf{x}'(S) = \mathbf{d}_3(S)$. Integrating this gives

$$\mathbf{x}(S) = \mathbf{x}(0) + \int_0^S \mathbf{d}_3(S') dS' \,.$$

Taking the variation, we have

$$\delta\mathbf{x}(S) = \delta\mathbf{x}(0) + \int_0^S \delta\mathbf{d}_3(S') dS' = \delta\mathbf{x}(0) + \int_0^S \delta\boldsymbol{\phi}(S') \times \mathbf{d}_3(S') dS' \,.$$

By using this expression with the variation in work, we obtain

$$\begin{aligned}\delta W =& (\mathbf{P}(0) + \mathbf{F}(0)) \cdot \delta\mathbf{x}(0) + \mathbf{Q}(0) \cdot \delta\boldsymbol{\phi}(0) + \mathbf{Q}(L) \cdot \delta\boldsymbol{\phi}(L) \\ &+ \int_0^L (\mathbf{q}(s) + \mathbf{d}_3 \times \mathbf{F}(S)) \cdot \delta\boldsymbol{\phi}(S) dS \,,\end{aligned}$$

where

$$\mathbf{F}(S) = \int_s^L \mathbf{p}(S') dS' + \mathbf{P}(L) \,.$$

A more common way to write this expression is by taking the derivative as

$$\mathbf{F}'(S) + \mathbf{p}(S) = 0\,.$$

This expression is commonly known as the balance of forces.

Combining this expression with the variation in strain energy, we can get an expression for the variation of potential energy, which we set equal to zero as

$$\begin{aligned} 0 = &- \int_0^L \mathbf{M}(S)' \cdot \delta\boldsymbol{\phi}(S) dS - (\mathbf{P}(0) + \mathbf{F}(0)) \cdot \delta\mathbf{x}(0) - (\mathbf{Q}(0) + \mathbf{M}(0)) \cdot \delta\boldsymbol{\phi}(0) - (\mathbf{Q}(L) \\ &- \mathbf{M}(L)) \cdot \delta\boldsymbol{\phi}(L) - \int_0^L (\mathbf{q}(s) + \mathbf{d}_3 \times \mathbf{F}(S)) \cdot \delta\boldsymbol{\phi}(S) dS\,. \end{aligned} \tag{2.2}$$

Using the Fundamental Theorem of the Calculus of Variations (i.e. the perturbations $\delta\boldsymbol{\phi}$ are arbitrary and thus the integrand must equal zero), we arrive at the strong form of our equilibrium equations

$$\frac{d\mathbf{M}}{dS}(S) + \mathbf{d}_3(S) \times \mathbf{F}(S) + \mathbf{q}(S) = 0\,, \tag{2.3}$$

known as the balance of moments equation.

The boundary conditions for this system of equations can be found by inspection of Equation 2.2. Consider the case where the boundary is free to move at $S = 0$, then the space of perturbations includes perturbations at the boundary. Therefore, $\delta\mathbf{x}(0)$ is arbitrary, giving the condition that

$$\mathbf{P}(0) + \mathbf{F}(0) = 0\,.$$

If the boundary is free to rotate, then we have that $\delta\boldsymbol{\phi}(0)$ is arbitrary and thus

$$\mathbf{Q}(0) + \mathbf{M}(0) = 0\,.$$

By making similar arguments at both boundaries, the proper boundary conditions can be found.

Summary

The above discussion demonstrates how to derive and interpret the equations of equilibrium for a generalized rod. To summarize, we have

$$\begin{aligned} \mathbf{F}'(S) + \mathbf{p}(S) = 0\,, \\ \mathbf{M}'(S) + \mathbf{d}_3(S) \times \mathbf{F}(S) + \mathbf{q}(s) = 0\,. \end{aligned} \tag{2.4}$$

In addition to the equations of equilibrium, we must recall the kinematic relations where

$$\begin{aligned}\mathbf{d}_i'(S) &= \boldsymbol{\kappa}(S) \times \mathbf{d}_i(S)\,,\\ \mathbf{d}_3(S) &= \mathbf{x}'(S)\,,\\ \mathbf{M}(S) &= \frac{\partial w}{\partial \kappa_i}(\kappa_j(S))\mathbf{d}_i(S)\,.\end{aligned}$$

Beam theory

As mentioned previously, beam theories are a special case of rod theories where the deformation is assumed to exist only in the plane. In this case, the formulation simplies quite drastically. Recall the definition of the Darboux vector as $\mathbf{d}_i'(S) = \boldsymbol{\kappa}(S) \times \mathbf{d}_i(S)$. If we consider planar deformations, then deformations will be limited to the $\mathbf{e}_1$, $\mathbf{e}_3$ plane (where $\mathbf{e}_i = \mathbf{d}_i(0)$). Note that this gives

$$0 = \mathbf{d}_2(S)\cdot\mathbf{d}_1'(S) = \mathbf{d}_2(S)\cdot(\boldsymbol{\kappa}(S)\times\mathbf{d}_1(S)) = \boldsymbol{\kappa}(S)\cdot(\mathbf{d}_1(S)\times\mathbf{d}_2(S)) = \boldsymbol{\kappa}(S)\cdot\mathbf{d}_3(S) = \kappa_3(S)$$

$$0 = \mathbf{d}_2(S)\cdot\mathbf{d}_3'(S) = \mathbf{d}_2(S)\cdot(\boldsymbol{\kappa}(S)\times\mathbf{d}_3(S)) = \boldsymbol{\kappa}(S)\cdot(\mathbf{d}_3(S)\times\mathbf{d}_2(S)) = -\boldsymbol{\kappa}(S)\cdot\mathbf{d}_1(S) = -\kappa_1(S)\,.$$

This condenses the curvature vector down to a single component $\boldsymbol{\kappa}(S) = \kappa_2(S)\mathbf{d}_2(S)$. Noting that $\mathbf{d}_2'(S) = \boldsymbol{\kappa}(S) \times \mathbf{d}_2 = \kappa_2(S)\mathbf{d}_2(S) \times \mathbf{d}_2(S) = 0$, we can even further simplify the curvature vector as

$$\boldsymbol{\kappa}(S) = \kappa_2(S)\mathbf{e}_2 = \kappa(S)\mathbf{e}_2\,,$$

where the basis is now the fixed out-of-plane component. When considering the local strain energy function, we then have

$$w(\kappa) = w(0, \kappa, 0)\,,$$

because now, only one curvature matters.

We can also consider the forces. Since $\mathbf{p}$ lies only in the $\mathbf{d}_1$, $\mathbf{d}_3$ plane, we have that $\mathbf{F}$ also lies only in that plane. Plugging these into the moment balance equation and considering only the out-of-plane component, we have

$$M_2(S)' + F_1(S) + q_2(S) = 0\,,$$

where $M_2 = \mathbf{M} \cdot \mathbf{e}_2$, $F_1 = \mathbf{F} \cdot \mathbf{d}_1$, and $q_2 = \mathbf{q} \cdot \mathbf{e}_2$. Now, rather than having a system of equations, we have a single scalar-valued problem.

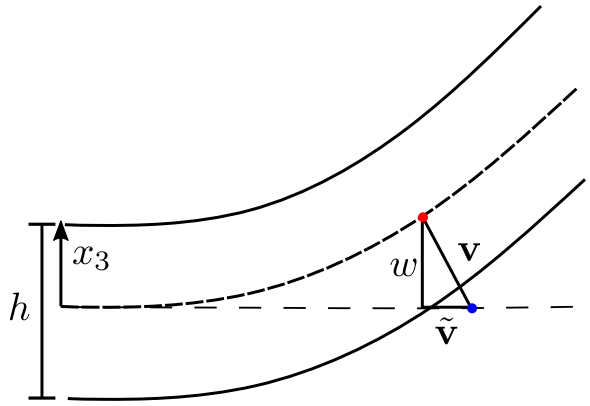

Figure 2.2: Diagram of the deflection of a plate for the Föppl-von Kármán plate model. The deflection of the mid-plane follows the decomposition $\mathbf{v}(x_\alpha) = \tilde{\mathbf{v}}(x_\alpha) + w(x_\alpha)\mathbf{e}_3$. The blue dot is the original location of a material point and the red dot is the location after the deformation.

2.2 Plate/Shell theories

For the sake of this manuscript, we will focus on the development and discussion of one particular plate model: the Föppl-von Kármán plate model. This veriation has a few particular advantages as it is valid for plates with substantial loading parallel to the plate as well as substantial out-of-plane displacements. The systems we study, capturing both these effects is essential to see the rich behavior of sheets.

Consider a plate like body whose thickness dimension h is much smaller than the other two. The mid-plane of the undeformed configuration is denoted by Ω. We will assume $\|\Omega\| \gg h$, there is a constant thickenss h, no in-plane loading, and out-of-plane loading is parallel to $x_3(z)$.

We define $w(x_\alpha)$ to be the vertical deflection and $\mathbf{v}$ to be the total deflection of the mid-plane of the plate. This decomposition can be found in Figure 2.2.

We make the kinematic assumption that $\mathbf{u}(x_i) = \mathbf{v}(x_\alpha) - x_3\nabla w(x_\alpha)$ where $\mathbf{v} = v_\alpha(x_\beta)\mathbf{e}_\alpha + w(x_\alpha)\mathbf{e}_3 = \tilde{\mathbf{v}}(x_\alpha) + w(x_\alpha)\mathbf{e}_3$ and ∇ indicates the gradient with respect to the in plane variables x_α. Latin indices indicate $1, 2, 3$ and Greek indices indicate $1, 2$. Calculating the deformation gradient associated with this ansatz, we have

$$\mathbf{F} = \mathbf{I} + \nabla\tilde{\mathbf{v}}(x_\alpha) + \mathbf{e}_3 \otimes \nabla w(x_\alpha) - x_3\nabla^2 w(x_\alpha) - \nabla w \otimes \mathbf{e}_3 \,.$$

For small strains but moderate rotations, we neglect terms higher order than $\|\nabla w(x_\alpha)\|^2$. We also make the additional assumption that the thickness of the

plate does not change. Using this, we can calculate the Lagrangian strain tensor ($\mathbf{E} = \frac{1}{2}(\mathbf{F}^T\mathbf{F} - \mathbf{I})$). We separate this into the in-plane components and the out-of-plane components as

$$\begin{aligned} E_{\alpha\beta} &= \frac{1}{2}(\tilde{v}_{\alpha,\beta} + \tilde{v}_{\beta,\alpha}) + \frac{1}{2}w_{,\alpha}w_{,\beta} - x_3 w_{,\alpha\beta}\,. \\ E_{i3} &= 0 \end{aligned}$$

For simplicity, we define $\epsilon_{\alpha\beta} = \frac{1}{2}(\tilde{v}_{\alpha,\beta} + \tilde{v}_{\beta,\alpha}) + \frac{1}{2}w_{,\alpha}w_{,\beta}$ so $\mathbf{E} = \boldsymbol{\epsilon} - x_3\nabla^2 w$.

Recall the strain energy of a 3D elastic body has the form

$$\mathcal{E} = \frac{1}{2}\int_\Omega \int_{-h/2}^{h/2} E_{ij}\mathbb{C}_{ijkl}E_{kl}dx_3 dA\,,$$

where $\mathbb{C}$ is the 4th order stiffness tensor. For our problem, we will assume that this tensor conforms to the plain-stress assumption. Recalling that all the out-of-plane components of our strain are equal to zero, we have

$$\mathcal{E} = \frac{1}{2}\int_\Omega \int_{-h/2}^{h/2} E_{\alpha\beta}\mathbb{C}_{\alpha\beta\gamma\delta}E_{\gamma\delta}dx_3 dA\,.$$

Plugging in our form of Lagrangian strain gives

$$\mathcal{E} = \frac{1}{2}\int_\Omega \int_{-h/2}^{h/2} \left(\epsilon_{\alpha\beta} - x_3 w_{,\alpha\beta}\right)\mathbb{C}_{\alpha\beta\gamma\delta}\left(\epsilon_{\gamma\delta} - x_3 w_{,\gamma\delta}\right)dx_3 dA\,.$$

Note that we can not integrate with respect to x_3 to arrive at

$$\mathcal{E} = \frac{1}{2}\int_\Omega \left(h\epsilon_{\alpha\beta}\mathbb{C}_{\alpha\beta\gamma\delta}\epsilon_{\gamma\delta} + \frac{h^3}{12}w_{,\alpha\beta}\mathbb{C}_{\alpha\beta\gamma\delta}w_{,\gamma\delta}\right)d\Omega\,.$$

If we define $W(\xi) = \frac{1}{2}\xi_{\alpha\beta}\mathbb{C}_{\alpha\beta\gamma\delta}\xi_{\gamma\delta}$, then note that we can write this energy in compact form as

$$\mathcal{E} = \int_\Omega \left(hW\left(\boldsymbol{\epsilon}\right) + \frac{h^3}{12}W(\nabla^2 w)\right)dA\,,$$

where $\boldsymbol{\epsilon} = \frac{1}{2}\left(\nabla\tilde{\mathbf{v}} + \nabla\tilde{\mathbf{v}}^T\right) + \frac{1}{2}\nabla w \otimes \nabla w$. This strain captures the effective strain of the mid-surface with contributions from the out-of-plane deformation. These components become very important when considering large rotations of the midplane. The second term involving second derivatives of w capture the energetic contribution of curvature as flexural or bending strains.

Chapter 3

LIGHT GENERATED DEFORMATIONS OF PHOTOMECHANICAL BEAMS

The work presented in this chapter has been adapted from the following publication:

> Kevin Korner et al. "A nonlinear beam model of photomotile structures". In: *Proceedings of the National Academy of Sciences* (Apr. 2020). ISSN: 0027-8424. DOI: 10.1073/PNAS.1915374117. URL: https://www.pnas.org/content/early/2020/04/15/1915374117.

3.1 Introduction

A major challenge in soft robotics is the integration of sensing, actuation, control, and propulsion. In most soft robotic systems, propulsion and controls are enabled through a physical tether or complex on-board electronics and batteries. A tether simplifies the design but limits the range of motion of the robot, while on-board controls and power supplies can be heavy and can complicate the design [20]. Actuation by light through photomechanical processes directly converts photons to deformation and offers an attractive alternative. It can deliver energy remotely. Further, multiple frequencies can be used to actuate and sense different modes. Finally, if a tether is an option, then a significant energy can be delivered through corrosion-free and lightweight fiber-optic cables.

A further challenge arises in propulsion where one needs to generate cyclic motion. Since most actuation systems actuate one way, there is a need to reset the system [20]. To simplify the control process, it is desirable to do so by inherent response rather than by pulsing of the external source. Actuation by light is again attractive because one can use the directionality of the propagation of light. As the structure absorbs light and deforms, the conditions of illumination change, and this in turn changes the nature of further deformation. This coupling can be exploited in either closed structures or with structural instabilities to generate cyclic motion.

These advantages have motivated a recent body of work on developing photomechanical materials (see [21] for an extensive review). Much of this work has focussed on incorporating azobenzene photochromes that absorb light and transform between *cis* and *trans* configurations into liquid crystal elastomers whose orientational order

is coupled to deformation, following the pioneering work of Yu *et al.* [10]. These materials are typically synthesized as thin strips which bend when illuminated with light of appropriate frequency. Further, they can be combined with structural polymers to provide robustness [22].

Various works have demonstrated the ability to generate cyclic motion under steady illumination. Yamada *et al.* [23] demonstrated that a ring of liquid crystal elastomer (LCE) film containing azobenzene derivatives can roll in the presence of illumination. When wrapped around a series of pulleys, the film can be used as a light-driven plastic motor system. White *et al.* [24] developed a high frequency oscillator from a strip which bends under illumination sufficiently to block the light source and reset. Wei *et al.* [25] produced rolling motion in monolithic polymer films where ultraviolet-visible light transforms the film from flat sheets to spiral ribbons, which then rolls under continuous illumination. Finally, Gelebart *et al.* [22] created an oscillatory behavior of a doubly clamped LCE film.

Modeling light-mediated actuation is a complex multiphysics process involving three key elements: propagation and absorption of light, chemical transformation and temporal evolution of chromophores between states, and the nonlinear mechanics of structures undergoing large deformations. Corbett and Warner analyzed light absorption and actuation in azobenzene containing liquid crystal elastomers [26] and proposed a geometrical theory of illuminated thin strips [27]; this theory assumes that the stress in the strip remains zero, and is only applicable to the special case when the strips are unconstrained. While this model reveals various aspects of photo-actuation, it is unable to explain the cyclic behavior in the experiments above, where the constraints applied on the ends of strips, either through boundary conditions [22] or as a closed loop [23], give rise to internal stress.

In this chapter, we build on the work of Corbett and Warner [27] by coupling it to the mechanics of beams, and derive a fully coupled photo-activated mechanical model for thin illuminated strips which can handle arbitrary boundary conditions. Remarkably, a number of material, physical parameters—time-constants of photo-activation and relaxation, penetration depth, the elastic modulus and thickness of the strip and illumination intensity—collapse into a single non-dimensional parameter that governs the behavior. This highlights the flexibility that is available in the choice of material and structure in the development of light-activated structures. Our resulting model is simple and can be solved numerically in real time on any personal computer, while capturing a rich range of behaviors. We use it to address cyclic or

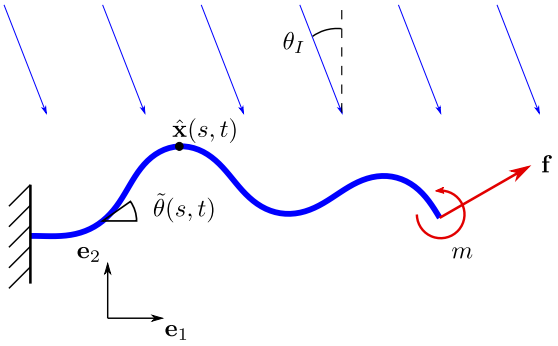

Figure 3.1: Elastica under illumination.

periodic motion under steady illumination and reveal the underlying mechanisms. The ability of this simple model to capture complex dynamics of light illuminated deformation make it a useful tool for the design and control of this novel type of structures.

3.2 Photo-deformable elastica

Consider an inextensible beam or a strip (planar elastica) subjected to illumination as shown in Figure 3.1. Let $\mathbf{x}(s,t)$ denote the position of centerline point s at time t and $\theta(s,t)$ denote the angle that the tangent to the beam makes with the horizontal axis $\mathbf{e}_1$. We assume that the deformation caused by illumination takes place over a significantly slower time scale than the natural periods of vibration of the beam so that we may assume that the beam is at equilibrium at all times. Therefore, at each t,

$$\frac{\partial \mathbf{f}}{\partial s}(s,t) = 0, \tag{3.1}$$

$$\frac{\partial m}{\partial s}(s,t) + (\widehat{\mathbf{t}}(s,t) \times \mathbf{f}(s,t)) \cdot \mathbf{e}_3 = 0\,, \tag{3.2}$$

where $\widehat{\mathbf{t}}(\theta(s,t)) = \partial \mathbf{x}/\partial s(s,t) = \cos\theta(s,t)\mathbf{e}_1 + \sin\theta(s,t)\mathbf{e}_2$ is the unit tangent, $\mathbf{f}(s,t)$ is the internal force transmitted across a cross-section, and $m(s,t)$ is the internal moment about $\mathbf{e}_3$.

Since we assume that the beam is inextensible and unshearable, the internal force $\mathbf{f}$ is constitutively indeterminate and we only need to specify a constitutive law for the moment m. Following Corbett and Warner [27], we assume that the beam is made of an elastic material whose spontaneous or stress-free strain, ε_0, changes with time depending on the local population of *cis* molecules. The longitudinal stress at a point at a position s along the length of the beam, z along the depth of the beam

and at time t is given by Hooke's law, $\sigma(s,z,t) = E(\varepsilon(s,z,t) - \varepsilon_0(s,z,t))$, where ε is the strain and ε_0 is the spontaneous strain. The moment is found by integration through the thickness as

$$m(s,t) = \int_{-h/2}^{h/2} E(\varepsilon(s,z,t) - \varepsilon_0(s,z,t))z\mathrm{d}z\,, \tag{3.3}$$

where h is the thickness of the beam and $z = 0$ is taken to be the center of the beam. The strain is related to curvature as in classical elastica theory[1], and the spontaneous strain depends on the built-in curvature κ_r of the beam (the curvature with no applied load and no illumination) and the concentration n_c of the *cis* molecules:

$$\varepsilon(s,z,t) = \kappa(s,t)z, \tag{3.4}$$

$$\varepsilon_0(s,z,t) = \kappa_r(s)z - \lambda n_c(s,z,t)\,, \tag{3.5}$$

where λ is a constant of proportionality linking the longitudinal strain and concentration of *cis* molecules. $\lambda > 0$ is when the *cis* molecules corresponds to an expansion, while $\lambda < 0$ corresponds to an induced contraction. This depends on the orientation of the director of the LCE. If the strip is made with directors parallel to the the length of the strip (as in the 'planar' face of Gelebart et al.), illumination produces a contraction along the length and therefore $\lambda < 0$. If, on the other hand, the strip is made with the director along the normal to the strip (as in the 'homoetropic' face of Gelebart et al.), illumination causes an elongation along the length of the strip and therefore $\lambda > 0$.

Substituting (3.4) and (3.5) into (3.3), we find the constitutive law in the form

$$m(s,t) = \frac{Eh^3}{12}(\kappa(s,t) - \kappa_0(s,t))\,, \tag{3.6}$$

where

$$\kappa_0(s,t) = \kappa_r(s) - \frac{12\lambda}{h^3}\int_{-h/2}^{h/2} n_c(s,z,t)z\mathrm{d}z\,. \tag{3.7}$$

It remains to specify the evolution of the spontaneous curvature in the presence of illumination. The concentration of *cis* molecules is increased by photon absorption, and decreased by thermal decay [27]:

$$\frac{\partial n_c}{\partial t}(s,z,t) = -\kappa_1 n_c(s,z,t) + (1 - n_c(s,z,t))\kappa_2\tilde{\alpha}_1\mathcal{I}(s,z,t),$$

[1] We assume that the neutral axis is unaffected by illumination since the penetration depth is small, as argued later.

where n_c is the fraction of activated chromophores, $\tilde{\alpha}_1$ is a material constant which measures the efficiency of the production of *cis* isomers by incident light, and $\mathcal{I}(s,z,t)$ denotes the illumination, *i.e.*, the quantity of photons per unit time arriving at the depth z at time t. κ_1 and κ_2 are the thermal decay and the forward isomerization reaction rates, respectively. In typical materials, $n_c \ll 1$ is small [21] so we can simplify the differential equation to

$$\tau \frac{\partial n_c}{\partial t}(s,z,t) = n_c(s,z,t) + \alpha_1 \mathcal{I}(s,z,t)\,, \tag{3.8}$$

where $\tau = 1/\kappa_1$ and $\alpha_1 = \kappa_2\tilde{\alpha}_1/\kappa_1$. Further, at any location s along the length of the strip, the intensity diminishes with depth with the number of photons absorbed [27]

$$\frac{\partial \mathcal{I}}{\partial z} = -\frac{1-n_c}{d}\mathcal{I}(s,z,t)\,,$$

where d is the penetration depth. So, when $n_c \ll 1$, the intensity follows Beer's law

$$\mathcal{I}(s,z,t) = \mathcal{I}_0(s,t)\exp\left(-\frac{h/2-z}{d}\right), \tag{3.9}$$

where $z = h/2$ is the free surface that is illuminated and $\mathcal{I}_0$ is the intensity of light on the illuminated surface[2]. Combining (3.7), (3.8), and (3.9),

$$\tau\frac{\partial \kappa_0}{\partial t}(s,t) = -\frac{12\lambda}{h^3}\int_{-h/2}^{h/2}\tau\frac{\partial n_c}{\partial t}(s,z,t)z\mathrm{d}z = -(\kappa_0(s,t)-\kappa_r(s)) + \alpha\mathcal{I}_0(s,t)\,,$$

where $\alpha = -\frac{12\lambda\alpha_1}{h^3}\int_{-h/2}^{h/2}\exp\left(-\frac{h/2-z}{d}\right)z\mathrm{d}z$ is an effective (macroscopic) coupling constant. Finally, the absorption of light on the surface depends on light intensity I_0 and on the relative orientation of the light and the strip, $\mathcal{I}_0(s,t) = I_0 f(\theta(s,t)-\theta_I)$, where θ_I is the angle of illumination. Therefore,

$$\tau\frac{\partial \kappa_0}{\partial t}(s,t) + (\kappa_0(s,t)-\kappa_r(s)) = \alpha I_0 f(\theta(s,t)-\theta_I)\,. \tag{3.10}$$

The projection function f is chosen as

$$f(\phi) = \begin{cases} \cos\phi & \text{if } \phi \in (-\pi/2, \pi/2), \\ 0 & \text{else.} \end{cases} \tag{3.11}$$

This f accounts for self-shadowing in an approximate but effective way: in our examples, the parts of the rods that are exposed to the light source are such that

[2]Note that the result (3.10) does not require the exponential profile of Beer's law, but simply a steady profile, $\mathcal{I}(s,z,t) = \mathcal{I}_0(s,t)\,f(z)$. Also note that the failure of the condition $n_c \ll 1$ leads to bleaching and other effects discussed in [27] and [28].

$\phi \in (-\pi/2, \pi/2)$ and in that case the coefficient $\cos\phi$ accounts for the reduction in light flux per unit area due to the non-normal incidence. Regions such that $\phi \notin (-\pi/2, \pi/2)$ are considered to be shadowed by other parts of the rod.

Finally, we combine (3.1), (3.2), (3.4), and (3.6), and non-dimensionalize the resulting equation along with (3.10), introducing the scaled arclength $S = s/l$ (where l is the length of the beam), the scaled time $T = t/\tau$ and the scaled curvature $K = l\kappa$,

$$\frac{\partial}{\partial S}\left(\frac{\partial\theta}{\partial S}(S,T) - K_0(S,T)\right) - F_x\cos\theta(S,T) + F_y\sin\theta(S,T) = 0, \tag{3.12}$$

$$\frac{\partial K_0}{\partial T}(S,T) + (K_0(S,T) - K_r(S)) = \Lambda f(\theta(S,T) - \theta_I)\,. \tag{3.13}$$

The constants F_x and F_y are Lagrange multipliers that enforce the inextensibility. Remarkably, these equations depend on two parameters only: the angle of illumination θ_I and the dimensionless constant

$$\Lambda = \alpha l I_0 = -\frac{12\kappa_2\tilde{\alpha}_1\bar{I}_0}{\kappa_1 h^3}\int_{-h/2}^{h/2}\exp\left(-\frac{h/2 - z}{d}\right)z\mathrm{d}z\,, \tag{3.14}$$

that encompasses various material and physical parameters—time constants of photo-activation and relaxation, penetration depth, the elastic modulus and thickness of the strip, and illumination intensity. The fact that so many material and physical parameters collapse into a single non-dimensional parameter highlights the flexibility that is available in the choice of material and structure in the development of light-activated structures. Since the dimensionless equations are governed by a single dimensionless parameter Λ, we are able to characterize all the possible behaviors in a given geometry simply by sweeping over Λ. Based on the values in Table 3.1 estimated from literature reports on a glassy azobenzene-functionalized polyimide, we obtain a value of $|\Lambda| \approx 2.9$; these values are typical of the materials used in many other experimental works, although not all of them document the material properties in detail.

To predict how the shape of the beam evolves with time, we solve these equations (3.12) and (3.13) for $\theta(S,T)$ using a numerical method described in the Supplementary Materials A with specific initial, boundary and illumination conditions. We remark that in deriving the equations, we assumed that the material response—the relation between curvature and moment (3.6), and the relation between illumination and spontaneous curvature (3.7)—is linear. Yet, the final equations are nonlinear as evidenced by the presence of the trigonometric terms in (3.12) and f in (3.13) due

Parameter	Typical Value
$\lambda\alpha_1$	$-5.4 * 10^{-5}$ m^{2}W^{-1} [29]
I_0	100 W/m^2 [29]
E	0.6 – 4 GPa [29]
h	15 μm [29]
d	0.56 μm [30]
w	1 mm [29]
l	15 mm [29]

Table 3.1: Estimates of the experimental parameters based on the literature.

to the nonlinearity of the kinematics of large deformation and the presence of finite rotations.

For future reference, we note that the equilibrium equation (3.12) can be derived by the Euler-Lagrange method as the stationarity condition of the energy functional

$$\mathcal{E}[\theta] = \int_0^1 \frac{1}{2}\left|\frac{\partial\theta}{\partial S} - K_0\right|^2 \mathrm{d}S\,. \tag{3.15}$$

3.3 Rolling ring

Our first example is motivated by the work of Yamada *et al.* [23] on a rolling ring and motor, as well as that of Wei *et al.* [25] on a rolling spiral. We consider a closed, initially circular ring on a rigid horizontal surface, which is illuminated with a steady source at angle θ_I. The fact that the ring is closed implies that

$$\int_0^1 \sin\theta(S,T)\mathrm{d}S = \int_0^1 \cos\theta(S,T)\mathrm{d}S = 0\,, \tag{3.16}$$

as well as $\theta(0,T) = \theta(1,T)$. We assume that the ring makes a tangential rolling contact with the horizontal surface so that $X(S_c(T),T) = S_c(T)$, $Y(S_c(T),T) = 0$ and

$$\theta(S_c(T),T) = 0\,, \tag{3.17}$$

where $S_c(T)$ is the point of contact. We determine this point of contact by assuming overall mechanical equilibrium of the ring under gravity so that the center of mass of the ring is always vertically above the point of contact,

$$\begin{aligned} S_c(T) = X(S_c(T),T) &= \int_0^1 X(S,T)\mathrm{d}S = \int_0^1 \left(\int_0^S \cos\theta(\tilde{S},T)\mathrm{d}\tilde{S}\right)\mathrm{d}S \\ &= \int_0^1 (1-S)\cos\theta(S,T)\mathrm{d}S = -\int_0^1 S\cos\theta(S,T)\mathrm{d}S\,. \end{aligned} \tag{3.18}$$

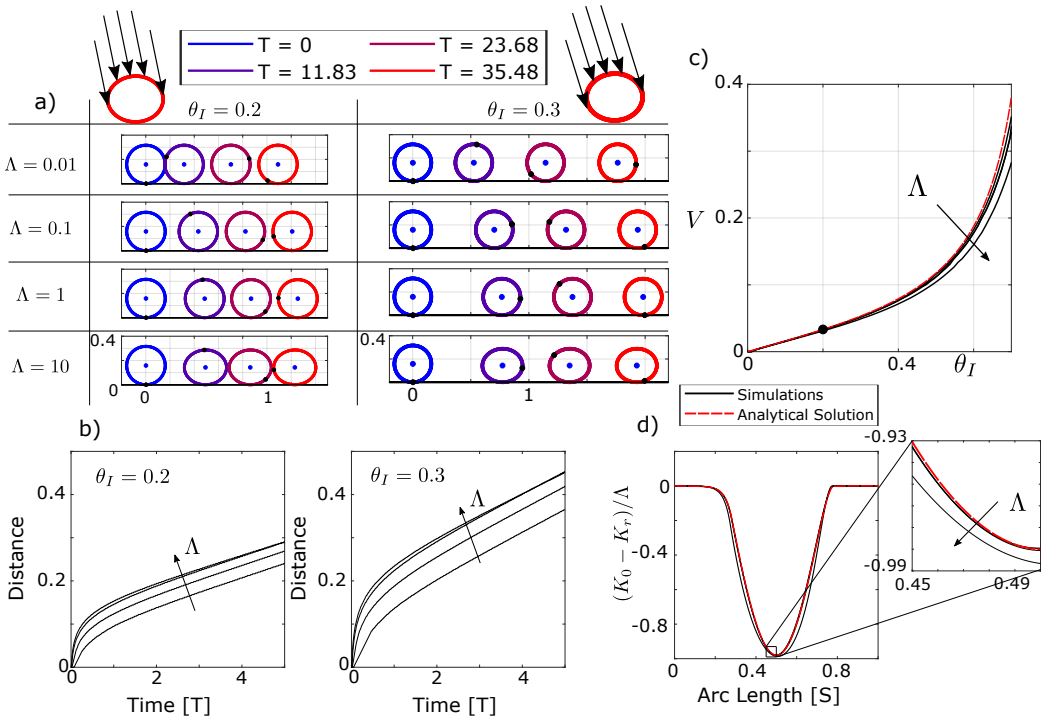

Figure 3.2: Rolling ring. (a) Snapshots of an initially circular ring with radius $R = 1/(2\pi)$ subjected to illumination at angle θ_I and of intensity Λ at times $T = \{0, 11.83, 23.68, 35.48\}$. The point that is initially in contact with the ground is marked with a black dot while the center of mass is the blue dot. The incident arrows indicate the direction of incoming light. Self-shadowing is taken into account thanks to the choice of f in equation (3.11); this is depicted by the absence of arrows in the lower part of the ring. (b) Distance traveled by the rolling ring vs. time for various intensities $\Lambda = \{0.01, 0.1, 1, 10\}$. Note that the a steady velocity is reached in all cases, after an initial transient. (c) Steady state velocity as a function of illumination angle and intensity. The velocity increases when the illumination angle moves away from the vertical, but is relatively insensitive to the intensity of illumination. (d) Scaled change of spontaneous curvature induced by illumination along the beam for $\theta_I = 0.2$ (indicated by dot in (c)), for various illumination intensities. This quantity appears to be largely insensitive to the intensity of illumination where Λ are as in (b). Simulation data is shown as solid black lines while the analytical solution given by solving Equation (3.29) is shown as a red dashed line.

We set $K_r = 2\pi$ and $\theta(S,0) = 2\pi S$ corresponding to an initially circular ring and solve the equations (3.12), (3.13) subject to the conditions above. Figure 3.2(a) shows snapshots of the ring for various angles and intensity of illumination. In each case, the ring deforms as it is illuminated, in a way which is non-symmetric with respect to the vertical axis and depends on the angle of illumination. This asymmetry causes the center of mass of the ring to move, which in turn causes the ring to roll. Figure 3.2(b) shows the distance travelled by the point of contact as a function of time under various angles and intensity of illumination. After an initial transient, the ring rolls with a steady velocity and has an invariant shape. The steady velocity is plotted as a function of the illumination angle for various illumination intensities in Figure 3.2(c): it is zero when the illumination is vertical ($\theta_I = 0$), which is a consequence of the symmetry, and increases with increasing angle of illumination θ_I. Remarkably, *the rolling velocity is practically independent of the intensity of illumination* in the range of values of Λ relevant to the experiments and investigated here. To investigate this further, we plot the scaled deviation in spontaneous curvature $(K_0 - K_r)/\Lambda$ as a function of arclength in Figure 3.2(d): this quantity appears to be practically independent of the intensity of illumination as well. This shows that amount of deformation scales linearly with the light intensity, while the profile of deformation (and, hence, the asymmetry and the rolling velocity) is largely independent of the intensity.

To understand these features, we analyze steadily rolling solutions, *i.e.*, we seek solutions of the form $\theta(S,T) = \Theta(S - VT)$ and aim at identifying the rolling velocity V. We set $\omega = 2\pi(S - VT)$ choosing $T = 0$ to be a time when the point in contact with the ground is $S = S_c(0) = 0$. This implies

$$\Theta(0) = 0. \tag{3.19}$$

The rolling condition (3.18) becomes

$$0 = \int_0^{2\pi} \omega \cos\Theta(\omega) \mathrm{d}\omega\,, \tag{3.20}$$

and the evolution equation (3.13)

$$-2\pi V \frac{\mathrm{d}K_0}{\mathrm{d}\omega} + (K_0 - 2\pi) = \Lambda f(\Theta - \theta_I)\,. \tag{3.21}$$

We now assume that *the shape of the ring is almost circular* so that

$$\Theta(\omega) = \omega + \Theta_1(\omega), \quad K_0(\omega) = 2\pi + K_1(\omega)\,, \tag{3.22}$$

where $|\Theta_1| \ll 1$ and $|K_1| \ll 1$ are treated as perturbations. Keeping only terms linear in Θ_1, K_1, the equilibrium equation (3.12) and closure condition (3.16) become

$$\begin{aligned} &4\pi^2\Theta_1''(\omega) - 2\pi K_1'(\omega) + F_y\cos\omega - F_x\sin\omega = 0\,, \\ &\int_0^{2\pi}\cos(\omega)\Theta_1(\omega)\mathrm{d}\omega = \int_0^{2\pi}\sin(\omega)\Theta_1(\omega)\mathrm{d}\omega = 0\ . \end{aligned} \tag{3.23}$$

Introducing the Fourier transform $\hat{f}(k) = \int_0^{2\pi} f(\omega)\exp(-ik\omega)\mathrm{d}\omega$ where k is an integer, we can solve (3.21) as

$$\hat{K}_1(k) = \frac{\Lambda\hat{f}_I(k)}{1 - 2i\pi kV}\ , \tag{3.24}$$

where

$$f_I(\omega) = f(\omega - \theta_I)\,. \tag{3.25}$$

Similarly, we can solve equation (3.23) in Fourier form as

$$\begin{aligned} \hat{\Theta}_1(\pm 1) &= 0 && \text{for } |k| = 1, \\ \hat{\Theta}_1(k) &= -i\tfrac{\hat{K}_1(k)}{2\pi k} && \text{for } |k| \geqslant 2\,. \end{aligned} \tag{3.26}$$

Note that the first equation in (3.23) yields F_x and F_y in terms of $\hat{\Theta}_1(\pm 1)$ and $\hat{K}_1(\pm 1)$ as well, but these expressions are not needed.

The horizontal tangency condition (3.19) reads $0 = \Theta(0) = \Theta_1(0) = \frac{1}{2\pi}\sum_k \hat{\Theta}_1(k)$ where the sum runs over all *signed* integers k. Rearranging the terms in the sum and solving for $\hat{\Theta}_1(0)$, we find

$$\hat{\Theta}_1(0) = -2\sum_{k\geqslant 1}\mathrm{Re}\,\hat{\Theta}_1(k)\,, \tag{3.27}$$

where we have used $\hat{\Theta}_1(-k) + \hat{\Theta}_1(k) = \overline{\hat{\Theta}_1(k)} + \hat{\Theta}_1(k) = 2\,\mathrm{Re}\,\hat{\Theta}_1(k)$ since $\Theta_1(\omega)$ is a real function. Here, $\overline{z}$ denoting the conjugate of the complex number z.

Equations (3.24–3.27) yield the shape in terms of the known illumination parameter Λ and of the unknown scaled rolling velocity V. The latter can be found by linearizing the rolling condition (3.20) as $\int_0^{2\pi} g(\omega)\Theta_1(\omega)d\omega = 0$ where $g(\omega) = \omega\sin\omega$. Using Parseval's identity, this can be rewritten as

$$\frac{1}{2\pi}\sum_k \hat{g}(k)\hat{\Theta}_1(-k) = 0, \qquad \text{where } \hat{g}(k) = \begin{cases} -\frac{\pi}{2}(2\pi ik + 1) & \text{if } |k| = 1\,, \\ \frac{2\pi}{k^2-1} & \text{if } |k| \neq 1\,. \end{cases} \tag{3.28}$$

Inserting (3.26–3.27) into this equation, we obtain $2\sum_{k\geqslant 2}\frac{k^2}{k^2-1}\,\mathrm{Re}\,\hat{\Theta}_1(k) = 0$ which, in view of (3.24–3.26), yields an implicit equation for the rolling velocity V in terms

of the angle of illumination θ_I,

$$\Lambda \cdot H(\theta_I, V) = 0 \quad \text{where} \quad H(\theta_I, V) = \sum_{k \geqslant 2} \frac{k}{k^2 - 1} \operatorname{Im}\left(\frac{\hat{f}_I(k)}{1 - 2i\pi k V} \right). \tag{3.29}$$

Note that f_I and hence H depends on θ_I, see equation (3.25).

When $\theta_I = 0$, $f_I(\omega) = f(\omega)$ is an even function of ω, so that $\hat{f}_0(k)$ is real, hence $H(0,0) = 0$. It is also clear from the form of $H(\theta_I, V)$ that $\dfrac{\partial H}{\partial \theta_I}$ and $\dfrac{\partial H}{\partial V}$ are generally non-zero. By the implicit function theorem, we can solve (3.29) for $V = V(\theta_I)$, at least for θ_I small enough. We do so numerically; the result is shown in Figure 3.2(c) as the dashed line, and agrees well with the non-linear simulations. In Figure 3.2(d), the distribution of natural curvatures predicted by the linear theory is compared to the non-linear numerical simulations, and a good agreement is obtained as well; the agreement with the linear theory is better and better for lower and lower illuminations, as could be anticipated.

Remarkably, the intensity of illumination Λ factors out in equation (3.29) selecting the rolling velocity, so that V depends on θ_I but not on Λ in this linear theory: this explains why the rolling velocity is largely independent of Λ in the non-linear simulations.

3.4 Waves in doubly clamped beams

The second example we study is motivated by the experiments of Gelebart *et al.* [22]. These experiments were done on a nematic strip possessing a splay director field: the nematic directors are aligned along the length of strip on one surface (called the *planar face*) and normal to the surface on the opposite face (*homeotropic face*). The goal is to induce contraction on one face and expansion on the other in order to maximize the magnitude of the photo-bending coupling $|\lambda|$. Exposing the planar face to light makes $\lambda < 0$ while exposing the homeotropic face to light makes $\lambda > 0$. In view of the analysis done in Section 3.2, $\Lambda \propto \alpha \propto -\lambda$, so illuminating the planar (respectively, homeotropic) face corresponds to $\Lambda > 0$ (resp. $\Lambda < 0$) in our model. Illumination, either due to the direct effect or due to temperature rise or both, reduces the nematic order causing a contraction by $(r/r_0)^{2/3}$ when illuminated on the planar face and an extension by $(r_0/r)^{1/3}$ when illuminated on the homeotropic face where r (respectively r_0) is the anisotropy parameter in the illuminated (respectively ambient) state. Since $r < r_0$, for fixed unscaled illumination intensity I_0, we expect the resulting photo-strain and spontaneous curvature coefficients $0 \leq \Lambda_p \approx -2\Lambda_h$, where Λ_p is the coefficient when illuminated on the planar side and Λ_h when

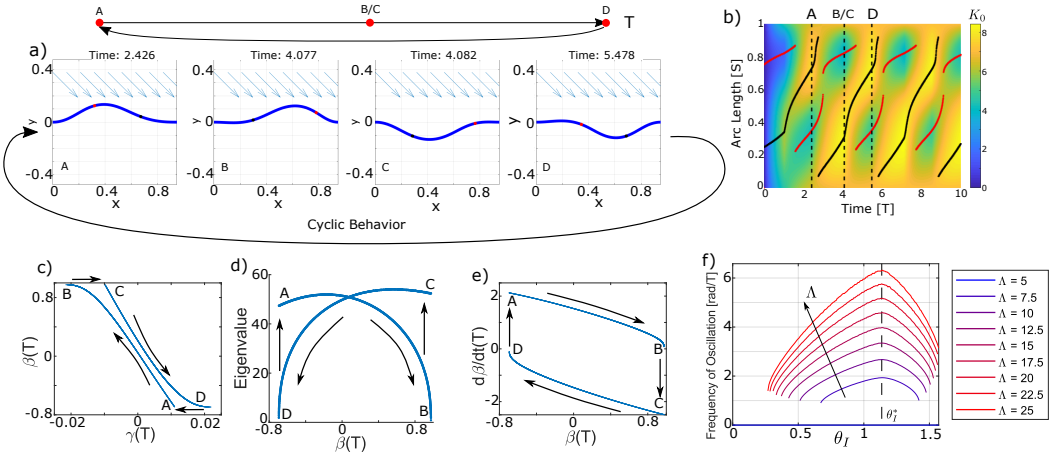

Figure 3.3: Waves in a strip for $\Lambda > 0$. (a) Snapshots of an initially flat strip clamped in a buckled state ($l_f = 0.95$) and subjected to illumination with $\Lambda = 10, \theta_I = \pi/4$. The arrows indicate the direction of incoming light. After an initial transient, it goes into a periodic motion. (b) Evolution of the light-induced spontaneous curvature K_0 of the strip. The peaks are marked with a black curve and the troughs are marked with a red curve. Note that the evolution becomes periodic but is quite complex with an alternation of slow (quasi-static) and fast (dynamic) motions. (c) Shape vs. spontaneous curvature descriptors as defined in Equation (3.31). (d) Incremental stiffness (lowest eigenvalue of the stiffness matrix) vs. spontaneous curvature descriptor. (e) Phase plot revealing the oscillation cycles after an initial transient. (f) Frequency of flapping as a function of illumination angle for various illumination angles. The angle for maximum flapping frequency (θ_I^*) is shown with the vertical dashed line.

illuminated on the homeotropic side. This distinction between Λ_p and Λ_h is caused by the small penetration depth only activating the *trans* to *cis* isomerization on the illuminated side; therefore, it is only the nematic orientation on the illuminated surface that matters. We study the results of our model first, and compare to the experimental observations next.

We first consider the case $\Lambda > 0$. We take a strip that is flat in the absence of any light or stress, so that $K_r = 0$. We use the same scaled quantities as earlier, and the scaled length of the strip is 1. We clamp the two ends at a distance $l_f < 1$ from each other, corresponding to boundary conditions

$$\theta(0,T) = \theta(1,T) = 0, \quad \int_0^1 \sin\theta(S,T)\mathrm{d}S = 0\,, \quad \int_0^1 \cos\theta(S,T)\mathrm{d}S = l_f\,. \tag{3.30}$$

Since $l_f < 1$, the beam buckles and there are two equivalent fundamental buckled

modes, buckled up and down. We choose one of the two states, say the buckled up state for definiteness, although the results are independent of this choice. We illuminate the strip with a light source that is spatially uniform and at an angle ($\theta_I \neq 0$) as shown in Figure 3.3(a). We solve the equations (3.12–3.13) subject to the boundary conditions (3.30).

Figure 3.3(a-e) show a typical simulation result. After an initial transient, we find that the beam goes into a periodic motion alternating between the up and down buckled shapes, see Figure 3.3(a). At the start of the cycle, we have an up-bump at the left side of the strip (state A). Illumination moves it to the right initially rapidly but slowing down and becoming very slow as it reaches the right end (B). It then pops into a down bump located on the left (C). Subsequently, the down-bump moves to the right initially rapidly but slowing down and becoming very slow as it reaches the right end (D). It then pops again into up-bump located on the left of the sample, and the cycle repeats.

The evolution of the light-induced spontaneous curvature as a function of time and position is shown in Figure 3.3(b). After an initial transient, we see that the spontaneous curvature reaches a steady periodic cycle. This is emphasized in Figure 3.3(c), which plots one particular Fourier component $\gamma(T)$ of the deflection, against one particular Fourier component $\beta(T)$ of the natural curvature,

$$\gamma(T) = \int_0^1 \sin(2\pi S) Y(S,T) \mathrm{d}S\,, \quad \beta(T) = \int_0^1 \sin(2\pi S) K_0(S,T) \mathrm{d}S\,. \tag{3.31}$$

We call these quantities the descriptors of the deformation and curvature, respectively. In the figure, the deformation descriptor appears to vary abruptly during the sudden changes from state B to C, and from D to A, although the the curvature descriptor remains unchanged. This suggest that the jumps are snap-through bifurcations, from one equilibrium solution of the elastica to another one. For some fixed time T and spontaneous curvature distribution $K_0(S,T)$, the equilibrium equation (3.12) may have multiple solutions (equivalently, $\mathcal{E}$ has multiple stationary points). Stable solutions are those for which the second variation is positive definite (Supplementary Material B). With the aim to confirm the snap-through scenario, we study the lowest eigenvalue associated with the second variation $\delta^2\mathcal{E}$ of the energy. It is plotted from the numerical solution, as a function of β in Figure 3.3(d). We see that this eigenvalue is positive at the start of the cycle at A (the solution with the up-bump) but decreases as we go from A to B. The jump at B occurs when the eigenvalue is becoming negative and the solution loses stability. It arrives on another

solution C having a down-bump, which appears to be elastically stable, *i.e.*, has a positive lowest eigenvalue. Again, the lowest eigenvalue begins to decrease as we go from C to D and passes through zero at D.

This reveals the mechanism of the cyclic motion. At any time, there are two possible solutions, one with an up-bump and one with a down-bump. If the solution with the up-bump has the bump on right, the solution with the down-bump has the bump on the left and vice-versa. The evolution of light-induced spontaneous curvature always forces the bump to move to the right, *i.e.*, away from the light source. At some point it loses stability and has to snap to the other solution. The periodic cycles are represented in the phase space $(\beta, \dot{\beta})$ in Figure 3.3(e). Immediately after a snap-through, the evolution speed $|\dot{\beta}|$ is high. As the instability is approached, the magnitude of $|\dot{\beta}|$ decreases until nearly zero. This coincides with the snap through and once the system snaps to the new configuration, $|\dot{\beta}|$ jumps to a large value again, and the other half of the cycle proceeds similarly.

We repeat this calculation for various illumination angles and illumination intensities, and the results are summarized in Figure 3.3(f). At any given intensity, there is a window of illumination angles at which periodic flapping solutions are observed. Outside this window, a stationary solution is reached, which can be the up-bump or the down-bump depending on the initial conditions. Physically, if the illumination is oriented in a direction too shallow to the beam, then the bump moves to the far end and is stable. This explains the lower limit. Similarly, if the illumination is close to being normal to the beam, then the beam finds it difficult to break the symmetry required to induce the periodic motion. This explains the upper limit. The window of periodic behavior becomes wider when the light intensity is increased. Further, at any given orientation, the frequency of the limit cycle increases with intensity; this can be seen from equation (3.10), where an increase of the light intensity in the right-hand side is seen to induce a quicker rate of change $\partial\kappa_0/\partial t$ of the curvature.

In figure 3.3(f), the angle of incidence θ_I maximizing the flapping frequency is 65.1° for $l_f = 0.95$, and this angle appears to be virtually independent of the light intensity as long as flapping takes place: it is just a function of l_f in our model. To compare with the observations of [22], we ran additional simulations using the same value $l_f = 0.957$ as in the experiments, and found that the maximum frequency is obtained for an angle of incidence $\theta_I = 65.7^\circ$; this value is similar to the peak at 70° in the experiment.

We now turn to the case when $\Lambda < 0$. As can be seen in Figure 3.4(a), the system

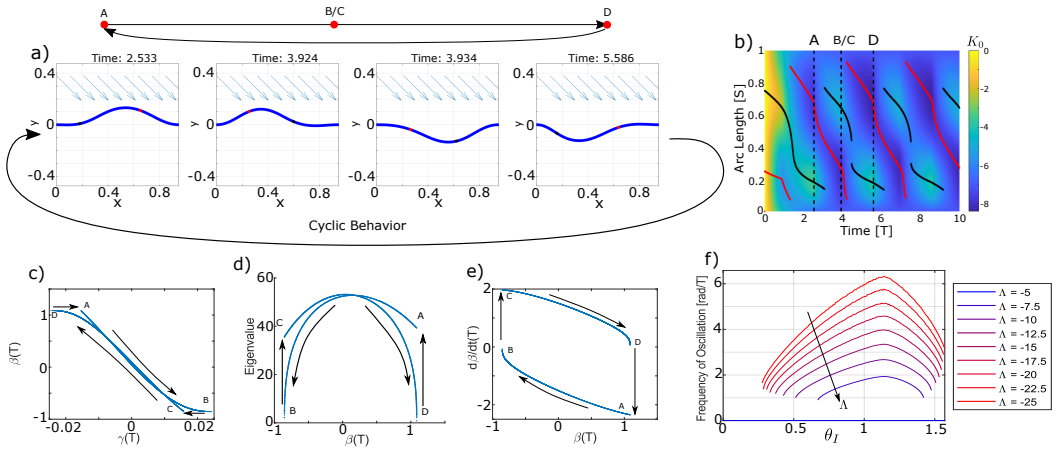

Figure 3.4: Waves in a strip for $\Lambda < 0$. Same as in Figure 3.3 except with $\Lambda = -10$.

again alternates between up and down buckled states. In this case, however, the bulge propagates from right to left, *i.e.*, towards the light source, and opposite from the case where $\Lambda > 0$. It can be seen in (c)–(e) that the descriptors give different paths through the phase space than when $\Lambda > 0$. This shows that flipping the sign of Λ does not simply amount to reverse the arrow of time. Interestingly, even though the deformation mode differs, the flapping frequency (f) does not change significantly between the positive and negative cases.

We now compare the experimental observations of Gelebart *et al.* [22]. After an initial transient, the strip begins a periodic motion with the wave moving from right to left as predicted in Figure 3.4, when illuminated on the homeotropic phase ($\Lambda = \Lambda_h < 0$). The wave moves from left to right as predicted in Figure 3.3 when illuminated on the planar face ($\Lambda = \Lambda_p > 0$). They also observed that the frequency of oscillation when illuminating the homeotropic face is lower as compared to the planar face, holding all other parameters fixed. Again, this is consistent with the predictions in Figures 3.4(f) and 3.3(f) since $|\Lambda_p| > |\Lambda_h|$ for fixed I_0. Further, this wave-like motion is observed only in a finite range of illumination angles and, for fixed illumination intensity, the range when illuminating the planar side is larger than that of the homeotropic side as predicted because $|\Lambda_p| > |\Lambda_h|$. All these results are in good agreement with the experimental observations.

3.5 Snap-through instability of doubly clamped beams

The critical event in the emergence of wave-like cyclic behavior is the snap-through instability. We study this instability more closely in our final example, by analyzing

the experiments first conducted by Shankar and collaborators [30, 31].

As in the previous example, an initially flat ($K_r = 0$) strip of (normalized) length 1 is clamped at both ends so that the end to end distance is $l_f < 1$; the beam is subject to the same boundary conditions (3.30). There are two equilibrium conditions, one buckled up, and one buckled down. As before, we start with the buckled up state and shine light on it. There are two differences compared to the geometry of the previous section: we limit attention to normal illumination ($\theta_I = 0$), and use a wide light beam described by a Gaussian distribution of intensity:

$$\Lambda(S,T) = \Lambda_{\max}\, g(X(S,T), \mu, W)\,, \tag{3.32}$$

where $g(X,\mu,W) = \exp\left(-\frac{(X-\mu)^2}{2W^2}\right)$ is a normal distribution centered at μ, with width W and scaled so that the peak value is 1.

We also conduct experiments using 1mm $\times$ 15mm $\times$ 50 μm beams made of planar nematic LCN films (see Materials and Methods and Supplementary Materials C for details) illuminated using a 365 nm LED.

Figure 3.5 summarizes our results. First consider the case when the illumination is centered on the bump ($\mu = l_f/2$) in Figure 3.5(a). When the light is turned on, the bumps flattens out slowly due to photo-induced curvature; after a period of slow deformation, it snaps suddenly at a critical time T^* to the down-buckled state. We have verified through eigenvalue analysis as before that the snap-through occurs when the up-bump solution becomes unstable. Continued illumination beyond the time of snap-through does not result in any significant further deformation. Figure 3.5(b) shows the results of the case where the illumination is slightly off the center of the bump ($\mu = 0.45$). The overall phenomenon is similar, but the initial slow deformation pushes the bump to the side away from the illumination instead of flattening it. These figures Figure 3.5(a,b) superpose the results of theoretical computation (cyan dashed line) with images retrieved from the experimental observation, showing excellent agreement.

As the illumination becomes too low, or the off-set from center $|l_f/2 - \mu|$ is too large, the beam does not snap-through. The phase portrait is shown in Figure 3.5(c) along with the experimental observations, again showing good agreement between theory and experiments. At higher illuminations, we see some evidence of photo-bleaching in the experiments and we believe that this accounts for the slight discrepancy. The phase portrait also shows that the smallest illumination required for snap-through

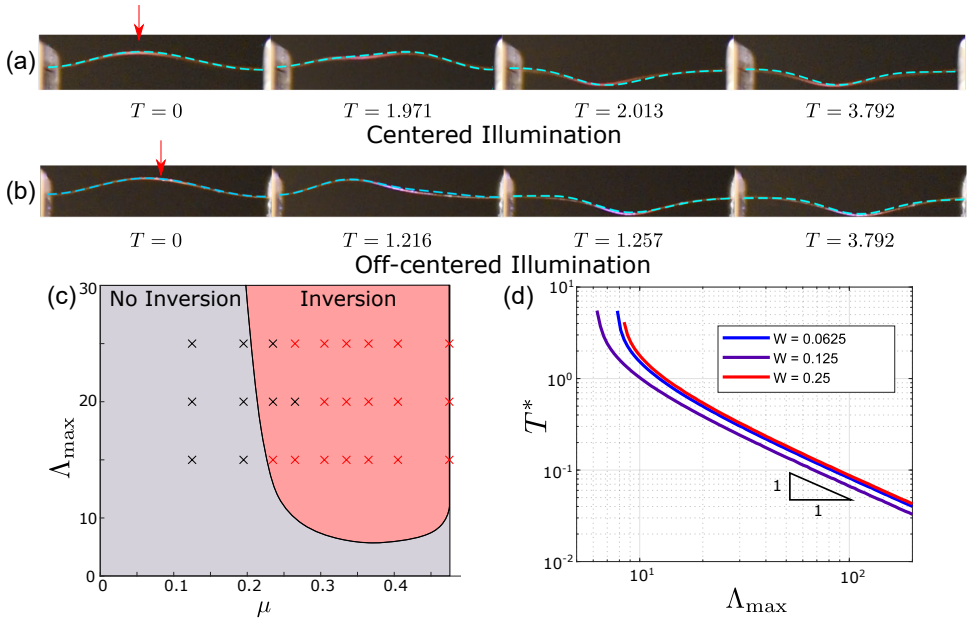

Figure 3.5: Snap-through of a strip subject to normal illumination. (a,b) Snapshots of an initially flat strip clamped in a buckled state and subjected to illumination with $\Lambda_{max} = 10$ and $l_f = 0.99$ for two different offsets, (a) $\mu = l_f/2$ and (b) $\mu = 0.45$. The red arrows indicate the location of the center of the laser beam. Predictions of the model (cyan) are superimposed onto the experimental observations without any adjustable parameter. Note the two distinct snap-through modes: symmetric with the creation of a flat-top when the light beam is centered and displacing the peak position when the light beam is not centered. (c) Phase portrait in the illumination vs. offset plane, showing the absence or presence of snap-through, for $l_f = 0.95$. The background colors and the crosses are the theoretical and experimental results, respectively. (d) Time for snap-through as a function of illumination for $l_f = 0.95$ and $\mu = l_f/2$, as predicted by the model.

decreases as the light is moved away from the center (i.e., when μ decreases from $l_f/2$). In other words, it is easier to snap when the illumination is slightly off center.

Finally, the time it takes for the snap-through to occur as a function of illumination in the centered case is plotted in Figure 3.5(d). We observe that for moderate to large illumination (i.e., away from the snap/no-snap boundary), this takes on a power law with an exponent -1. Shankar et al. [30] had studied this over a very large range of illuminations, and they reported a slope of -1, in agreement with our simulations.

3.6 Materials and Methods

Planar nematic liquid crystal network films were prepared following the procedure of Gelebart et al. [22] with modification. To synthesize films with a a penetration depth of 1.5 μm at an illumination wavelength of 365 nm, a formulation of 9.2 : 90.8 by weight of 4,4'-Bis(6-acryloyloxyhexyloxy)azobenzene (Azo-6) : 1,4-Bis[4-(6-acryloyloxyhexyloxy)benzoyloxy]-2-methylbenzene (RM82) was used, with 2.5 wt% of photoinitiator with respect to the total monomer weight. In a typical sample preparation, 4.6 mg Azo-6, 45.4 mg RM82, and 1.25 mg Iphenylbis(2,4,6-trimethylbenzoyl)phosphine oxide) (Irgacure 819) were melted together in a vial and vortexed repeatedly to ensure mixing. The molten monomer mixture was then infiltrated via capillary action into alignment cells on a hot plate at 100°C. The alignment cells were prepared by spin-coating Elvamide onto clean glass slides, rubbing the slides with a velvet cloth, and gluing the two Elvamide sides facing each other with epoxy mixed with 15 μm glass beads. The filled cells were subsequently cooled to 80°C, held isothermal for 5 minutes to induce alignment of the liquid crystalline mesogens, and photopolymerized for 30 minutes with 405 nm light. Following photopolymerization, samples were post-cured at 120°C for 10 minutes and the 15m thick LCNs were harvested by cracking open the alignment cells with a razor blade. Finally, beams of 1 mm in width were cut from the film with the nematic director along the long axis of the strip.

3.7 Conclusion

We explored various behaviors of nematic liquid crystal networks embeded with azobenzenes to incorporate a photo-mechanical effect. In this work, we specifically focus on 2D deformations of thin films which allowed us to use a standard beam model coupled with the interaction with light and curvature to model complex behaviors. We demonstrate cyclic motions to induce movement. The first involves a continuous rolling behavior where the interaction between the light and deformation leads to a wave solution that travels down the beam at a constant speed, despite the level of intensity of the light. The second case demonstrated how illumination can create conditions for a repeated snap-through instability. In this case, the motion is periodic and has sudden releases of energy to produce motion. This has the advantage of storing energy in strain, then suddenly releasing it in an instant. This scheme presents a significant advantage as many systems require high power rather than total energy; therefore, there are many ways to implement this strategy into engineering structures. The final configuration was similar to the previous;

however, we demonstrate a controlled snap-through by using a controlled light beam of different widths, locations, and intensities. This configuration is more similar to that of a switch and can be utilized to sense whether an illumination environment has been experienced.

The systems studied in this section are all 2D systems and only consider the deformations of a beam in the plane. While there are many systems that satisfy this condition, it does not paint the full picture. In many cases, the deformation of a thin structure can veer out of plane, involving multiple bending components as well as twist. Both of these introduce significant complication into modeling these structures. In order to address this difficulty, we develop a novel method of defining strains in the discrete elastic rod framework.

Chapter 4

NOVEL DEFORMATION MEASURES FOR RODS AND RIBBONS

The work presented in this chapter has been adapted from the following publication:

> Kevin Korner, Basile Audoly, and Kaushik Bhattacharya. "Simple deformation measures for discrete elastic rods and ribbons". In: *Proceedings of the Royal Society A* 27 (Dec. 2021), pp. 1–63. ISSN: 1364-5021. DOI: 10.1098/RSPA.2021.0561. URL: https://royalsocietypublishing.org/doi/abs/10.1098/rspa.2021.0561.

4.1 Introduction

In modeling non-linear deformations of rods, such as those in the presence of spontaneous curvatures and external forcing, we required some development of the discrete elastic rod model in order to accurately describe the strains. Particularly, the relationship between the discrete and continuous strain measures was not entirely clear. This distinction becomes important when trying to study a variety of highly nonlinear rod models.

The geometric non-linearity of thin elastic rods gives rise to a rich range of phenomena even when the strains are small, see e.g. [33, 34] for recent examples. So, the non-linear theory of rods has traditionally combined geometrically non-linearity with linear constitutive laws [35, 1]. However, recent interest has expanded beyond the linearly elastic regime, including viscous threads [36, 37], plastic and visco-plastic bars [38, 39, 40], visco-elastic rods [41], and capillary elastic beams made of very soft materials [42]. Thin elastic ribbons may also be viewed in this class with a non-linear constitutive law that captures the complex deformation of the cross-sections [3, 4, 43, 44, 5, 45].

The study of instabilities, especially in the presence of complex constitutive relations, requires an accurate but efficient numerical method. Here, we build on the work of Bergou et al. [46] to propose a numerical method applicable to slender elastic structures in general. To keep the presentation focused, we limit our presentation to *elastic* rods: both linearly elastic and non-linear elastic constitutive laws are covered. Our main contribution consists in providing a discrete geometric description of

slender rods. This kinematic building block is independent of the elastic constitutive law in our formulation, making the extension to inelastic constitutive laws relatively straightforward, as discussed in Section 4.4.

We follow the classical kinematic approach, and use the arc-length s in the undeformed configuration as a Lagrangian coordinate. We denote the center-line of the rod in the current configuration as $\boldsymbol{x}(s)$ (boldface symbols denote vectors). We introduce an orthonormal set of vectors $(\boldsymbol{d}_I(s))_{1\leqslant I\leqslant 3}$, called the *directors*, to describe the orientation of the cross-section. We impose the *adaptation condition* that the director $\boldsymbol{d}_3$ matches the unit tangent $\boldsymbol{t}$ to the center-line:

$$\boldsymbol{d}_3(s) = \boldsymbol{t}(s), \text{ where } \boldsymbol{t}(s) = \frac{\boldsymbol{x}'(s)}{|\boldsymbol{x}'(s)|}. \tag{4.1}$$

Here $\boldsymbol{x}'(s) = \partial\boldsymbol{x}/\partial s$ denotes the derivative of $\boldsymbol{x}$ with respect to the arc-length s. Note that the adaptation condition does *not* impose any restriction on the actual deformation of the rod at the microscopic scale; specifically, it does not require the deformed cross-section to be spanned by $\boldsymbol{d}_1$ and $\boldsymbol{d}_2$. Instead, it expresses the fact that the only role of the directors is to track the twisting motion of the cross-sections about the tangent. Equation (4.1) does not impose inextensibility either.

The rotation gradient $\boldsymbol{\kappa}(s)$, also known as the Darboux vector, is defined by

$$\boldsymbol{d}_I'(s) = \boldsymbol{\kappa}(s) \times \boldsymbol{d}_I(s), \qquad I = 1, 2, 3\,. \tag{4.2}$$

It exists and is unique since the directors are orthonormal. The deformation measures are

$$\kappa_{(I)}(s) = \boldsymbol{\kappa}(s) \cdot \boldsymbol{d}_I(s)\,. \tag{4.3}$$

A fourth deformation measure is introduced to characterize how the center-line stretches, such as $\varepsilon(s) = \frac{1}{2}\left(\boldsymbol{x}'^2(s) - 1\right)$ (Green-Lagrange strain).

This kinematic description is common to all variants of the rod model. It is complemented by constitutive equations specifying either the stored energy density (in the case of a hyperelastic theory) or the reaction forces and moments as functions of the four deformation measures or their histories. The formulation is completed by imposing either equilibrium or balance of momenta. The resulting equations for linear elastic constitutive relations are known as the Kirchhoff equations for rods, and they can be derived variationally, see [47, 1]; we will not discuss them further.

Various strategies have been proposed to simulate the equations for thin rods numerically. In approaches based on the finite-element methods, it is challenging to

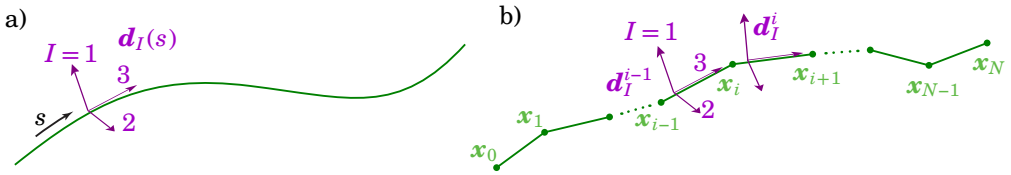

Figure 4.1: (a) A continuous elastic rod and (b) a discrete elastic rod. The adaptation condition from equations (4.1) and (4.9) is satisfied in both cases.

represent the kinematic constraint of adaptation (4.1) between the unknown center-line $\boldsymbol{x}(s)$ and the unknown rotation representing the orthonormal directors $\boldsymbol{d}_I(s)$. Another approach is based on super-helices or super-clothoids: in these high-order approaches, the bending and twisting strain measures $\kappa_{(I)}(s)$ are discretized into constant or piecewise linear functions. The result is a highly accurate method which has been successfully applied to several challenging problems [48, 49, 50]. The price to pay is that the reconstruction of the center-line in terms of the degrees of freedom is non-trivial and non-local. Additionally, some common boundary conditions, such as clamped-clamped conditions, must be treated using non-linear constraints.

A new approach called the Discrete elastic rods method was introduced by Bergou it et al. [46]; see [51] for a recent primer. The Discrete elastic rod method is a low-order method, which starts out by discretizing the center-line into a polygonal chain with nodes $(\boldsymbol{x}_0, \ldots, \boldsymbol{x}_N)$. The tangents and material frames $\boldsymbol{d}_I^i$ are defined on the segments, see Figure 4.1. The adaptation condition (4.1) is used to parameterize the material frames $(\boldsymbol{d}_I^i)_{1 \leqslant i \leqslant 3}$ in terms of the positions $(\boldsymbol{x}_{i-1}, \boldsymbol{x}_i)$ of the adjacent nodes and of a single twisting angle φ^i, as described in Section 4.2. A discrete rotation gradient is obtained by comparing the orthonormal directors from adjacent segments: this yields a differential rotation at a *vertex* between the segments. This must now be projected onto a material frame to yield the bending and twisting strain measures according to equation (4.3). The material frame, however, lives on *segments*. The original Discrete elastic rod formulation worked around this difficulty by introducing an additional director frame living on the nodes, obtained by averaging the director frames from the adjacent segments [46, 51]. In the present work, a different definition of the discrete bending and twisting strain measures is used, see Equations (4.14) and (4.16). This small change simplifies the formulation of model considerably. We note that a similar measure was introduced independently in a recent work on shearable rod models [52].

Overall, the proposed formulation offers the following advantages:

- As in the original Discrete rod model, the proposed formulation eliminates two out of the three degrees of freedom associated with the directors at each node using of the adaptation condition (4.1); this leads to a constraint-free formulation that uses degrees of freedom sparingly.
- The formulation of the model is concise: in particular the gradient and Hessian of the discrete elastic energy are given by the simple, closed form formulas listed in Section 4.3.
- The proposed deformation measures have a clear geometric interpretation: in the context of inextensible ribbons, for example, a discrete developability condition can easily be formulated in terms of the new set of discrete strains, see Section 4.4.
- The kinematic description can easily be combined with various constitutive models to produce discrete models for elastic rods, inextensible ribbons, viscous or visco-elastic rods, etc., as discussed in Section 4.4.

4.2 Discrete bending and twisting deformation measures

A compendium on quaternions

Rod models make use of rotations in the three-dimensional space. These rotations are conveniently represented using quaternions. Here, we provide a brief summary of quaternions and their main properties. A complete and elementary introduction to quaternions can be found in [53].

A quaternion $q \in \mathbb{Q}$ can be seen as a pair made up of a scalar $s \in \mathbb{R}$ and a vector $\boldsymbol{v} \in \mathbb{R}^3$, $q = (s, \boldsymbol{v})$. Identifying the scalar s and the vector $\boldsymbol{v}$ with the quaternions $(s, \mathbf{0})$ and $(0, \boldsymbol{v})$ respectively, one has the quaternion decomposition

$$q = s + \boldsymbol{v}.$$

The product of two quaternions $q_1 = (s_1, \boldsymbol{v}_1)$ and $q_2 = (s_2, \boldsymbol{v}_2)$ is defined as

$$q_1\, q_2 = (s_1\, s_2 - \boldsymbol{v}_1 \cdot \boldsymbol{v}_2) + (s_1 \boldsymbol{v}_2 + s_2 \boldsymbol{v}_1 + \boldsymbol{v}_1 \times \boldsymbol{v}_2)\,. \tag{4.4}$$

The product is non-commutative.

A unit quaternion $r = s + \boldsymbol{v}$ is a quaternion such that $s^2 + |\boldsymbol{v}|^2 = 1$. Unit quaternions represent rotations in the three-dimensional Euclidean space, in the following sense.

Define $\bar{r} = s - \boldsymbol{v}$ as the quaternion conjugate to r. Define the action of the unit quaternion r on an arbitrary vector $\boldsymbol{w}$ as

$$r * \boldsymbol{w} = r\,\boldsymbol{w}\,\bar{r},$$

where the left-hand side defines a linear map on the set of vectors $\boldsymbol{w}$, and the right-hand side is a double product of quaternions. It can be shown that (*i*) the quaternion $r * \boldsymbol{w}$ is a pure vector, (*ii*) the mapping $\boldsymbol{w} \longrightarrow r * \boldsymbol{w}$ is a rotation in Euclidean space, (*iii*) the quaternion r can be written as $r = \pm r_{\boldsymbol{n}}(\theta)$ where

$$r_{\boldsymbol{n}}(\theta) = \cos\frac{\theta}{2} + \boldsymbol{n}\,\sin\frac{\theta}{2} = \exp\frac{\boldsymbol{n}\,\theta}{2}, \tag{4.5}$$

θ is the angle of the rotation, and $\boldsymbol{n}$ is a unit vector subtending the axis of the rotation. Note that both unit quaternions $+r_{\boldsymbol{n}}(\theta)$ and $-r_{\boldsymbol{n}}(\theta)$ represent the same rotation.

Given two unit quaternions r_1 and r_2, consider the product $r_2\,r_1$: for any vector $\boldsymbol{w}$, the equality $(r_2\,r_1) * \boldsymbol{w} = r_2\,r_1\,\boldsymbol{w}\,\overline{r_2\,r_1} = r_2\,r_1\,\boldsymbol{w}\,\overline{r_1}\,\overline{r_2} = r_2 * (r_1 * \boldsymbol{w})$ shows that the unit quaternion $r_2\,r_1$ represents the *composition* of the rotations associated with r_1 applied first, and r_2 applied last. The multiplication of unit quaternions is therefore equivalent to the composition of rotations. In view of this, we will *identify* rotations with unit quaternions. The inverse of the rotation r will accordingly be identified with the conjugate $\overline{r}$.

Parallel transport

Parallel transport plays a key role in the Discrete elastic rods model, by allowing one to define twistless configurations of the material frame in an intrinsic way. For two unit vectors $\boldsymbol{a}$ and $\boldsymbol{b}$ such that $\boldsymbol{b} \neq -\boldsymbol{a}$, the parallel transport from $\boldsymbol{a}$ to $\boldsymbol{b}$ is the rotation mapping $\boldsymbol{a}$ to $\boldsymbol{b}$, whose axis is along the binormal $\boldsymbol{a} \times \boldsymbol{b}$. Parallel transport can be interpreted geometrically as the rotation mapping $\boldsymbol{a}$ to $\boldsymbol{b}$ and tracing out the shortest path on the unit sphere [46].

An explicit expression of the parallel transport from $\boldsymbol{a}$ to $\boldsymbol{b}$ in terms of unit quaternions is [54]

$$p_{\boldsymbol{a}}^{\boldsymbol{b}} = \sqrt{\frac{1 + \boldsymbol{a}\cdot\boldsymbol{b}}{2}} + \frac{1}{2}\,\frac{\boldsymbol{a}\times\boldsymbol{b}}{\sqrt{\frac{1+\boldsymbol{a}\cdot\boldsymbol{b}}{2}}}\,. \tag{4.6}$$

The proof is as follows. First it can be verified that $p_{\boldsymbol{a}}^{\boldsymbol{b}}$ is a unit quaternion, as can be shown by using the identity $\frac{|\boldsymbol{a}\times\boldsymbol{b}|^2}{1+\boldsymbol{a}\cdot\boldsymbol{b}} = \frac{1-(\boldsymbol{a}\cdot\boldsymbol{b})^2}{1+\boldsymbol{a}\cdot\boldsymbol{b}} = 1 - \boldsymbol{a}\cdot\boldsymbol{b}$. Second, the rotation $p_{\boldsymbol{a}}^{\boldsymbol{b}}$ indeed maps $\boldsymbol{a}$ to

$$p_{\boldsymbol{a}}^{\boldsymbol{b}} * \boldsymbol{a} = p_{\boldsymbol{a}}^{\boldsymbol{b}}\,\boldsymbol{a}\,\overline{p_{\boldsymbol{a}}^{\boldsymbol{b}}} = \boldsymbol{b}\,, \tag{4.7}$$

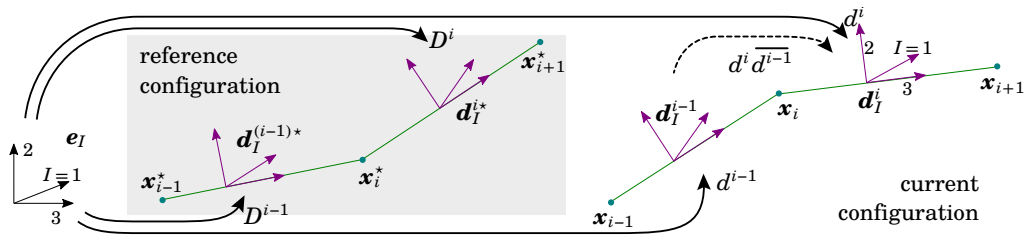

Figure 4.2: A node $\boldsymbol{x}_i$, its adjacent segments, and the adjacent nodes $\boldsymbol{x}_{i\pm1}$ in reference (gray background) and current (white background) configurations. Director frames, shown in purple, are represented by a unit quaternion, whose action on the Cartesian frame $\boldsymbol{e}_I$ yields the director frame.

as can be checked by explicit calculation. Finally, the axis of $p_{\boldsymbol{a}}^{\boldsymbol{b}}$ is indeed about the binormal $\boldsymbol{a} \times \boldsymbol{b}$: equation (4.5) shows that the vector part of the unit quaternion is aligned with the rotation axis and equation (4.6) shows that the vector part of $p_{\boldsymbol{a}}^{\boldsymbol{b}}$ is aligned with $\boldsymbol{a} \times \boldsymbol{b}$.

For two units vectors $\boldsymbol{a}$ and $\boldsymbol{b}$ such that $\boldsymbol{a} = -\boldsymbol{b}$, the parallel transport $p_{\boldsymbol{a}}^{\boldsymbol{b}}$ is ill-defined.

Reference and current configurations

A configuration of the discrete rod is defined by a set of nodes $\boldsymbol{x}_i$ indexed by an integer i, $0 \leqslant i \leqslant N$. We consider an open rod having unconstrained endpoints $\boldsymbol{x}_0$ and $\boldsymbol{x}_N$ for the moment; alternate boundary conditions such as periodic or clamped boundary conditions are discussed later. For simplicity, we limit attention to the case where the nodes are equally spaced in the undeformed configuration, *i.e.*, the undeformed length ℓ^j is independent of the segment index j: it is denoted as

$$\ell^j = \ell.$$

In addition to the undeformed configuration, the simulation deals with two configurations shown in Figure 4.2:

- **Reference configuration** (shown with a gray background in the figure). The only role of the reference configuration is to allow a parameterization of the current configuration. It does not bear any physical meaning and its choice does not affect the results of the simulations. It is chosen for convenience.

  In the reference configuration, the position of node i is denoted by $\boldsymbol{x}_i^\star$. The orthonormal frame of directors on segment i connecting nodes $\boldsymbol{x}_i^\star$ and $\boldsymbol{x}_{i+1}^\star$ is denoted as $(\boldsymbol{d}_I^{i\star})_{I\in\{1,2,3\}}$. The adaptation condition from equation (4.1)

requires that the third director $\boldsymbol{d}_3^{j\star}$ coincides with the unit tangent $\boldsymbol{T}^j$ to the segment in reference configuration,

$$\boldsymbol{d}_3^{j\star} = \boldsymbol{T}^j, \text{ where } \boldsymbol{T}^j = \frac{\boldsymbol{x}_{j+1}^\star - \boldsymbol{x}_j^\star}{|\boldsymbol{x}_{j+1}^\star - \boldsymbol{x}_j^\star|}. \tag{4.8}$$

- **Current configuration** (shown with a white background). The current configuration is the physical configuration of the rod and is the unknown in a simulation. It is parameterized by the degrees of freedoms (see Section 4.2).

  In the current configuration, the center-line of the rod is defined by the node positions $\boldsymbol{x}_i$. On segment i connecting the nodes $\boldsymbol{x}_i$ and $\boldsymbol{x}_{i+1}$, the directors are denoted as $(\boldsymbol{d}_I^i)_{I\in\{1,2,3\}}$. The adaptation condition from equation (4.1) requires

$$\boldsymbol{d}_3^j = \boldsymbol{t}^j, \text{ where } \boldsymbol{t}^j = \frac{\boldsymbol{x}_{j+1} - \boldsymbol{x}_j}{|\boldsymbol{x}_{j+1} - \boldsymbol{x}_j|}. \tag{4.9}$$

As shown in the figure, the orthonormal director frames $(\boldsymbol{d}_I^{j\star})_{1\leqslant I\leqslant 3}$ and $(\boldsymbol{d}_I^j)_{1\leqslant I\leqslant 3}$ are represented by unit quaternions D^j and d^j, respectively, that yield the directors when applied to the Cartesian basis $\boldsymbol{e}_I$:

$$D^j * \boldsymbol{e}_I = \boldsymbol{d}_I^{j\star} \qquad d^j * \boldsymbol{e}_I = \boldsymbol{d}_I^j \qquad \text{for } I = 1, 2, 3. \tag{4.10}$$

The quaternions $d^{j\star}$ and d^j therefore represent the rotations $\sum_{I=1}^3 \boldsymbol{d}_I^{j\star} \otimes \boldsymbol{e}_I$ and $\sum_{I=1}^3 \boldsymbol{d}_I^j \otimes \boldsymbol{e}_I$, respectively. They fully describe their respective frames.

The reference and current configurations are not assumed to be close to one another. However, our parameterization introduces a weak restriction: the reference configuration must be chosen such that the angle of the rotation $\left(d^j\,\overline{D}^j\right)$ mapping $\boldsymbol{d}_I^{j\star}$ to $\boldsymbol{d}_I^j$ does not come close to π, in any of the segments j. This condition is fulfilled by resetting periodically the reference configuration to the current configuration:

- in dynamic simulations, this reset is typically done at the end of any time step;
- in equilibrium problems, it is typically done whenever an equilibrium has been found and the load is incremented.

In principle, it is even possible to reset the reference configuration in the middle of the Newton-Raphson iteration used to update a time step (in the dynamic case) or the non-linear equilibrium (in the static case), but special care is required as this amounts to changing the parameterization of the unknown during iteration.

All the applications shown at the end of this paper deal with the static case, *i.e.*, they involve the calculation of equilibria for a series of load values: our simulations are initialized with the reference configuration $\boldsymbol{x}_i^\star$, $\boldsymbol{d}_I^{j\star}$ representing a simple starting point which is typically a straight or circular equilibrium configuration without any load (see the example description for further details). The reference configuration is reset each time an equilibrium is found.

Centerline-twist representation

In this section, we introduce a parameterization that provides a concise representation of the current configuration that is at the heart of the Discrete elastic rod method. All quantities from the reference configuration, such as the node positions $\boldsymbol{x}_i^\star$, unit tangents $\boldsymbol{T}^j$, material frames $\boldsymbol{d}_3^{j\star}$ and associated rotations D^j, are known. We proceed to analyze the current configuration. A key observation is that equation (4.9) yields the tangent director $\boldsymbol{d}_3^j$ as a function of the node positions $\boldsymbol{x}_i$: if the nodes are prescribed, the full frame of directors $\boldsymbol{d}_I^j$ can only twist about this tangent. The three directors $(\boldsymbol{d}_I^j)_{1\leqslant I\leqslant 3}$ on segment j, as well as the associated unit quaternion d^j by equation (4.10), can therefore be parameterized in terms of

- the adjacent nodes positions $\boldsymbol{x}_j$ and $\boldsymbol{x}_{j+1}$,
- a scalar twist angle φ^j.

The parameterization used by the Discrete elastic rod method may be written as [46, 55, 56]

$$d^j(\boldsymbol{x}_j, \varphi^j, \boldsymbol{x}_{j+1}) = p^j(\boldsymbol{x}_j, \boldsymbol{x}_{j+1})\, r_{\boldsymbol{T}^j}(\varphi^j)\, D^j\,, \tag{4.11}$$

where $\boldsymbol{x}_j$ and $\boldsymbol{x}_{j+1}$ are the positions of the adjacent nodes, φ^j is the twisting angle,

$$p^j(\boldsymbol{x}_j, \boldsymbol{x}_{j+1}) = p_{\boldsymbol{T}^i}^{\boldsymbol{t}^i(\boldsymbol{x}_j, \boldsymbol{x}_{j+1})} \tag{4.12}$$

is the parallel transport from the reference unit tangent $\boldsymbol{T}^i$ to the current unit tangent $\boldsymbol{t}^i(\boldsymbol{x}_j, \boldsymbol{x}_{j+1})$ given as a function of the node positions by equation (4.9), $r_{\boldsymbol{T}^j}(\varphi^j) = \cos\frac{\varphi^j}{2} + \boldsymbol{T}^j \sin\frac{\varphi^j}{2}$ is the rotation about $\boldsymbol{T}^j$ with angle φ^j (see equation (4.5)), and D^j is the unit quaternion associated with the reference configuration of the directors (see equation (4.10)).

Using equations (4.10), (4.8) and (4.7), we have $\boldsymbol{d}_3^j = d^j(\boldsymbol{x}_j, \varphi^j, \boldsymbol{x}_{j+1}) * \boldsymbol{e}_3 = p^j(\boldsymbol{x}_j, \boldsymbol{x}_{j+1}) * (r_{\boldsymbol{T}}(\varphi^j, \boldsymbol{T}^j) * (D^j * \boldsymbol{e}_3)) = p_{\boldsymbol{T}^i}^{\boldsymbol{t}^i} * (r_{\boldsymbol{T}^j}(\varphi^j) * \boldsymbol{T}^j) = p_{\boldsymbol{T}^i}^{\boldsymbol{t}^i} * \boldsymbol{T}^j = \boldsymbol{t}^j$: the parameterization (4.11) of the directors satisfies the adaptation constraint in (4.9) automatically.

This yields a parameterization of the rod in terms of the degrees of freedom vector

$$\boldsymbol{X} = (\boldsymbol{x}_0, \varphi^0, \boldsymbol{x}_1, \varphi^1, \boldsymbol{x}^2, \cdots, \boldsymbol{x}_{n-1}, \varphi^{n-1}, \boldsymbol{x}_n), \tag{4.13}$$

where the nodes positions $\boldsymbol{x}_i$ are read off directly from $\boldsymbol{X}$ and the directors are reconstructed using equations (4.10) and (4.11). It is called the *centerline-twist representation*.

As observed in Section 4.2, the parallel transport in equation (4.12) is singular if $\boldsymbol{t}^i(\boldsymbol{x}_j, \boldsymbol{x}_{j+1}) = -\boldsymbol{T}^i$, *i.e.*, if any one of the tangents flips by an angle π between the reference and current configuration. The periodic reset of the reference configuration described earlier in Section 4.2 prevents this from happening.

Note that in the original paper of [46], parallel transport was used to move the directors from one segment to an adjacent segment (*spatial* parallel transport). This makes the directors dependent on the degrees of freedom associated with all the nodes and segments located on one side of the directors. Here, like in subsequent work by the same authors [55, 56], we use parallel transport 'in time': in equation (4.11), $p^j(\boldsymbol{x}_j, \boldsymbol{x}_{j+1})$ serves to parameterize the directors in current configuration in terms of the same set of directors in reference configuration. With this approach, the directors are a function of the *local* degrees of freedom, as implied by the notation $d^j(\boldsymbol{x}_j, \varphi^j, \boldsymbol{x}_{j+1})$ in equation (4.11).

Lagrangian rotation gradient

The rotation mapping one director frame $(\boldsymbol{d}_I^{i-1})_{I=1,2,3}$ to the adjacent director frame $(\boldsymbol{d}_I^i)_{I=1,2,3}$ is shown by the dashed arrow on top of Figure 4.2. It captures the variation of the frame along the rod, and it is the discrete counterpart of the rotation gradient $\boldsymbol{\kappa}(s)$ introduced in equation (4.2). Using equation (4.10), it can be written as the composition of the rotations $\overline{d^{i-1}}$ and d^i:

$$d^i\,\overline{d^{i-1}} : \boldsymbol{d}_I^{i-1} \mapsto \boldsymbol{d}_I^i\,.$$

This rotation is an Eulerian quantity: like its continuous counterpart $\boldsymbol{\kappa}(S)$, it is not invariant when the rod rotates rigidly. The following, however, is a Lagrangian version q_i of the rotation gradient that is invariant by rigid-body rotations,

$$q_i(\boldsymbol{x}_{i-1}, \varphi^{i-1}, \boldsymbol{x}_i, \varphi^i, \boldsymbol{x}_{i+1}) := \overline{d^{i-1}}(\boldsymbol{x}_{i-1}, \varphi^{i-1}, \boldsymbol{x}_i)\, d^i(\boldsymbol{x}_i, \varphi^i, \boldsymbol{x}_{i+1})\,. \tag{4.14}$$

Here, we depart from earlier work on Discrete elastic rods [46] who used $q_i := q_i^{\text{avg}} = \bar{d}_i^{\dagger}\,(d^i\,\overline{d^{i-1}})\,d_i^{\dagger}$ instead, where $d_i^{\dagger}$ is some average of the adjacent frames

d^{i-1} and d^i. A definition of the rotation gradient similar to (4.14) has been used in the context of shearable rods [52] and in a purely geometric analysis of discrete rods [54].

We now explain why this definition represents a Lagrangian rotation gradient. One way to define a Lagrangian rotation gradient, is to pull back the Eulerian rotation gradient $d^i\,\overline{d^{i-1}}$ to the reference configuration. However, the discreteness of our representation raises a difficulty: the frames are defined on the segment while the Eulerian rotation gradient $d^i\,\overline{d^{i-1}}$ is defined on the nodes. So, we could use the frame associated with the segment on the left of the node for the pull back by defining $q_i^{\text{left}} = \overline{d^{i-1}}\,(d^i\,\overline{d^{i-1}})\,d^{i-1}$, but this biases the choice on the left. Or, we could use the right counter-part, $q_i^{\text{right}} = \overline{d^i}\,(d^i\,\overline{d^{i-1}})\,d^i$, but this biases the choice to the right. However, these biases are apparent only: elementary calculations shows that these are in fact identical:

$$q_i^{\text{left}} = \overline{d^{i-1}}\,d^i\,\left(\overline{d^{i-1}}\,d^{i-1}\right) = \overline{d^{i-1}}\,d^i = q_i, \quad q_i^{\text{right}} = \left(\overline{d^i}\,d^i\right)\,\overline{d^{i-1}}\,d^i = \overline{d^{i-1}}\,d^i = q_i, \tag{4.15}$$

thereby justifying our definition.

The unit quaternion q_i introduced in equation (4.14) is the discrete analogue of the pull-back $(\boldsymbol{e}_I \otimes \boldsymbol{d}_I(s)) \cdot \boldsymbol{\kappa}(s)$ of the rotation gradient $\boldsymbol{\kappa}(s)$ used in the continuous rod theory, whose components $\kappa_J(s) = \boldsymbol{e}_J \cdot [(\boldsymbol{e}_I \otimes \boldsymbol{d}_I(s)) \cdot \boldsymbol{\kappa}(s)] = \boldsymbol{d}_J(s) \cdot \boldsymbol{\kappa}(s)$ define the bending and twisting measures. In the following section, bending and twisting are similarly extracted from the unit quaternion q_i.

Bending and twisting deformation measures

The discrete bending and twisting deformation measures are defined as the components of the pure vector,

$$\boldsymbol{\kappa}_i(\boldsymbol{x}_{i-1}, \varphi^{i-1}, \boldsymbol{x}_i, \varphi^i, \boldsymbol{x}_{i+1}) = q_i - \overline{q}_i. \tag{4.16}$$

This $\boldsymbol{\kappa}_i$ is twice the vector part $\mathcal{I}(q_i) = \frac{q_i - \overline{q}_i}{2}$ of the quaternion q_i, which shows that it is indeed a vector. Let $\kappa_{i,I}$ denote its components in the Cartesian basis, such that $\boldsymbol{\kappa}_i = \sum_{I=1}^3 \kappa_{i,I}\,\boldsymbol{e}_I$. The first two components $\kappa_{i,1}$ and $\kappa_{i,2}$ can be interpreted as measures of bending about the transverse directors $\boldsymbol{d}_1^j$ and $\boldsymbol{d}_2^j$, while the third component $\kappa_{i,3}$ is a discrete measure of twisting. Like q_i, these are *integrated* versions of their smooth counterparts, that are proportional to the discretization length ℓ; this will be taken into account when setting up a discrete strain energy.

Summary

The current configuration is reconstructed in terms of the degrees of freedom $\boldsymbol{X}$ from equation (4.13) as follows:

- the node positions $\boldsymbol{x}_i$ are directly extracted from $\boldsymbol{X}$, see equation (4.13),
- the unit tangents $\boldsymbol{t}^j(\boldsymbol{x}_j, \boldsymbol{x}_{j+1})$ are obtained from equation (4.9),
- parallel transport $p^j(\boldsymbol{x}_j, \boldsymbol{x}_{j+1})$ is obtained by combining equations (4.12) and (4.6),
- the director frames $d^j(\boldsymbol{x}_j, \varphi^j, \boldsymbol{x}_{j+1})$ are obtained from equation (4.11),
- the rotation gradient $q_i(\boldsymbol{x}_{i-1}, \varphi^{i-1}, \boldsymbol{x}_i, \varphi^i, \boldsymbol{x}_{i+1})$ is available from equation (4.14),
- the bending and twisting deformation vector $\boldsymbol{\kappa}_i(\boldsymbol{x}_{i-1}, \varphi^{i-1}, \boldsymbol{x}_i, \varphi^i, \boldsymbol{x}_{i+1})$ is calculated from equation (4.16).

Finally, a possible definition of the discrete stretching measure on segment j joining nodes $\boldsymbol{x}_j$ and $\boldsymbol{x}_{j+1}$ is

$$\varepsilon^j(\boldsymbol{x}_j, \boldsymbol{x}_{j+1}) = \frac{1}{2}\left(\frac{(\boldsymbol{x}_{j+1} - \boldsymbol{x}_j)^2}{\ell} - \ell\right), \tag{4.17}$$

see for instance [42]. Here, ℓ denotes the undeformed length of the segments, which is different from the length $|\boldsymbol{x}^\star_{j+1} - \boldsymbol{x}^\star_j|$ in reference configuration. This discrete stretching measure is an integrated version of the continuous strain $\varepsilon(S)$, like the discrete bending and twisting deformation measures $\kappa_{i,I}$. The particular definition of the stretching measure ε^j in equation (4.17) requires the evaluation of the *squared* norm and not of the norm itself, which simplifies the calculation of the gradient significantly.

Interpretation of the discrete deformation measures

We now show that the discrete deformation measures (up to a minor rescaling) may be interpreted as the rotation that transports the director frame from one segment to the next.

Consider the function ψ

$$\psi(t) = \frac{\arcsin(t/2)}{t/2} \quad \text{for } 0 \leqslant t \leqslant 2, \tag{4.18}$$

and note that $\psi(t) \approx 1$ for $t \ll 1$ (See supplementary information for a plot of this function). Define the *adjusted deformation measure* to be

$$\omega_{i,J} = \psi(|\boldsymbol{\kappa}_i|)\, \boldsymbol{\kappa}_i \cdot \boldsymbol{e}_J. \tag{4.19}$$

This is well defined for all values of κ since $|\boldsymbol{\kappa}_i| = |q_i - \overline{q}_i| \leqslant 2\,|q_i| = 2$. This rescaling is insignificant in the continuum limit where $d^{i-1} \approx d^i$, $q_i \approx 1$ and $|\boldsymbol{\kappa}_i| \ll 1$, implying $\psi(|\boldsymbol{\kappa}_i|) \approx 1$. Even for moderate values of $|\boldsymbol{\kappa}_i|$, the original and adjusted deformations measures are not very different, $\omega_{i,J} \approx \boldsymbol{\kappa}_i \cdot \boldsymbol{e}_J$, as the variations of the function ψ are bounded by $1 \leqslant \psi(t) \leqslant \pi/2$.

The adjusted deformation measure has a simple geometric interpretation. We start from the decomposition (4.5) of the rotation gradient $q_i = r_{\boldsymbol{n}_i}(\theta_i) = \cos\frac{\theta_i}{2} + \boldsymbol{n}_i \sin\frac{\theta_i}{2} = \exp\frac{\boldsymbol{n}_i\,\theta_i}{2}$, where $\boldsymbol{n}_i$ is a unit vector aligned with the axis of the rotation q_i, and θ_i is the angle of this rotation, $0 \leqslant \theta \leqslant \pi$. In view of equation (4.16), $\boldsymbol{\kappa}_i = q_i - \overline{q}_i = 2 \sin\frac{\theta_i}{2}\, \boldsymbol{n}_i$. In particular, $|\boldsymbol{\kappa}_i| = 2 \sin\frac{\theta_i}{2}$ and so $\psi(|\boldsymbol{\kappa}_i|) = \frac{\theta_i/2}{\sin(\theta_i/2)}$ from equation (4.18). The adjusted strain is then $\omega_{i,J}\, \boldsymbol{e}_J = \psi(|\boldsymbol{\kappa}_i|)\, \boldsymbol{\kappa}_i = \frac{\theta_i/2}{\sin(\theta_i/2)}\, 2 \sin\frac{\theta_i}{2}\, \boldsymbol{n}_i = \theta_i\, \boldsymbol{n}_i$: in effect, the adjustment factor $\psi(|\boldsymbol{\kappa}_i|)$ transforms $\boldsymbol{\kappa}_i = 2\,\mathcal{I}\,(q_i)$ (twice the vector part of q_i) into $\omega_{i,J}\, \boldsymbol{e}_J = \theta_i\, \boldsymbol{n}_i = 2 \log q_i$ (twice its logarithm).

Now, rewriting $q_i = \overline{d^{i-1}}\, d^i = \overline{d^{i-1}} \left(d^i\, \overline{d^{i-1}}\right) d^{i-1} = q_i^{\text{right}}$, one sees that q_i is conjugate to $d^i\, \overline{d^{i-1}}$. Combining with $q_i = \cos\frac{\theta_i}{2} + \boldsymbol{n}_i \sin\frac{\theta_i}{2}$, we have $d^i\, \overline{d^{i-1}} = d^{i-1}\, q_i\, \overline{d^{i-1}} = \cos\frac{\theta_i}{2} + (d^{i-1} * \boldsymbol{n}_i) \sin\frac{\theta_i}{2} = \exp\frac{(d^{i-1} * \boldsymbol{n}_i)\,\theta_i}{2}$: as is well known, the conjugate rotation $d^i\, \overline{d^{i-1}}$ has the same angle θ_i as the original rotation q_i and its axis is obtained by applying the rotation d^{i-1} to the original axis. This can be rewritten as

$$d^i = \exp\left(\frac{\boldsymbol{\Omega}_i}{2}\right) d^{i-1} \tag{4.20}$$

where $\boldsymbol{\Omega}_i = d^{i-1} * \boldsymbol{n}_i\, \theta_i = d^{i-1} * \omega_{i,J}\, \boldsymbol{e}_J = \omega_{i,J}\, \boldsymbol{d}_J^{i-1}$ is a (finite) rotation vector. Similar relations have been derived in the work of [54]. Repeating the same argument with $q_i = \overline{d^{i-1}}\, d^i = \overline{d^i}\, (d^i\, \overline{d^{i-1}})\, d^i = q_i^{\text{left}}$, one can show that the vector $\boldsymbol{\Omega}$ has the same decomposition in the other directors frame, $\boldsymbol{\Omega}_i = \omega_{i,J}\, \boldsymbol{d}_J^i$:

$$\boldsymbol{\Omega}_i = \omega_{i,J}\, \boldsymbol{d}_J^{i-1} = \omega_{i,J}\, \boldsymbol{d}_J^i. \tag{4.21}$$

Equations (4.20–4.21) show that *the adjusted deformation measures $\omega_{i,J}$ are the components of the rotation vector $\boldsymbol{\Omega}_i$ that maps one set of directors frame $(\boldsymbol{d}_I^{i-1})_{I=1,2,3}$ to the other one $(\boldsymbol{d}_I^i)_{I=1,2,3}$* across the vertex $\boldsymbol{x}_i$. Remarkably, these components can be calculated in any one of the adjacent directors frame as they are identical.

One could build a Discrete elastic rod model based on the adjusted deformation measure $\omega_{i,J}\,\boldsymbol{e}_J = 2\,\overline{d^{i-1}} * \log\left(d^i\,\overline{d^{i-1}}\right) = 2\,\overline{d^i} * \log\left(d^i\,\overline{d^{i-1}}\right)$ instead of the deformation measure $\boldsymbol{\kappa}_i$ proposed in Section 4.2. The benefit is that $\omega_{i,J}$ have an even simpler interpretation, see equations (4.20–4.21). The drawback is that the function ψ gets involved in the calculation of the strain, resulting in cumbersome formulas for the strain gradients (Section 4.3). Therefore, we continue to use the original deformation measures.

4.3 Variations of the discrete deformation measures

In this section, we present explicit formulae for the first and second derivatives of the deformation measures $\boldsymbol{\kappa}_i$ (summarized in Section 4.2) with respect to $\boldsymbol{X}$. The first gradient is required for determination of the internal forces, which are the first gradient of the strain energy. The availability of the second gradient in analytical form makes it possible to use implicit time-stepping methods (in dynamic problems) or to evaluate the Hessian for second order methods (in static problems).

Our notation for variations is first introduced based on a simple example. For a function $\boldsymbol{y} = \boldsymbol{f}(\boldsymbol{x})$ taking a vector argument $\boldsymbol{x}$ and returning a vector $\boldsymbol{y}$, the first variation is the linear mapping $\delta\boldsymbol{x} \mapsto \delta\boldsymbol{y} = \boldsymbol{f}'(\boldsymbol{x}) \cdot \delta\boldsymbol{x}$, where $\delta\boldsymbol{x}$ is a perturbation to $\boldsymbol{x}$ and $\boldsymbol{f}'(\boldsymbol{x})$ is the gradient matrix. To compute the second variation, we start from $\delta\boldsymbol{y} = \boldsymbol{f}'(\boldsymbol{x}) \cdot \delta\boldsymbol{x}$, perturb the argument $\boldsymbol{x}$ of $\boldsymbol{f}'$ as $\boldsymbol{x} + \delta\boldsymbol{x}$ and linearize the result as $\boldsymbol{f}'(\boldsymbol{x} + \delta\boldsymbol{x}) \cdot \delta\boldsymbol{x} \approx \boldsymbol{f}'(\boldsymbol{x}) \cdot \delta\boldsymbol{x} + \boldsymbol{f}''(\boldsymbol{x}) : (\delta\boldsymbol{x} \otimes \delta\boldsymbol{x})$. Here, the second variation is defined as the second order term $\delta^2\boldsymbol{y} := \boldsymbol{f}''(\boldsymbol{x}) : (\delta\boldsymbol{x} \otimes \delta\boldsymbol{x})$, where $\boldsymbol{f}''(\boldsymbol{x})$ is the Hessian. By construction, $\delta^2\boldsymbol{y}$ is a quadratic form of $\delta\boldsymbol{x}$.

In this section, the reference configuration is fixed and the degrees of freedom are perturbed by $\delta\boldsymbol{X} = (\cdots, \delta\boldsymbol{x}_i, \delta\varphi^i, \cdots)$. We simply present the final results; the detailed calculations are cumbersome but straightforward, and provided as supplementary material.

- **unit tangents** $\boldsymbol{t}^i = (\boldsymbol{x}_{i+1} - \boldsymbol{x}_i)/|\boldsymbol{x}_{i+1} - \boldsymbol{x}_i|$ from equation (4.9),

$$\begin{aligned} \delta\boldsymbol{t}^i &= \tfrac{\boldsymbol{I} - \boldsymbol{t}^i \otimes \boldsymbol{t}^i}{|\boldsymbol{x}_{i+1} - \boldsymbol{x}_i|} \cdot (\delta\boldsymbol{x}_{i+1} - \delta\boldsymbol{x}_i) \\ \delta^2\boldsymbol{t}^i &= -\tfrac{\boldsymbol{\tau}^i + (\boldsymbol{\tau}^i)^{T(132)} + (\boldsymbol{\tau}^i)^{T(231)}}{|\boldsymbol{x}_{i+1} - \boldsymbol{x}_i|^2} : ((\delta\boldsymbol{x}_{i+1} - \delta\boldsymbol{x}_i) \otimes (\delta\boldsymbol{x}_{i+1} - \delta\boldsymbol{x}_i)), \end{aligned} \tag{4.22}$$

  where $\boldsymbol{I}$ is the identity matrix, $\boldsymbol{\tau}^i$ is the third-order tensor $\boldsymbol{\tau}^i = (\boldsymbol{I} - \boldsymbol{t}^i \otimes \boldsymbol{t}^i) \otimes \boldsymbol{t}^i$, the colon denotes the double contraction of the *last* two indices of the rank-three tensor on the left-hand side. For any permutation (n_1, n_2, n_3) of $(1, 2, 3)$,

$T(n_1, n_2, n_3)$ denotes the generalized transpose of a rank-three tensor $\boldsymbol{\mu}$ such that $\mu^{T(n_1 n_2 n_3)}_{i_1 i_2 i_3} = \mu_{i_{n_1} i_{n_2} i_{n_3}}$;

- **parallel transport** $p^i = p^{\boldsymbol{t}^i}_{\boldsymbol{T}^i}$ from equations (4.12) and (4.6),

$$\begin{array}{rcl} \delta\hat{\boldsymbol{p}}^i & = & \left((\boldsymbol{t}^i)_\times - \frac{\boldsymbol{t}^i \otimes \boldsymbol{k}^i}{2}\right) \cdot \delta\boldsymbol{t}^i, \\ \delta^2\hat{\boldsymbol{p}}^i & = & \left((\boldsymbol{t}^i)_\times - \frac{\boldsymbol{t}^i \otimes \boldsymbol{k}^i}{2}\right) \cdot \delta^2\boldsymbol{t}^i + \left(\delta\boldsymbol{t}^i \cdot \frac{\boldsymbol{k}^i \otimes \boldsymbol{T}^i + \boldsymbol{T}^i \otimes \boldsymbol{k}^i}{4\,(1+\boldsymbol{T}^i \cdot \boldsymbol{t}^i)} \cdot \delta\boldsymbol{t}^i\right) \boldsymbol{t}^i - (\delta\boldsymbol{t}^i \otimes \delta\boldsymbol{t}^i) \cdot \frac{\boldsymbol{k}^i}{2} \end{array} \tag{4.23}$$

where for any vector $\boldsymbol{a}$, $\boldsymbol{a}_\times$ is the linear operator

$$\boldsymbol{a}_\times : \boldsymbol{u} \mapsto \boldsymbol{a} \times \boldsymbol{u} \tag{4.24}$$

and $\boldsymbol{k}^i$ is the binormal defined by

$$\boldsymbol{k}^i = \frac{2\,\boldsymbol{T}^i \times \boldsymbol{t}^i}{1 + \boldsymbol{T}^i \cdot \boldsymbol{t}^i}\ ; \tag{4.25}$$

- **directors rotation** d^i from equation (4.11),

$$\begin{array}{rcl} \delta\hat{\boldsymbol{d}}^i & = & \delta\varphi^i \boldsymbol{t}^i + \delta\hat{\boldsymbol{p}}^i, \\ \delta^2\hat{\boldsymbol{d}}^i & = & \delta\varphi^i\, \delta\boldsymbol{t}^i + \delta^2\hat{\boldsymbol{p}}^i; \end{array} \tag{4.26}$$

- **rotation gradient** q_i from equation (4.14),

$$\begin{array}{rcl} \delta\hat{\boldsymbol{q}}_i & = & \overline{d^{i-1}} * (\delta\hat{\boldsymbol{d}}^i - \delta\hat{\boldsymbol{d}}^{i-1}), \\ \delta^2\hat{\boldsymbol{q}}_i & = & \overline{d^{i-1}} * (\delta^2\hat{\boldsymbol{d}}^i - \delta^2\hat{\boldsymbol{d}}^{i-1}) + \delta\hat{\boldsymbol{q}}_i \times (\overline{d^{i-1}} * \delta\hat{\boldsymbol{d}}^{i-1}); \end{array} \tag{4.27}$$

- **discrete bending and twisting strain measure vector** $\boldsymbol{\kappa}_i$ from equation (4.16),

$$\begin{array}{rcl} \delta\boldsymbol{\kappa}_i & = & \mathcal{I}\left(\delta\hat{\boldsymbol{q}}_i\, q_i\right), \\ \delta^2\boldsymbol{\kappa}_i & = & \mathcal{I}\left(\left(\delta^2\hat{\boldsymbol{q}}_i - \frac{\delta\hat{\boldsymbol{q}}_i \cdot \delta\hat{\boldsymbol{q}}_i}{2}\right) q_i\right), \end{array} \tag{4.28}$$

where $\mathcal{I}(q) = \frac{q-\overline{q}}{2}$ denotes the vector part of a quaternion q.

- **stretching measure** ε^i from equation (4.17),

$$\begin{array}{rcl} \delta\varepsilon^i & = & \frac{\boldsymbol{x}_{i+1}-\boldsymbol{x}_i}{\ell} \cdot (\delta\boldsymbol{x}_{i+1} - \delta\boldsymbol{x}_i), \\ \delta^2\varepsilon^i & = & \frac{1}{\ell}\,(\delta\boldsymbol{x}_{i+1} - \delta\boldsymbol{x}_i) \cdot (\delta\boldsymbol{x}_{i+1} - \delta\boldsymbol{x}_i). \end{array} \tag{4.29}$$

In these formula, the first and second variations of the rotations p^i, d^i and q_i are not captured by quaternions but by regular *vectors*, bearing a hat, such as $\delta\hat{\boldsymbol{p}}^i$, $\delta^2\hat{\boldsymbol{p}}^i$, $\delta\hat{\boldsymbol{d}}^i$, etc. Equations (4.22–4.29) involve standard calculations from Euclidean geometry:

the more advanced quaternion calculus is only required in the proof given in the supplementary materials.

Equations (4.22–4.29) suffice to calculate the strain gradients. They can be implemented easily and efficiently using standard libraries for vector and matrix algebra. These formulas for the first and second gradient of strain are considerably simpler than those applicable to the discrete strain measures used in earlier work on Discrete elastic rods [46, 56, 34, 42].

In equations (4.22–4.29), the perturbations to the degrees of freedom such as $\delta \boldsymbol{x}_i$ and $\delta \varphi^i$ are dummy variables. The first-order variations such as $\delta \boldsymbol{t}^i$, $\delta \hat{\boldsymbol{p}}^i$, must be represented numerically as linear forms, by storing their coefficients as vectors. Similarly, the second-order variations such as $\delta^2 \boldsymbol{t}^i$, $\delta^2 \hat{\boldsymbol{p}}^i$, etc. are represented as quadratic forms, whose coefficients are stored as sparse symmetric matrices; the reader is referred to [42] for further details on this aspect of implementation. All these coefficients depend on the current configuration and must be updated whenever the degrees of freedom $\boldsymbol{X}$ or the reference configuration change.

These vectors and symmetric matrices should be stored at an appropriate place in the data structure representing the Discrete elastic rod. The tensors representing $\delta \boldsymbol{t}^i$, $\delta \hat{\boldsymbol{p}}^i$, $\delta^2 \hat{\boldsymbol{p}}^i$ and $\delta^2 \hat{\boldsymbol{d}}^i$ depend on the perturbations $\delta \boldsymbol{x}_i$ and $\delta \boldsymbol{x}_{i+1}$ to the nodes adjacent to a given segment, and therefore best stored in the data structure representing segments, which have access naturally to the degrees of freedom of the adjacent nodes. The quantities $\delta \hat{\boldsymbol{d}}^i$ and $\delta^2 \hat{\boldsymbol{d}}^i$ make use of the twisting angle $\delta \varphi^i$ in addition to the adjacent nodes $\delta \boldsymbol{x}_i$ and $\delta \boldsymbol{x}_{i+1}$, and should be stored in the data structure representing the material frame attached to particular segment. The quantities $\delta \hat{\boldsymbol{q}}_i$, $\delta \boldsymbol{\kappa}_i$, $\delta^2 \hat{\boldsymbol{q}}_i$ and $\delta^2 \boldsymbol{\kappa}_i$ are best stored in a data structure representing an elastic hinge at a node, which depends on the material frames at the adjacent segments.

4.4 Constitutive models

The discrete kinematics from Sections 4.2 and 4.3 can be combined with a variety of constitutive laws to produce discrete numerical models for rods that are elastic, viscous, visco-elastic, etc.: the procedure has been documented in previous work, and it is similar to the general approach used in finite-element analysis. Elastic problems are treated by introducing a strain energy function $U(\boldsymbol{X})$, whose gradient with respect to $\boldsymbol{X}$ yields the negative of the discrete elastic forces [46, 42]; while viscous problems are treated by introducing a discrete Rayleigh potential $U(\boldsymbol{X}, \dot{\boldsymbol{X}})$, whose gradient with respect to velocities $\dot{\boldsymbol{X}}$ yields discrete viscous forces [55, 36,

56]. More advanced constitutive models such as visco-elastic laws can be treated by variational constitutive updates of a discrete potential that makes use of the same discrete deformation measures [42]. In [42], it is emphasized that these different constitutive models can be implemented *independently* of the geometric definition of discrete deformation measure. Using this decoupled approach, it is straightforward to combine the kinematic element proposed in the present work with constitutive element from previous work. We illustrate this with the classical, linearly elastic rod in Section 4.4 (Kirchhoff rod model), and a discrete inextensible ribbon model in Section 4.4 (Wunderlich model). The latter is a novel application of the Discrete elastic rod method.

Elastic rods (Kirchhoff model)

The classical, continuous theory of elastic rods uses a strain energy functional $U[\boldsymbol{\kappa}] = \int_0^L E(\kappa_{(1)}(s), \kappa_{(2)}(s), \kappa_{(3)}(s))\,\mathrm{d}s$, where $\kappa_{(I)}(s) = \boldsymbol{\kappa}(s) \cdot \boldsymbol{d}_I(s)$ are the components of the rotation gradient in the frame of directors, see equation (4.3). For an inextensible, linearly elastic rod made of a Hookean material with natural curvature $\kappa_{(0)}$, for instance, the strain energy density is

$$E(\kappa_{(1)}(s), \kappa_{(2)}(s), \kappa_{(3)}(s)) = \frac{1}{2} Y I_1 \kappa_{(1)}^2 + \frac{1}{2} Y I_2 (\kappa_{(2)} - \kappa_{(0)})^2 + \frac{1}{2} \mu J \kappa_{(3)}^2\,, \quad (4.30)$$

where Y and μ are the Young modulus and the shear modulus of the material, I_1 and I_2 are the geometric moments of inertia of the cross-section, and J is the torsional constant.

In the discrete setting, we introduce a strain energy $\sum_i E_i(\boldsymbol{\kappa}_i)$ where the sum runs over all interior nodes i. The strain energy assigned to an interior node i is defined in terms of the strain energy density as

$$E_i(\boldsymbol{\kappa}_i) = \ell\, E\left(\frac{\boldsymbol{\kappa}_i}{\ell}\right), \quad (4.31)$$

(no implicit sum over i), where ℓ is the undeformed length of the segments for a uniform mesh. The factor ℓ in the argument of E takes care of the fact that $\boldsymbol{\kappa}_i$ is an integrated quantity, *i.e.*, it is $\frac{\boldsymbol{\kappa}_i}{\ell} \cdot \boldsymbol{e}_J$ and not just $\boldsymbol{\kappa}_i \cdot \boldsymbol{e}_J$ that converges to the continuous strain $\kappa_{(J)}(s)$; for a non-uniform grid, this ℓ would need to be replaced with the Voronoi length associated with the interior vertex i in undeformed configuration. The factor ℓ in factor of E in equation (4.31) ensures that the discrete sum $\sum_i E_i = \sum_i \ell\, E$ converges to the integral $\int_0^L E\,\mathrm{d}s = U$ [46].

Consider for instance an equilibrium problem with dead forces $\boldsymbol{F}_i$ on the nodes: it is governed by the total potential energy $\Phi(\boldsymbol{X})$ defined in terms of $\boldsymbol{X} = (\boldsymbol{x}_0, \varphi_0, \ldots, \varphi_{N-1}, \boldsymbol{x}_N)$

as

$$\Phi(\boldsymbol{X}) = \sum_{i=1}^{N-1} E_i(\boldsymbol{\kappa}_i(\boldsymbol{x}_{i-1}, \varphi^{i-1}, \boldsymbol{x}_i, \varphi^i, \boldsymbol{x}_{i+1})) - \sum_{i=0}^{N} \boldsymbol{F}_i \cdot \boldsymbol{x}_i. \tag{4.32}$$

This energy is minimized subject to the inextensibility constraints

$$\forall i \in (0, N-1) \qquad \varepsilon^j(\boldsymbol{x}_j, \boldsymbol{x}_{j+1}) = 0. \tag{4.33}$$

In equations (4.32–4.33), the elastic deformation measures $\boldsymbol{\kappa}_i$ and ε^j is reconstructed in terms of the unknown $\boldsymbol{X}$ by the method described in Section 4.2, as expressed by the notation $\boldsymbol{\kappa}_i(\boldsymbol{x}_{i-1}, \varphi^{i-1}, \boldsymbol{x}_i, \varphi^i, \boldsymbol{x}_{i+1})$ and $\varepsilon^j(\boldsymbol{x}_j, \boldsymbol{x}_{j+1})$.

In the case of dead forces, the first and second variations of the total potential energy is derived as

$$\begin{aligned} \delta\Phi &= \textstyle\sum_{i=1}^{N-2} \dfrac{\partial E_i}{\partial \boldsymbol{\kappa}_i} \cdot \delta\boldsymbol{\kappa}_i - \sum_{i=0}^{N-1} \boldsymbol{F}_i \cdot \delta\boldsymbol{x}_i \\ \delta^2\Phi &= \textstyle\sum_{i=1}^{N-2} \left(\delta\boldsymbol{\kappa}_i \cdot \dfrac{\partial^2 E_i}{\partial \boldsymbol{\kappa}_i^2} \cdot \delta\boldsymbol{\kappa}_i + \dfrac{\partial E_i}{\partial \boldsymbol{\kappa}_i} : \delta^2\boldsymbol{\kappa}_i \right), \end{aligned} \tag{4.34}$$

see for instance [42]. Here, $\frac{\partial E_i}{\partial \boldsymbol{\kappa}_i}$ and $\frac{\partial^2 E_i}{\partial \boldsymbol{\kappa}_i^2}$ are the internal stress and tangent elastic stiffness produced by the elastic constitutive model $E_i(\boldsymbol{\kappa}_i)$. The two terms appearing in the parentheses in the right-hand side of $\delta^2\Phi$ are known as the elastic and geometric stiffness, respectively. The first and second variations of the strain, $\delta\boldsymbol{\kappa}_i$ and $\delta^2\boldsymbol{\kappa}_i$, are available from Section 4.3: the equilibrium can be solved using numerical methods that require evaluations of the Hessian of the energy. Note that the Hessian can be represented as a sparse matrix thanks to the local nature of the energy contributions $E_i(\boldsymbol{\kappa}_i(\boldsymbol{x}_{i-1}, \varphi^{i-1}, \boldsymbol{x}_i, \varphi^i, \boldsymbol{x}_{i+1}))$ in equation (4.32).

In the applications presented in the forthcoming sections, we find equilibrium configurations by minimizing $\Phi(\boldsymbol{X})$ in equation (4.32) using the sequential quadratic programming method (SQP) described by [57]; it is an extension of the Newton method for non-linear optimization problems which can handle the non-linear constraints in equation (4.33). It requires the evaluation of the first and second gradient of the energy Φ, see equation (4.34), and of the first gradient of the constraints that are available from equation (4.29). We used an in-house implementation of the SQP method in the `C++` language, with matrix inversion done using the `SimplicialLDLT` method available from the Eigen library [58].

Inextensible elastic ribbons (Wunderlich model)

Ribbons made up of material that are sensitive to light [10, 22] or temperature change [59] have been used to design lightweight structures that can be actuated.

They are easy to fabricate, typically by cutting out a thin sheet of material, and their thin geometry can turn the small strains produced by actuation into large-amplitude motion. For this reason, there has been a surge of interest towards mechanical models for elastic ribbons recently. When the width-to-thickness ratio of a ribbon cross-section is sufficiently large, its mid-surface is effectively inextensible. Sadowsky has proposed a one-dimensional mechanical model for inextensible ribbons [3]. Sadowsky model is one-dimensional but differs from classical rod models in two aspects: one of the two bending modes is inhibited due to the large width-to-thickness aspect-ratio, and the two remaining twisting and bending modes are governed by an *non-quadratic* strain energy potential that effectively captures the inextensible deformations of the ribbon mid-surface. Sadowsky's strain energy is non-convex which can lead to the formation of non-smooth solution representing a micro-structure [60, 61]; to avoid these difficulties, we use the higher-order model of Wunderlich that accounts for the dependence of the energy on the longitudinal gradient of bending and twisting strain [4].

The Wunderlich model has been solved numerically by a continuation method, see for instance the work of [44]. The continuation method is an extension of the shooting method that can efficiently track solutions depending on a parameter [62]. It requires the full boundary-value problem of equilibrium to be specified spelled out, which is quite impractical in the case of Wunderlich ribbons. A recent and promising alternative is the high-order method of [50] that starts from linear and quadratic interpolations of the bending and twisting strains, and treats the center-line position and the directors as secondary (reconstructed) quantities. In the present work, we explore an alternative approach, and show that simulations of the Wunderlich model are possible with limited additional work on top of the generic Discrete elastic rod framework.

We build on the work of [5] who have shown that the Wunderlich model can be viewed as a special type of a non-linear elastic rod, see also [63]. Accordingly, simulations of the Wunderlich model can be achieved using a simple extension of the Discrete elastic rod model, which we describe now. We first introduce a geometric model for a *discrete inextensible ribbon*, in which the inextensibility of the mid-surface is fully taken into account. We start from a rectangular strip lying in the plane spanned by $(\boldsymbol{e}_1, \boldsymbol{e}_3)$, as shown in Figure 4.3a. Through every node (shown as black dots in the figure), we pick a folding direction within the plane of the strip (brown dotted line in the figure); we denote by $\pi/2 - \gamma_i$ the angle of the fold line

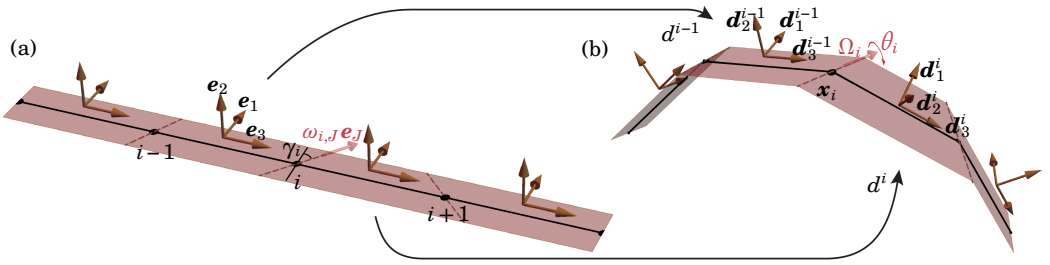

Figure 4.3: A discrete inextensible ribbon: (a) flat configuration and (b) current (folded) configuration obtained by folding along the generatrices (brown dashed lines) by an angle θ_i. By the inextensibility condition, the fold line through vertex $\boldsymbol{x}_i$ in current configuration lies at the intersection of the adjacent faces, *i.e.*, of the planes spanned by $\boldsymbol{d}_1^{i-1}$ and $\boldsymbol{d}_3^{i-1}$ on the one hand and by $\boldsymbol{d}_1^i$ and $\boldsymbol{d}_3^i$ on the other hand.

relative to the centerline. Next, we fold along each one of these lines by an angle θ_i, as shown in Figure 4.3b. We call the resulting surface a discrete inextensible ribbon. By construction, it is isometric to the original strip.

Let us now introduce the director frames $\boldsymbol{d}_I^i$ following rigidly each one of the faces: the planar faces are spanned by the directors $\boldsymbol{d}_1^i$ and $\boldsymbol{d}_3^i$. By construction the vector $\boldsymbol{\Omega}_i$ for the rotation that maps one frame, $\boldsymbol{d}_I^{i-1}$, to the next, $\boldsymbol{d}_I^i$, see equation (4.20), is aligned with the fold line. We observe that the unit tangent along the fold direction is $\boldsymbol{e}_3 \sin\gamma_i + \boldsymbol{e}_1 \cos\gamma_i$ in the flat configuration of the strip; it is therefore mapped to $\boldsymbol{d}_3^{i-1} \sin\gamma_i + \boldsymbol{d}_1^{i-1} \cos\gamma_i = \boldsymbol{d}_3^i \sin\gamma_i + \boldsymbol{d}_1^i \cos\gamma_i$ in the current configuration. In view of this, we conclude

$$\boldsymbol{\Omega}_i = \left(\boldsymbol{d}_3^{i-1} \sin\gamma_i + \boldsymbol{d}_1^{i-1} \cos\gamma_i\right) \theta_i = \left(\boldsymbol{d}_3^i \sin\gamma_i + \boldsymbol{d}_1^i \cos\gamma_i\right) \theta_i.$$

Comparing with equation (4.21), we obtain the discrete deformation measure in the developable ribbon as $\omega_{i,1} = \theta_i \cos\gamma_i$ (bending mode), $\omega_{i,2} = 0$ (inhibited bending mode) and $\omega_{3,i} = 0$ (twisting mode). Eliminating θ_i, we find $\omega_{i,2} = 0$ and $\frac{\omega_{i,3}}{\omega_{i,1}} = \tan\gamma_i$, which can be rewritten in terms of the original discrete strain $\boldsymbol{\kappa}_i = (\kappa_{i,1}, \kappa_{i,2}, \kappa_{i,3})$ with the help of equation (4.18) as

$$\begin{aligned} \kappa_{i,2} &= 0 \\ \kappa_{i,3} &= \eta_i\, \kappa_{i,1}\,, \end{aligned} \tag{4.35}$$

where

$$\eta_i = \tan\gamma_i.$$

The continuous version of the developability conditions is $\kappa_2(s) = 0$ and $\kappa_3(s) = \eta(s)\,\kappa_1(s)$, where $\eta(s) = \tan\gamma(s)$ and $\pi/2 - \gamma(s)$ is the angle between the generatrix

and the tangent, see for instance [5]. It is remarkable that the discrete developability conditions (4.35) are identically satisfied. This is a consequence of the simple geometric interpretation for the discrete deformation measures introduced in Section 4.2.

To simulate inextensible ribbons, we introduce the unknown η_i as an additional degree of freedom at each one of the interior nodes, and we use in equation (4.32) a strain energy density directly inspired from that of Wunderlich [5, 44]

$$E_i(\boldsymbol{\kappa}_i, \eta_{i-1}, \eta_i, \eta_{i+1}) = \frac{D\,w}{2\,\ell}\kappa_{i,1}^2\,(1+\eta_i^2)^2\,\frac{1}{w\,\eta_i'}\,\ln\left(\frac{1+\frac{1}{2}\,\eta_i'\,w}{1-\frac{1}{2}\,\eta_i'\,w}\right). \tag{4.36}$$

In equation (4.36), $D = \frac{Y\,h^3}{12\,(1-\nu^2)}$ is the bending modulus from plate theory, h is the thickness, w is the width, and ℓ is the discretization length. The quantity η_i' is calculated by a central-difference approximation of the gradient of η,

$$\eta_i' = \frac{\eta_{i+1} - \eta_{i-1}}{2\,\ell},$$

where ℓ is the mesh size. The constraint $(4.35)_2$ is imposed at each node using the SQP method. Introducing the nodal degrees of freedom η_i together with the constraint $(4.35)_2$ allows us to work around calculating $\eta_i = \kappa_{i,3}/\kappa_{i,1}$, which is a division with a potentially small denominator; in addition, this approach warrants that $\kappa_{i,3} = 0$ whenever $\kappa_{i,1} = 0$, which is necessary for the Wunderlich energy to remain finite.

It is a feature of the Wunderlich model that η can take on arbitrary values in intervals where κ_1 vanishes identically. To work around this, we have introduced an artificial drag on the η_i's between iterations of the solve. When convergence is reached, the drag force is identically zero.

The discrete potential energy $\Phi(\boldsymbol{X})$ is minimized by the same numerical method as described in Section 4.4, taking into account the kinematic constraints (4.35) and the centerline inextensibility (4.33).

4.5 Illustrations

In this section, the Discrete elastic rod model is used to simulate

- a linearly elastic model for an isotropic beam, Section 4.5,
- a linearly elastic model for an anisotropic beam with natural curvature, Section 4.5,

- Sano and Wada's extensible ribbon model, Section 4.5,
- Wunderlich's inextensible ribbon model, Section 4.5.

These examples serve to illustrate the capabilities of the model. In addition, comparison with reference solutions available from the literature provide a verification of its predictions.

Euler buckling

We consider Euler buckling for a planar, inextensible elastic rod that is clamped at one endpoint. We consider two types of loading: either a point-like force f_p at the endpoint opposite to the clamp, or a force f_d distributed along the length of the rod. In both cases, the force is applied along the initial axis of the rod, is invariable (dead loading), and is counted positive when compressive. A sketch is provided in Figure 4.4.

Mathematically, the equilibria of the rod having bending modulus B are the stationary points of the functional $\Phi = \int_0^L \frac{B}{2}\,\theta'^2(s)\,\mathrm{d}s + f_\mathrm{p}\,x(L)$ (point load) or $\Phi = \int_0^L \left(\frac{B}{2}\,\theta'^2(s) + f_\mathrm{d}\,x(s)\right)\,\mathrm{d}s$ (distributed load), subject to the clamping condition $\theta(0) = 0$. The coordinates of a point on the centerline $(x(s), y(s))$ are reconstructed using the inextensibility condition as $x(s)\,\boldsymbol{e}_1 + y(s)\,\boldsymbol{e}_2 = \int_0^s (\cos\theta\,\boldsymbol{e}_1 + \sin\theta\,\boldsymbol{e}_2)\,\mathrm{d}s$.

The boundary-value equilibrium problem for the Elastica is obtained by the Euler-Lagrange method as

$$0 = B\,\theta''(s) + \sin\theta(s) \times \begin{cases} f_\mathrm{p} & \text{(point-like load)} \\ f_\mathrm{d}\,(L-s) & \text{(distributed load)} \end{cases} \qquad \theta(0) = 0 \qquad \theta'(L) = 0. \tag{4.37}$$

By writing this problem in dimensionless form, one can effectively set the bending modulus, the length and the load to $B = 1$, $L = 1$, and $f_\mathrm{p} = \overline{f}_\mathrm{p}$ (point-like load) or $f_\mathrm{d} = \overline{f}_\mathrm{d}$ (distributed load), where the dimensionless load is

$$\overline{f}_\mathrm{p} = \frac{f_\mathrm{p}}{B/L^2} \qquad \overline{f}_\mathrm{d} = \frac{L\,f_\mathrm{d}}{B/L^2}. \tag{4.38}$$

The critical buckling loads are found by solving the *linearized* version of the buckling problem (4.37) (linear bifurcation analysis),

$$\begin{aligned} \left(\overline{f}_\mathrm{p}\right)_\mathrm{crit} &= \tfrac{\pi^2}{4} && \text{(point-like load)} \\ \left(\overline{f}_\mathrm{d}\right)_\mathrm{crit} &= 7.837 && \text{(distributed load)} \end{aligned} \tag{4.39}$$

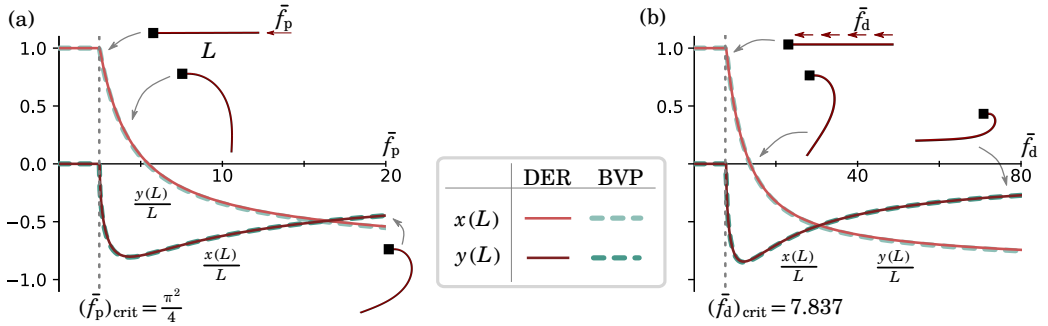

Figure 4.4: Buckling of a planar Elastica subject to (a) a point-like force applied at the endpoint and (b) a distributed force. Comparison of the solutions of the boundary-value problem (4.37) by a numerical shooting method (dashed curves) and of the Discrete elastic rod method (solid curves): the scaled coordinates of the endpoint $s = L$ are plotted as a function of the dimensionless load. The dotted vertical line is the first critical load predicted by a linear bifurcation analysis from equation (4.39).

Numerical simulations of this Euler buckling problem are conducted using the Discrete elastic rod method, as explained in Section 4.32. Simulations are set up with $B = 1$, $L = 1$, number of nodes $N = 100$. In view of this we expect to the buckling loads to be $f_d = \overline{f}_d$ $f_p = \overline{f}_p$. The inextensibility constraint is enforced exactly using SQP. The clamped boundary is enforced by fixing the first and second nodes as well as the first frame.

The typical simulation time is about 1/10s for each equilibrium on a personal computer, and the results are shown in Figure 4.4, and compared to that obtained by solving (4.37) using the `bvp4c` solver from Matlab. A good agreement on the position of the endpoint of the rod is found in the entire post-bifurcation regime. In addition, the onset of bifurcation agrees accurately with the prediction (4.39) from the linear stability analysis.

Folding of an over-curved ring

A circular elastic ring with length L can buckle out of plane if its natural natural curvature $\kappa_{(0)}$ does not match the curvature $2\pi/L$ of the circle with length L. In the case of an over-curved ring, such that $\kappa_{(0)} > 2\pi/L$, a buckled shape featuring two symmetric lobes has been reported [64, 59, 65]. Here, we simulate the buckling of over-curved rings using the Discrete elastic rod model and compare the results to the experimental shapes reported by [64].

In the experiments of [64], a commercial slinky spring with a width $w = 5$ mm,

thickness $t = 2\,\text{mm}$ and length $L = 314\,\text{mm}$ is used; Poisson's ratio has been measured as $\nu = 0.41$. Note that the aspect-ratio $t/w = 0.4$ is not small. In our simulations, we use a discrete version of the quadratic strain energy for a linearly elastic rod having an anisotropic cross-section ($I_1 \neq I_2$), see equations (4.30–4.32). We use the elastic moduli reported in the supplement of [64]:

$$Y\,I_1 = Y\,\frac{w\,t^3}{12} \qquad Y\,I_2 = Y\,\frac{w^3\,t}{12} \qquad \mu\,J = Y\,\frac{0.256\,w\,t^3}{2\,(1+\nu)}. \tag{4.40}$$

The value 0.256 in the numerator was obtained by [64] from the book of [66], and applies to the particular commercial Slinky used in their experiments. In the absence of applied loading, the value of the Young modulus is irrelevant and we set $Y = 1$ in the simulations.

The equilibria of the Discrete elastic rod are calculated numerically for different values of the dimensionless loading parameter $O = 2\,\pi\,\kappa_{(0)}/L$, with $O > 1$ corresponding to the over-curved case. We use $N = 400$ nodes. We start from a circular configuration having curvature $\kappa_{(0)} = 2\,\pi/L$. The Discrete elastic rod model is closed into a ring as follows: the first two nodes and the last two nodes are prescribed to $\boldsymbol{x}_0 = \boldsymbol{x}_{N-1} = \boldsymbol{0}$ and $\boldsymbol{x}_1 = \boldsymbol{x}_N = \ell\,\boldsymbol{e}_x$, respectively; the first and last frames are also fixed, such that $\boldsymbol{d}_1^0 = \boldsymbol{d}_1^{N-1} = \boldsymbol{e}_y$. Next, the over-curvature $\kappa_{(0)}$ is varied incrementally. For each value of $\kappa_{(0)}$, an equilibrium configuration is sought, and we extract the minimal distance D between pairs of opposite points on the ring. In Figure 4.5, the scaled distance D is plotted as a function of O. A good agreement is found with the experiments over the entire range of values of the over-curvature parameter $O > 1$. The simulations correctly predict a planar, triply covered circular solution for $O > O_\text{d} \approx 2.85$, as seen in the experiments.

Buckling of a bent and twisted ribbon

We now turn to an effective rod model applicable to thin ribbons. Sano and Wada [67] have proposed an effective beam model that accounts for the stretchability of the ribbon having moderate width, thereby improving on Sadowsky's inextensibility assumption. A discrete version of their continuous model is of the form (4.32) with a strain energy per elastic hinge

$$E_i(\kappa_1, \kappa_2, \kappa_3) = \frac{1}{2\,\ell}\left(A_1\,\kappa_1^2 + A_2\left(\kappa_2^2 + \frac{\kappa_3^4}{\ell^2/\xi^2 + \kappa_2^2}\right) + A_3\,\kappa_3^2\right). \tag{4.41}$$

Here, ℓ is the uniform segment length in undeformed configuration, $A_1 = Y\,h\,w^3/12$ and $A_2 = Y\,h^3\,w/12$ are the initial bending moduli, $A_3 = Y\,h^3\,w/[6\,(1+\nu)]$ is the

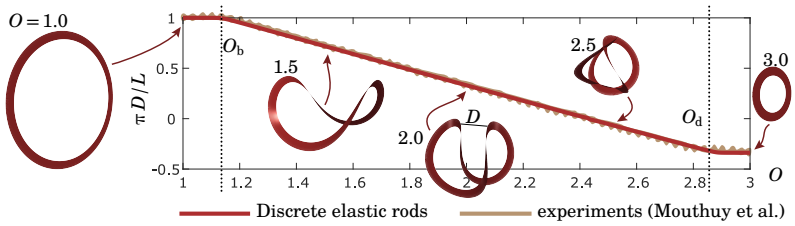

Figure 4.5: Equilibrium of an over-curved elastic ring. Material and geometric parameters correspond to the slinky used by [64] (see main text for values). a) Equilibrium configurations for different values of the over-curvature ratio O. b) Minimal distance of approach D as a function of O: comparison of Discrete elastic rod simulations and experiments [64]. The simulations reproduces both the initial buckling at O_b, and the 'de-buckling' into a flat, triply covered ring at O_d.

initial twisting modulus and $\xi^2 = (1-\nu^2)\, w^4/60\, h^2$. The parameter ξ is the typical length-scale where the stretchability of the mid-surface starts to play a role. The potential E_i from equation (4.41) is non-quadratic, meaning that the equivalent rod has non-linear elastic constitutive laws.

The elastic model (4.41) of Sano and Wada is applicable to thin ribbons, for $w \gg h$. It is based on kinematic approximations. A refined version of their model has been obtained very recently by [45], by asymptotic expansion starting from shell theory; in the latter work, a detailed discussion of the validity of the various models for thin ribbons can also be found. We do not expect any difficulty in applying the present numerical model to the ribbon model in [45]. Both the models of Sano and Wada, and of Audoly and Neukirch improve on Wunderlich model by addressing the stretchability of the ribbon; unlike the Wunderlich model, however, they ignore the dependence of the energy on η', and therefore account less accurately for the 'conical' singularities often observed in ribbons [68] as η varies quickly there.

Following [67], we consider the buckling of a ribbon with length $L = \pi R$ bent into half a circle, whose ends are twisted in an opposite senses by an angle ϕ, see Figure 4.6. Specifically, they identified a snapping instability which occurs for moderately wide ribbons, when the width $w < w^*$ is below a threshold $w^* \approx 1.24\sqrt{L\,h}$, but not for wider ribbons, when $w > w^*$; they showed that their equivalent rod model can reproduce this instability, as well as its disappearance for larger widths. In Figure 4.6, we compare the predictions of a Discrete elastic rod model using (4.41) with the original experiments and simulations from [67]. Our simulations use $N = 350$ vertices each. Our simulation results are in close agreement with both their experimental and numerical results. In particular, we recover the instability

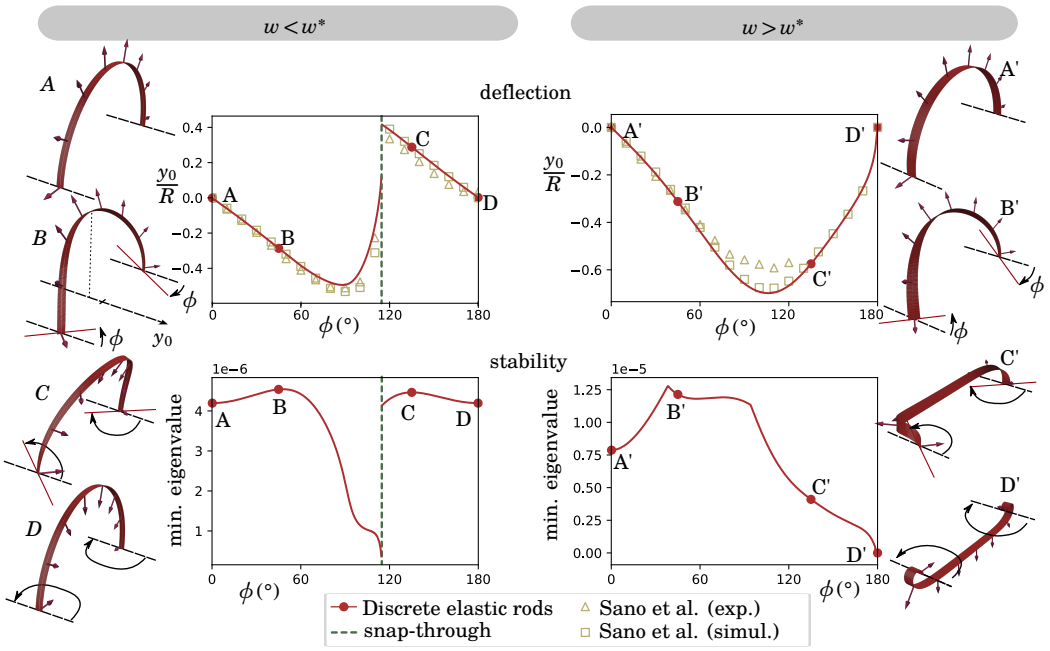

Figure 4.6: Equilibria of an extensible ribbon, as captured by Sano and Wada's equivalent rod model, see equation (4.41). *Top row*: equilibrium diagram showing the scaled value of the deflection y_0 at the center of the ribbon as a function of the twisting angle ϕ at the endpoints. Comparison of the experiments (triangles) and simulations (squares) from [67] with simulations using the Discrete elastic rod model (solid curves and circles). *Left column*: moderately wide ribbon $(h, w, R) = (0.2, 8, 108)$mm showing a snapping instability; *Right column*: wider ribbon $(h, w, R) = (0.2, 15, 108)$mm, in which the instability is suppressed. *Bottom row*: smallest eigenvalues of the tangent stiffness matrix, on the same solution branch shown as shown in the plot immediately above: the presence of an instability for $w < w^*$ (left column) is confirmed by the fact that the smallest eigenvalue reaches zero when the instability sets in.

when $w < w^*$ only.

The elastic Möbius band

An extension of the Discrete elastic rod model that simulates the inextensible ribbon model of Wunderlich has been described in Section 4.4, see equation (4.36). With the aim to illustrate and verify this discrete model, we simulate the equilibrium of a Möbius ribbon, and compare the results to those reported in the seminal paper of Starostin and van der Heijden [43]. In our simulations, the inextensible strip is first bent into a circle, and the endpoints are turned progressively twisted by an angle of 180° to provide the correct topology. The final equilibrium shapes are then recorded for all possible values of the aspect-ratio w/L. For these final equilibrium shapes,

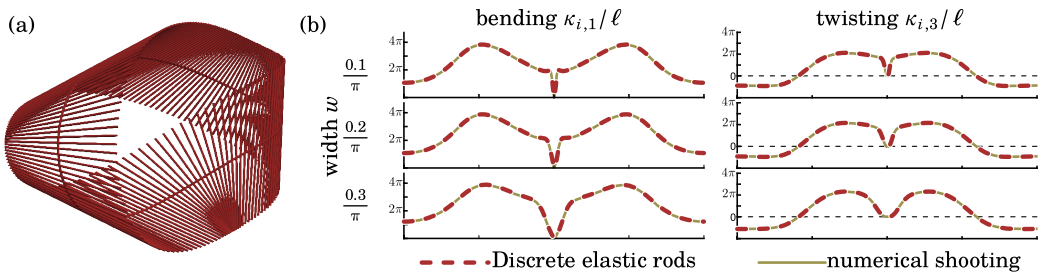

Figure 4.7: Simulation of an inextensible Möbius strip with $L = 1$. (a) Equilibrium width $w = 1/(2\pi)$, as simulated by the Discrete elastic rod model from Section 4.4 with $N = 150$ nodes. (b) Distribution of bending and twisting: Discrete elastic rod simulations with $N = 250$ vertices (dashed curves) versus solution of [43] obtained by numerical shooting (solid curves); the latter have been properly rescaled to reflect our conventions.

the conditions $\boldsymbol{x}_0 = \boldsymbol{x}_{N-1} = \boldsymbol{0}$ and $\boldsymbol{x}_1 = \boldsymbol{x}_N = \ell\, \boldsymbol{e}_x$ hold as earlier, and the orientation of the terminal material frames are such that $\boldsymbol{d}_1^0 = +\boldsymbol{e}_y$ and $\boldsymbol{d}_1^{N-1} = -\boldsymbol{e}_y$.

The equilibrium shape for a particular aspect-ratio $w/L = 1/(2\pi)$ is shown in Figure 4.7a, with arc-length $L = 1$, width $w = 1/(2\pi)$ and $N = 150$ simulation nodes. A detailed comparison with the results of [43] is provided in Figure 4.7b, where the scaled bending and twisting strains $\kappa_{i,1}/\ell$ and $\kappa_{i,3}/\ell$ from the discrete model with $N = 250$ vertices are compared to the strains $\kappa_1(s)$ and $\kappa_3(s)$ obtained by [43] using numerical shooting, for different values of the width w.

4.6 Conclusion

We have presented a new formulation of the Discrete elastic rod model. The formulation is concise and uses only the minimally necessary degrees of freedom: the position of the nodes and the angle of twist of the segments between the nodes. It naturally incorporates the adaptation condition without the need for any constraint, penalty or Lagrange multiplier. We use bending and twisting deformation measures that are different from those used in earlier work on Discrete elastic rods, are equally consistent with their continuum counterparts, and have a simple physical interpretation in the discrete setting. Consequently, the formulation is versatile in the sense that it can be combined with a variety of linear and nonlinear as well as elastic and inelastic constitutive relations. In fact, ribbons can be incorporated as generalized rods with a nonlinear constitutive model. Similarly, the formulation can be used both for static and dynamic simulations.

We have presented explicit formulae for the first and second derivatives of the

deformation measures that eases implementation. We have demonstrated our method with four examples, and verified our results against prior experimental and theoretical findings in the literature.

The source code used for the numerical simulation is available through CaltechDATA at `https://data.caltech.edu/records/2147`.

Chapter 5

LEAPING LIQUID CRYSTAL ELASTOMER PLATES

5.1 Introduction

In this chapter, we study the snap-through buckling of plates of liquid crystal elastomers and the applications of this snap-through buckling to leaping-enabled locomotion. Soft robotics, where soft and stimuli-responsive materials are incorporated into robotic devices [69], are of promise for bio-medical and other applications involving the interactions of robotic devices with humans. A particular challenge in this direction is locomotion. Crawling and walking has been demonstrated in soft materials, especially pneumatics [70, 71, 72, 73, 74]. However, there are few demonstrations of leaping. Despite this, nature is replete with a number of examples such as grasshoppers [75], frogs [76, 77], and kangaroo rats [78], which utilize snap-through to enhance jumping behaviors.

Snap-through transitions in soft materials have been explored using gradients in crosslink density [79], light exposure [80, 19], swelling [81], and pressure [82]. One particular class of materials capable of generating snap-through is liquid crystalline elastomers. As discussed in Section 1.2, the thermomechanical response of LCEs to heat is associated with thermotropic disruption of order, in which the material undergoes a nematic-to-isotropic transition. Alignment and retention of mesogen orientation upon polymerization has been utilized to prepare LCEs with distinctive deformations ranging from uniaxial contraction [7], bending [83], or shape morphing [84, 85]. While useful in instances such as weight-lifting [86] and gripping or moving objects [87], thermomechanical deformation of LCE are inherently slow [88]. Here, we explore a route to bridging the gap between snap-through instabilities and programmability of LCEs to achieve rapid actuations.

We study LCE laminates with spatial variation in the director [89, 90, 91] and through-thickness variation in modulus. These materials undergo thermally-induced mechanical instabilities that lead to leaping of the material to heights of over 200x the material thickness as a result of a rapid snap-through transition. To elucidate the mechanics of the stimuli-response, we develop a model based on theory of inhomogenous plates. The model is then used as a design tool to inform experimental investigation of variables relating to the material design and geometrical constrains.

The culmination of this effort is the realization of directional leaping, analogous to the motility of grasshoppers, facilitated by including “legs” of different lengths.

5.2 Layered liquid crystal elastomer sheets

Plates and sheets demonstrate a variety of strange behaviors, particularly when under the influence of spontaneous strains and curvatures. Various researchers [89, 90, 91] demonstrate how a +1 topological defect in LCE patterning can be actuated to create a conical shape, lifting many times the weight of the sheet. These systems, however, suffer from a problem of multi-stability with equivalent up and down snapped configurations. Therefore, when actuating, both modes are equally favorable. Additionally, once locked into either the up or down configuration, the energy barrier between each mode is very high. By carefully designing such systems, we can utilize this energy barrier for locomotion.

One mechanism to utilize this energy is to use laminated sheets of LCEs with differing material properties to induce a snap-through behavior. Lightly crosslinked LCEs have a lower Young’s modulus compared to highly crosslinked LCEs, however they also demonstrate a much higher spontaneous strain relative to that of the highly crosslinked LCE at a fixed temperature. By layering lightly and highly crosslinked materials, we can generate and design complex deformation pathways.

We consider the configuration shown in in Figure 5.1D by layering the LCEs in a low, low, high modulus configuration and placing the high modulus side in contact with a hot plate. Initially, the side in contact with the hot plate (high modulus) will contract. Due to the +1 topological defect patterning, the system will contract radially, preferring a conical shape. Because, initially, only the high modulus side is a significantly higher temperature than the low modulus side, a spontaneous curvature will develop simultaneously, biasing the conical shape to one side. As heat saturates the sheet, the spontaneous strains on the lightly crosslinked side will "pull" harder than the highly crosslinked side, biasing curvature in the opposite direction. Given a sufficiently high inverting curvature, the sheet will experience a rapid inversion through snap-through.

This system is explored theoretically and computationally in the following sections with experimental collaboration and validation by Hebner et al. Their work, particularly the material characterization, is given in more detail in Appendix A.3.

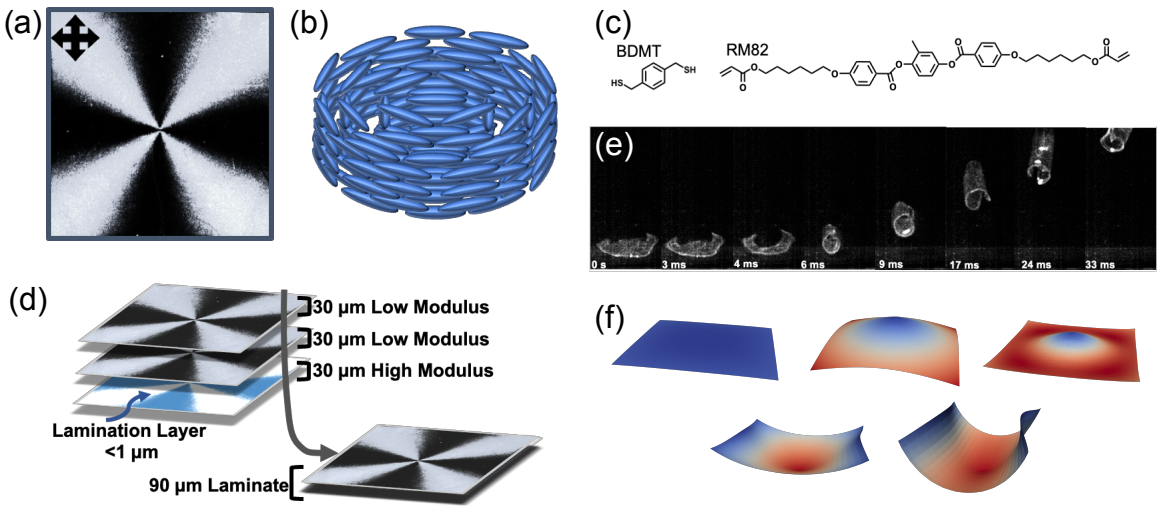

Figure 5.1: Leaping LCEs. (A) The birefringence associated with spatial variation of the nematic director described as a +1 topological defect is viewed in an LCE placed between crossed polarizers. (B) The nematic director in the LCE films rotates concentrically around a central point. (C) The LCE were prepared by free radical chain transfer polymerization between the liquid crystalline monomer (C6M) and dithiol (benzenedimethanethiol, BDMT). (D) The LCE elements were prepared by stacking patterned LCEs to create laminates with variation of modulus through the thickness. The total thickness of the LCE laminate was 90 mm. (E) Upon heating, the laminated LCEs leap from the hot surface.

5.3 Model development and validation

We develop a model based upon the Föppl-von Kármán plate theory coupled to heat transfer. Briefly, we compute the temperature distribution through the thickness at each time by solving the heat equation, and the mechanical equilibrium using the Föppl-von Kármán plate theory with thermally induced spontaneous in-plane strain $\boldsymbol{\epsilon}_m$ and spontaneous curvature $\boldsymbol{\kappa}_m$. These, as well ast he effective in-plane and bending modulus of the sheet, are computed from 3D elasticity with thermal strain $\hat{\epsilon}_{\alpha\beta}$ by enforcing equilibrium through the thickness of the film and shown in Table 5.1. The total strain energy of the system is written in Equation 5.1 where $\mathbf{x} = \{x_1, x_2\}$, is an element of the flat reference configuration, $\mathbf{u} = \{u_1, u_2\}$ is the in-plane displacement, w is the out-of-plane displacement, $\boldsymbol{\epsilon}_m$ is the spontaneous in-plane strain, and $\boldsymbol{\kappa}_m$ is the spontaneous bending:

$$\mathcal{E} = \int_\Omega \left(CW\left(\frac{1}{2}\left(\nabla\mathbf{u}(\mathbf{x}) + \nabla\mathbf{u}(\mathbf{x})^T\right) + \frac{1}{2}\nabla w(\mathbf{x}) \otimes \nabla w(\mathbf{x}) - \boldsymbol{\epsilon}^m(\mathbf{x})\right) + BW(\nabla^2 w(\mathbf{x}) - \boldsymbol{\kappa}_m(x))\right) da\,, \tag{5.1}$$

where C and B, are the stretching and bending moduli, respectively and

$$W(\boldsymbol{\xi}) = \frac{1}{2(1-\nu^2)}\left(\nu \mathrm{tr}(\boldsymbol{\xi})^2 + (1-\nu)\mathrm{tr}\left(\boldsymbol{\xi}^T\boldsymbol{\xi}\right)\right). \tag{5.2}$$

Note that the Föppl-von Kármán plate theory couples the out-of-plane displacement with the in-plane strain to account for higher order effects of plate deformations, and this coupling is critical to the model. We compute the equilibrium configuration at each time and infer the snap-through as a loss of stability of the equilibrium. Typical results are shown in Figure 5.2E which plots the curvature at the center of the sheet as a function of time, and the insets show the shape.

	In-Plane	**Bending**
Constitutive Relation	$N_{\alpha\beta} = C(\epsilon_{\alpha\beta} - \epsilon^m_{\alpha\beta})$	$M_{\alpha\beta} = B(\kappa_{\alpha\beta} - \kappa^m_{\alpha\beta})$
Modulus	$C = \mathcal{M}^0(E)$	$B = \mathcal{M}^2(E) - \frac{\mathcal{M}^1(E)^2}{\mathcal{M}^0(E)}$
Spontaneous Strain and Curvature	$\epsilon^m_{\alpha\beta} = \frac{\mathcal{M}^0(E\hat{\epsilon}_{\alpha\beta})}{\mathcal{M}^0(E)}$	$\kappa^m_{\alpha\beta} = \frac{1}{B}\left(\mathcal{M}^1(E\hat{\epsilon}_{\alpha\beta}) - \frac{\mathcal{M}^1(E)\mathcal{M}^0(E\hat{\epsilon}_{\alpha\beta})}{\mathcal{M}^0(E)}\right)$

Table 5.1: Equations used to describe evolution of in-plane and bending strain as a function of modulus. Note, $\mathcal{M}^p(f) = \int_{-h/2}^{h/2} z^p f(z)dz$ is the p-th moment through the thickness.

The model predicts that as the LCE laminate is heated from the bottom with the high-modulus side in contact with the surface, positive curvature initially develops. Simultaneously, the system will contract due to the evolution of $\epsilon_{\alpha\beta}$, forming an energy barrier between the up and down solution variants and resulting in a bifurcation. After initial development of positive curvature, the evolution of strain within the material causes a rapid change to net negative curvature. However, as shown in the series of simulations in Figure 5.2E, the configuration of the LCE remains locked into a physical deformation with positive curvature. When a sufficiently high magnitude of negative spontaneous curvature is achieved, the positive curvature solution in the model becomes unstable and the LCE inverts via snap-through to a negative curvature solution, at which point the simulation shows the physical deformation of the LCE into negative curvature. This rapid inversion in curvature is the origin of the leaping motion. Explicit analysis of the energy conversion confirms there is sufficient energy to result in leaping. This scenario presents an interesting method of both inducing snap-through of a free-standing structure as well as having

a thermally driven shape bifurcation with directional dependence. The experimental observations parallel the computational results (Figure 5.2C) thereby validating the model.

Next, the simulation of the natural in-plane strain and curvature is done for the configuration in which the high modulus side is facing upward. Like the previous scenario, the system contracts monotonically as heat saturates through the thickness of the plate. As the system reaches a constant temperature, the value of in-plane strain reaches a constant value. However, in this case, the coupling of the strain generation through the thickness with evolution of temperature does not result in a bifurcation, so no curvature inversion occurs and there is no instability. This again parallels the experiments in (Figure 5.2D), further validating the model. Ultimately, when the evolution of curvature is mapped with the simulated deformation of the LCE laminates as in Figure 5.2E, it becomes plainly evident that snap-through behavior is dependent on the initial placement of the LCE laminates. For all subsequent investigation, only the configuration with the high-modulus side in contact with the hot surface is considered.

5.4 Modeling of active, laminated structures

We model the transient behavior of the sheet up until the point of snap-through. During this period, the sheet deforms slowly in response to changes in temperature distribution and therefore inertial effects are negligible. Further, heat transfer is slow compared to mechanical time scales, and therefore we assume that the body is in mechanical equilibrium at each instant of time. We obtain the temperature profile by solving the heat equation assuming a set temperature on the bottom side and an insulated boundary on the top. The temperature distribution through the thickness gives rise to a spontaneous strain and curvature in the sheet. We obtain these by imposing equilibrium (balance of force and moment) across the cross-section. Given the spontaneous strain and curvature, we use a Föppl-von Kármán plate model to calculate the equilibrium shape, and then study the stability of the equilibrium shape to determine the instant of snap-through.

Evolution of strain

We develop a model for plates with anisotropic cross-sections in the presence of spontaneous strains. The book by Reddy [92] presents an excellent introduction to modeling anisotropic plates, particularly those comprised of laminate composites. We assume a plane state of stress in the sheet, and therefore the Hooke's law may

be written as

$$\sigma^s_{\alpha\beta}(z) = \frac{E(z)}{1-\nu^2}\left(\nu\epsilon^s_{\gamma\gamma}(z)\delta_{\alpha\beta} + (1-\nu)\epsilon^s_{\alpha\beta}(z)\right) = E(z) f_{\alpha\beta\gamma\delta}\epsilon^s_{\gamma\delta}(z)\,, \tag{5.3}$$

where z is the variable through the thickness, the Young's modulus $E(z)$ varies throug hthe thickness while the Poisson's relation ν is uniform. This allows us to write the Hooke's law in the compact form of the second equality. We make the usual ansatz that the through-thickness strain takes the form

$$\epsilon^s_{\alpha\beta}(z) = \kappa_{\alpha\beta}(z - z_0) + \epsilon_{\alpha\beta} - \hat{\epsilon}_{\alpha\beta}(z)\,, \tag{5.4}$$

where $\kappa_{\alpha\beta}$ is the apparent curvature, z_0 is the location of the neural axis, $\epsilon_{\alpha\beta}$ is the in-plane strain, and $\hat{\epsilon}_{\alpha\beta}(z)$ is the spontaneous strain due to the local temperature profile. The traction can be written as

$$\begin{aligned} N_{\alpha\beta} &= \int_{-h/2}^{h/2} \sigma^s_{\alpha\beta}(z)dz = \int_{-h/2}^{h/2} E(z) f_{\alpha\beta\gamma\delta}\left(\kappa_{\gamma\delta} + \epsilon_{\gamma\delta} - \hat{\epsilon}_{\gamma\delta}(z)\right) dz \\ &= f_{\alpha\beta\gamma\delta}\left(\kappa_{\gamma\delta}\left(\mathcal{M}^1(E) - z_0\mathcal{M}^0(E)\right) + \epsilon_{\gamma\delta}\mathcal{M}^0(E) - \mathcal{M}^0(E\hat{\epsilon}_{\gamma\delta})\right)\,. \end{aligned}$$

Setting $z_0 = \frac{\mathcal{M}^1(E)}{\mathcal{M}^0(E)}$, we get

$$N_{\alpha\beta} = C f_{\alpha\beta\gamma\delta}(\epsilon_{\gamma\delta} - \epsilon^m_{\gamma\delta})\,, \tag{5.5}$$

where the effective in-plane modulus is given by $C = \mathcal{M}^0(E)$ and the spontaneous effective in-plane strain is given by $\epsilon^m_{\alpha\beta} = \mathcal{M}^0(E\hat{\epsilon}_{\alpha\beta})$.

The moment is given by

$$\begin{aligned} M_{\alpha\beta} &= \int_{-h/2}^{h/2} z\sigma^s_{\alpha\beta}(z)dz = \int_{-h/2}^{h/2} zE(z) f_{\alpha\beta\gamma\delta}\left(\kappa_{\gamma\delta}(z - z_0) + \epsilon_{\gamma\delta} - \hat{\epsilon}_{\gamma\delta}(z)\right) dz \\ &= f_{\alpha\beta\gamma\delta}\left(\kappa_{\gamma\delta}\left(\mathcal{M}^2(E) - z_0\mathcal{M}^1(E)\right) + \epsilon_{\gamma\delta}\mathcal{M}^1(E) - \mathcal{M}^1(E\hat{\epsilon}_{\gamma\delta})\right) \\ &= f_{\alpha\beta\gamma\delta}\left(\kappa_{\gamma\delta}\left(\mathcal{M}^2(E) - \frac{\mathcal{M}^1(E)^2}{\mathcal{M}^0(E)}\right) + \epsilon_{\gamma\delta}\mathcal{M}^1(E) - \mathcal{M}^1(E\hat{\epsilon}_{\gamma\delta})\right)\,. \end{aligned}$$

Making the assumption that $\epsilon_{\gamma\delta} \approx \epsilon^m_{\gamma\delta}$, we have

$$M_{\alpha\beta} = f_{\alpha\beta\gamma\delta}\left(\kappa_{\gamma\delta}\left(\mathcal{M}^2(E) - \frac{\mathcal{M}^1(E)^2}{\mathcal{M}^0(E)}\right) + \frac{\mathcal{M}^0(E\hat{\epsilon}_{\gamma\delta})\mathcal{M}^1(E)}{\mathcal{M}^1(E)} - \mathcal{M}^1(E\hat{\epsilon}_{\gamma\delta})\right)\,.$$

Defining $B = \mathcal{M}^2(E) - \frac{\mathcal{M}^1(E)^2}{\mathcal{M}^0(E)}$ and $\kappa^m_{\gamma\delta} = \frac{1}{B}\left(\mathcal{M}^1(E\hat{\epsilon}_{\gamma\delta}) - \frac{\mathcal{M}^0(E\hat{\epsilon}_{\gamma\delta})\mathcal{M}^1(E)}{\mathcal{M}^1(E)}\right)$, we have

$$M_{\alpha\beta} = B f_{\alpha\beta\gamma\delta}(\kappa_{\gamma\delta} - \kappa^m_{\gamma\delta})\,. \tag{5.6}$$

These results allow for calculation of the evolution of spontaneous in-plane and bending strain relative to the modulus as described in Table 5.1. Given the relations betwee strains, stresses, and curvatures, we can then construct a Föppl-von Kármán energy of the form

$$\mathcal{E} = \int_\Omega \left(CW(\boldsymbol{\epsilon} - \boldsymbol{\epsilon}_m) + BW(\boldsymbol{\kappa} - \boldsymbol{\kappa}_m)\right) dA\,,$$

where $\boldsymbol{\epsilon} = \frac{1}{2}\left(\nabla\mathbf{u}(\mathbf{x}) + \nabla\mathbf{u}(\mathbf{x})^T\right) + \frac{1}{2}\nabla w(\mathbf{x}) \otimes \nabla w(\mathbf{x})$, $\boldsymbol{\kappa} = \nabla^2 w(\mathbf{x})$, and C, B, $\boldsymbol{\epsilon}_m$, $\boldsymbol{\kappa}_m$ are as defined in the previous work. In this formulation, $\mathbf{u}(x) \in \mathbb{R}^2$ is the in-plane deformation of the neutral plane and $w(x) \in \mathbb{R}$ is the out of plane deformation. W is the normalized strain energy funciton consistent with the plane stress approximation. We take

$$W(\boldsymbol{\epsilon}) = \frac{1}{2(1-\nu^2)}\left(\nu\epsilon_{\alpha\alpha}\epsilon_{\beta\beta} + (1-\nu)\epsilon_{\alpha\beta}\epsilon_{\alpha\beta}\right)\,.$$

Uniform case

As a demonstration of the consistency of the model, consider the case where we have zero thermal stresses ($\hat{\epsilon}_{\alpha\beta} = 0$) and the Young's Modulus is constant $E(z) = E$. We then have that $C = hE$, $B = \frac{h^3}{12}E$, $\boldsymbol{\epsilon}_m = 0$, and $\boldsymbol{\kappa}_m = 0$. We then see that the previous equation condenses to the standard Föppl-von Kármán plate energy of

$$\mathcal{E}_{FvK} = \int_\Omega \left(hEW\left(\frac{1}{2}\left(\nabla\mathbf{u}(\mathbf{x}) + \nabla\mathbf{u}(\mathbf{x})^T\right) + \frac{1}{2}\nabla w(\mathbf{x}) \otimes \nabla w(\mathbf{x})\right) + \frac{h^3 E}{12}W(\nabla^2 w(\mathbf{x}))\right) dA\,. \tag{5.7}$$

Non-dimensionalization

We non-dimensionalize the problem. Let L be a characteristic macroscopic length scale (i.e. the side length of the sample). We then have

$$\bar{h} = \frac{h}{L}\,, \quad \bar{\mathbf{x}} = \frac{\mathbf{x}}{L}\,, \quad \bar{\mathbf{u}} = \frac{\mathbf{u}}{L}\,, \quad \bar{w} = \frac{w}{L}\,, \quad \bar{\Omega} = \frac{\Omega}{L^2}\,. \tag{5.8}$$

Using the chain rule on the gradients, we have

$$\begin{aligned}
\nabla\mathbf{u} &= \nabla(L\bar{\mathbf{u}}) = \bar{\nabla}\bar{\mathbf{u}} \\
\nabla w &= \nabla(L\bar{w}) = \bar{\nabla}\bar{w} \\
\nabla^2 w &= \nabla(\bar{\nabla}\bar{w}) = \frac{1}{L}\bar{\nabla}^2\bar{w}\,,
\end{aligned}$$

where $\bar{\nabla}$ is the gradient with respect to the non-dimensionalized coordinates $\bar{\mathbf{x}}$.

Plugging this in, we have

$$\begin{aligned}\mathcal{E} &= \int_{\Omega} \left(CW(\boldsymbol{\epsilon} - \boldsymbol{\epsilon}_m) + BW(\boldsymbol{\kappa} - \boldsymbol{\kappa}_m)\right) dA \\ &= \int_{\bar{\Omega}} \left(CW(\bar{\boldsymbol{\epsilon}} - \boldsymbol{\epsilon}_m) + BW\left(\frac{1}{L}\bar{\boldsymbol{\kappa}} - \boldsymbol{\kappa}_m\right)\right) L^2 d\bar{A}\,,\end{aligned}$$

where $\bar{\boldsymbol{\epsilon}} = \frac{1}{2}\left(\bar{\nabla}\bar{\mathbf{u}} + \bar{\nabla}\bar{\mathbf{u}}^T\right) + \frac{1}{2}\bar{\nabla}\bar{w} \otimes \bar{\nabla}\bar{w}$ and $\bar{\boldsymbol{\kappa}} = \bar{\nabla}^2\bar{w}$. Because W is a quadratic form, $W(\alpha\mathbf{F}) = \alpha^2 W(\mathbf{F})$ for all $\alpha \in \mathbb{R}$. Defining $\bar{\boldsymbol{\kappa}} = L\boldsymbol{\kappa}_m$, we have

$$\begin{aligned}\mathcal{E} &= \int_{\bar{\Omega}} \left(CW(\bar{\boldsymbol{\epsilon}} - \bar{\boldsymbol{\epsilon}}_m) + \frac{B}{L^2}W(\bar{\boldsymbol{\kappa}} - \bar{\boldsymbol{\kappa}}_m)\right) L^2 d\bar{A} \\ &= L^2 C \int_{\bar{\Omega}} \left(W(\bar{\boldsymbol{\epsilon}} - \bar{\boldsymbol{\epsilon}}_m) + \frac{B}{CL^2}W(\bar{\boldsymbol{\kappa}} - \bar{\boldsymbol{\kappa}}_m)\right) d\bar{A}\,.\end{aligned}$$

This allows us to rescale our problem to a unit scale for numerical stability. Additionally, we obtain a non-dimensionalized form of the energy as

$$\bar{\mathcal{E}} = \frac{\mathcal{E}}{L^2 C} = \int_{\bar{\Omega}} \left(W(\bar{\boldsymbol{\epsilon}} - \bar{\boldsymbol{\epsilon}}_m) + \bar{B}W(\bar{\boldsymbol{\kappa}} - \bar{\boldsymbol{\kappa}}_m)\right) d\bar{A}\,, \tag{5.9}$$

where $\bar{B} = \frac{B}{CL^2}$ is the normalized bending modulus. Minimizing this elastic energy yields equilibrium solutions; but first, we have to obtain the temperature distribution through the thickness.

Heat equation and boundary conditions

We obtain the temperature distribution through the thickness, and its evolution by solving the following heat equation and boundary conditions.

$$\begin{aligned}\frac{\partial T}{\partial t}(z,t) &= D\frac{\partial^2 T}{\partial z^2}(z,t)\,, \\ T\left(-\frac{h}{2}, t\right) &= T_l\,, \\ \frac{\partial T}{\partial z}\left(\frac{h}{2}, t\right) &= 0\,, \\ T(z,0) &= T_0\,.\end{aligned}$$

We solve the above system using the pdepe routine in Matlab to obtain $T(z,t)$. This result can be used in combination with the strain as a function of temperature for different combinations of limated films. For example, with two laminated films (both of height $h/2$), we have

$$\epsilon_{\alpha\beta}(\Delta T, z) = \begin{cases} \epsilon^1_{\alpha\beta}(\Delta T), & z \in (0, h/2) \\ \epsilon^2_{\alpha\beta}(\Delta T), & z \in (-h/2, 0)\,, \end{cases}$$

where $\epsilon^1_{\alpha\beta}(\Delta T)$ and $\epsilon^2_{\alpha\beta}(\Delta T)$ are the (experimentally measured) strain functions for each of the individual laminates. For any given time, we can find the spontaneous strain through the thickness as

$$\hat{\epsilon}_{\alpha\beta}(z) = \epsilon_{\alpha\beta}(T(z,t) - T_0, z)\,, \tag{5.10}$$

where we suppress the explicit dependence on t. Note that this term also encapsulates the radial nature of the patterning on the LCE sheet.

Augmented lagrangian

Having obtained the temperature distribution and the resulting spontaneous stretch and curvature, we seek to study the equilibria associated with the energy (5.9) to obtain the shape of the sheet. This is non-trivial due to the presence of the second derivative $\nabla\nabla w$; so we use an augmented Lagrangian method. We write the strain energy (5.9) compactly as

$$U[\mathbf{u}, w] = \int_\Omega u(\mathbf{u}, \nabla\mathbf{u}, w, \nabla w, \nabla^2 w) dA\,.$$

In general, second derivatives are challenging in a finite element formulation due to discontinuities in the derivatives at the boundaries of each element, requiring C^1 shape functions. This makes it so that the space of finite element shape functions is ill suited to solving these problems. There are other approaches, such as using Hermitian elements [93] or specialized shape functions that are tailored to the physics of the problem. A description of such elements can be found in [94].

By utilizing augmented Lagrangians, we can utilize traditional finite element formulations and packages without significant modification to solve problems with constraints or, in our case, incorporate higher order derivatives into the energy. The idea behind this method is to relax the space of functions where we look for solutions to be outside of the constrained set then, by iterating, we satisfy the constraint more and more until a satisfactory point. This is similar to the approach of "mixed elements" in the Mindlin-Reissner plate theory, as described in [94], with an added quadratic relaxation term in the energy.

In this work, we will use the augmented Lagrangian formulation applied to the Föppl-von Kármán plate model find energy minimizers. We introduce a new function $\boldsymbol{\xi}$ which we constrain as $\boldsymbol{\xi} = \nabla w$.

We enforce this constraint with an augmented Lagrangian written as

$$\mathcal{L}[\mathbf{u}, w, \boldsymbol{\xi}, \boldsymbol{\lambda}] = \int_\Omega u(\mathbf{u}, \nabla\mathbf{u}, w, \nabla w, \nabla\boldsymbol{\xi})dA - \int_\Omega \boldsymbol{\lambda}\cdot(\boldsymbol{\xi}-\nabla w)dA + \frac{\mu}{2}\int_\Omega |\boldsymbol{\xi}-\nabla w|^2 dA\,,$$

where we must also solve for the contribution of the Lagrange multiplier $\boldsymbol{\lambda}$. The weak form of this Lagrangian is found by taking variations and solving for $\delta\mathcal{L}[\mathbf{u}, w, \boldsymbol{\xi}, \boldsymbol{\lambda}] = 0$. Taking this variation, we have

$$\begin{aligned}\delta\mathcal{L}[\mathbf{u}, w, \boldsymbol{\xi}, \boldsymbol{\lambda}] = \int_\Omega \left(\frac{\partial u}{\partial \mathbf{u}}\cdot\delta\mathbf{u} + \frac{\partial u}{\partial\nabla\mathbf{u}}\cdot\nabla\delta\mathbf{u} + \frac{\partial u}{\partial w}\cdot\delta w + \frac{\partial u}{\partial\nabla w}\cdot\nabla\delta w + \frac{\partial u}{\partial\nabla\nabla w}\cdot\nabla\delta\boldsymbol{\xi}\right)dA \\ - \int_\Omega \delta\boldsymbol{\lambda}\cdot(\boldsymbol{\xi}-\nabla w)dA - \int_\Omega \boldsymbol{\lambda}\cdot(\delta\xi - \nabla\delta w)dA \\ + \mu\int_\Omega (\boldsymbol{\xi}-\nabla w)\cdot(\delta\boldsymbol{\xi}-\nabla\delta w)dA\,,\end{aligned}$$

where $\delta\mathbf{u}, \delta w, \delta\boldsymbol{\xi}, \delta\boldsymbol{\lambda}$ are variations with respect to their respective variables. Noting that each of these variations are independent from each other, we note that this can be separated into a set of equations as

$$\begin{aligned}\int_\Omega \left(\frac{\partial u}{\partial \mathbf{u}}\cdot\delta\mathbf{u} + \frac{\partial u}{\partial\nabla\mathbf{u}}\cdot\nabla\delta\mathbf{u}\right)dA = 0 \\ \int_\Omega \left(\frac{\partial u}{\partial w}\cdot\delta w + \frac{\partial u}{\partial\nabla w}\cdot\nabla\delta w + \boldsymbol{\lambda}\cdot\nabla\delta w - \mu(\boldsymbol{\xi}-\nabla w)\cdot\nabla\delta w\right)dA = 0 \\ \int_\Omega \left(\frac{\partial u}{\partial\nabla\nabla w}\cdot\nabla\delta\boldsymbol{\xi} - \boldsymbol{\lambda}\cdot\delta\boldsymbol{\xi} + \mu(\boldsymbol{\xi}-\nabla w)\cdot\delta\boldsymbol{\xi}\right)dA = 0 \\ -\int_\Omega \delta\boldsymbol{\lambda}\cdot(\boldsymbol{\xi}-\nabla w)\,dA = 0\,,\end{aligned}$$

It can be seen that the first three equations are the equilibrium formulation and the final is the constraint satisfaction. In the augmented Lagrangian formulation, finding solutions to these equations is equivalent to finding extrema to the original optimization problem. One aspect to be aware of is that the conversion of a constrained optimization problem to an augmented Lagrangian problem comes with the caveat that minimizers of the original problem can be converted to saddle point problems in this scheme.

Following the standard finite element formulation, we expand both the function and its corresponding variations with Galerkin projections as

$$\mathbf{u}^p(\mathbf{x}) = \sum_i \mathbf{u}^i N_i^u(\mathbf{x}), \quad w^p(\mathbf{x}) = \sum_i w^i N_i^w(\mathbf{x}),$$
$$\boldsymbol{\lambda}^p(\mathbf{x}) = \sum_i \boldsymbol{\lambda}^i N_i^\lambda(\mathbf{x}), \quad \boldsymbol{\xi}^p(\mathbf{x}) = \sum_i \boldsymbol{\xi}^i N_i^\xi(\mathbf{x}),$$

where $N_i^{(\cdot)}$ are the shape functions with compact support. We use 2nd order shape functions in $\mathbf{u}$ and first order for all the rest. The finite element scheme is implemented in Deal.II, a finite element library for C++ [95]. The zero is found using Newton-Raphson iterations where the Hessian is calculated explicitly using second variations of the augmented Lagrangian.

Calculating critical curvatures

We start at the flat shape when the temperature distribution is uniform. At each subsequent time step, we compute the temperature distribution and use it obtain the spontaneous strain and curvature distribution. We use these to compute the new equilibrium shape using the previous shape as an initial guess. This leads to a smooth evolution until system loses stability. This is seen when the Newton-Raphson iteration fails to converge or when the solution jumps significantly. We can then calculate the shape of the snapped configuration. This method provides the verification and demonstration of snap-through as seen in Figure 2E. In order to calculate the relationship between a particular fixed value of in-plane strain and the spontaneous curvature necessary to cause inversion, we calculate the configuration for that fixed value of in-plane strain in the absence of any spontaneous curvature. The inverting curvature is then slowly increased, again leading to smooth deformations, until the Newton-Raphson iteration fails to converge or the solution jumps significantly. At this point, we calculate shape of the snapped configuration and tabulate the critical curvature necessary for inversion as well as the difference in stored strain energies before and after the snap-through. By repeating this process for various values of in-plane strain, we can characterize the relationship between inplane strain and the critical curvature necessary for inversion. This method is used for calculating the results in Figures 3B,C and 4A,B.

Jump height

To estimate the height that the sheet will jomp off the table, we assume that all of the energy released in the snap-through is converted to gravitational potential energy. Calculated in the non-dimensional scheme, the snap-through releases some

$\Delta\bar{\mathcal{E}}$. This can be converted to a dimensional energy as $\Delta\mathcal{E} = L^2 C \Delta\bar{\mathcal{E}}$, where the non-dimensionalization is done as above. We then equate the released energy to the gravitational potential energy as

$$\Delta\mathcal{E} = mg\hat{z}\,,$$

where $\hat{z}$ is the estimated jump height. Rearranging, we have

$$\hat{z} = \frac{L^2 C}{L^2 h\rho g}\Delta\bar{\mathcal{E}} = \frac{C}{\rho g h}\Delta\bar{\mathcal{E}}\,,$$

where we take $m = \rho L^2 h$.

Parameter	Value
C	$1.053 * 10^3$ mPa
h	$90\,\mu m$
ρ	$1.2\,g/cm^3$
g	$9.8\,m/s^2$
$\Delta\bar{\mathcal{E}}$	$2.0 * 10^{-4}$

Table 5.2: Parameters used for calculating the jump heigh of the LCE sheet.

Substituting values from the simulations, we get $\hat{z} \approx 20\,cm$. Interestingly, it seems that regardless of the macroscopic dimension of the system, the jump height is the same. This qualitatively matches the behavior of the experimental system. Note that in reality, there are dissipative processes that reduce the jump height. Some of these include dissipation within the material, non-ideal heat transfer, liftoff, and kinetic energy from non-rigid body effects; therefore, this solution should be considered an upper bound on the jump height.

Computational results

The results of combining the discussions in the above sections can be found in Figure 5.2. Results are shown for when both the high modulus side is in contact with the hot plate (blue, Top Up) and when the low modulus side is in contact (orange, Top Down). Using the solution to the heat equation and the spontaneous strains from Figure 5.2B, we can calculate the effective spontaneous strains and curvatures as shown in Figures 5.2E,F, respectively. The spontaneous strains follow a similar deformation pathway; however, the spontaneous curvatures demonstrate a different behavior. When the high modulus side is placed on the hot plate, the curvature initially develops in one direction, then inverts as heat saturates the sheet.

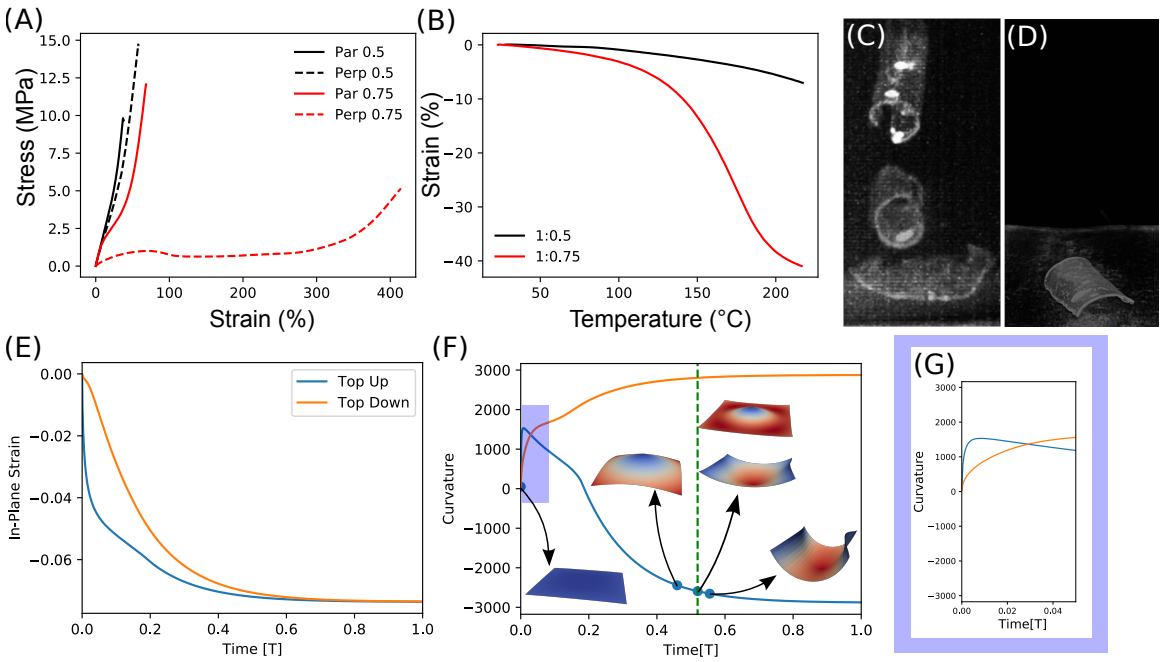

Figure 5.2: Material properties and thermomechanical response. (A) Stress-strain curves for uniaxially aligned LCEs measured parallel (solid lines) and perpendicular (dashed lines) to nematic director for high modulus (black) and low modulus (red) LCEs. Strain was applied at 5%/min. (B) Thermomechanical response of uniaxially aligned high (black) and low (red) modulus LCEs as LCE elements were held at a constant force of 0.0005 N and temperature was increased at 5°C/min. Overlaid sequence of images from high-speed recording of the response of the LCE laminates when the (C) high-modulus side or (D) low-modulus side was in contact with the hot surface. (E) Evolution of curvature in the simulated LCEs for the material parameters used in experiments in the cases the high modulus material is placed downward on the hot surface (blue) and when high modulus side is up (orange).

This behavior is not seen when the high modulus side is placed down, indicating that no snap-through will be seen. This behavior is confirmed in the experimental findings as the sheet only jumps when the high modulus side is placed down. We also calculate the quasi-static equilibrium configurations, as shown in the inset figures of Figure 5.2F, which demonstrate the initial transient behavior as well as the snap-through deformation.

5.5 Theory-led experimental examination of material and geometric variables

Equipped with a validated model, we consider other geometric variations of the system. One interesting adjustment is the association of the location of the point defect in the film geometry (Figure 5.3A). The model predicts that as the defect center

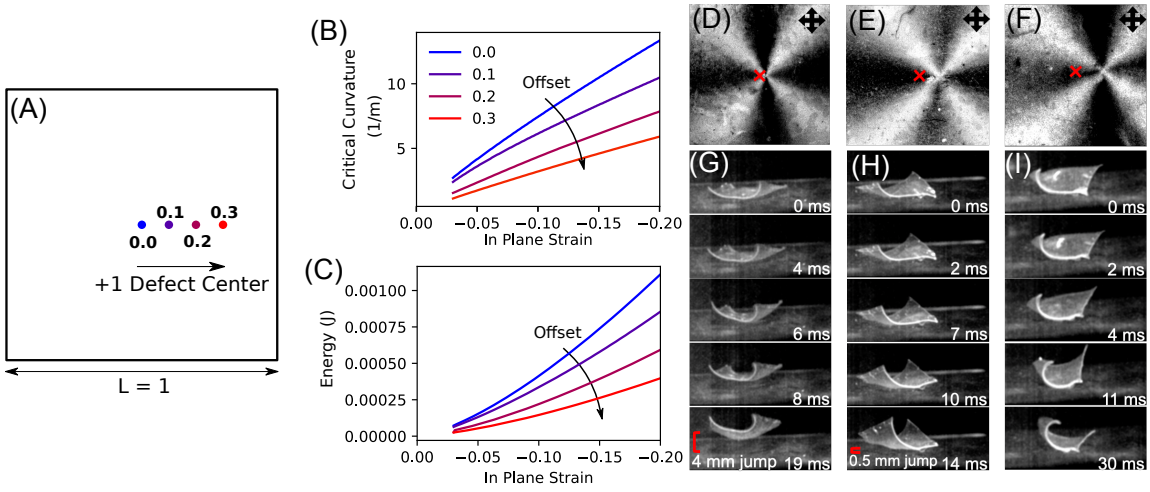

Figure 5.3: Spatial variation in patterning. (A) The central point of the topological defect was offset from the center of the square films. (B,C) Model predictions indicate that the critical curvature and energy released will decrease by offsetting the center point of the director profile relative to the geometric center of the film. The equivalent laminates were prepared experimentally, shown in (D,E,F) as viewed between crossed polarizers for 0.1 offset, 0.2 offset, and 0.3 offset, respectively. Materials were subjected to heat and high-speed images (G,H,I) were captured of the stimuli-response of the LCE patterns in (D-F), respectively.

is shifted away from the center of the laminate, the films will still undergo snap-through. However, as the defect is shifted further from the center of the laminate, the model predicted that the critical curvature required for snap-through would decrease (Figure 5.3B), resulting in less energy being dissipated in the snap-through event (Figure 5.3C). To test these results experimentally, we prepared LCE laminates as described in Figure 5.1D but in films where the point defect was offset from the center of the film (POM images in Figure 5.3D-F). The manufacturing and characterization procedure can be found in more detail in Appendix A.3. Upon actuating these materials, we find that the offset results in the snap-through deformation occurring at an angle, rather than the direct downward motion seen in the initial experiments. Therefore, the defect is shifted further from the center of the film, the amount of energy is not only decreased as predicted by the model, but also dissipated in ways that are not constructive to leaping. We see this manifest experimentally as leaping height decreases from 2 cm (0 offset, Figure 5.1), to 4 mm (0.1 offset, Figure 5.3G), to 1.5 mm (0.2 offset, Figure 5.3H), to no leaping (0.3 offset, Figure 5.3I), confirming that the optimal location of the defect center for maximum leaping height is, in fact, in the center of the material.

A second consideration is the preparation of LCE laminates with variation in the thickness. Evaluating this with our computational model, we find that increasing the thickness of the plate decreases the critical curvature for snap-through (Figure 5.4A), elucidating the trend that a thicker sheet penalizes the bending energy more than thin sheets. As a result, the sheet minimization of the bending energy causes the snap-through at smaller natural curvatures. The energy released in snap-through is not as straight-forward (Figure 5.4B). At small in-plane strains, a thinner sheet releases more energy than a thick sheet at snap-through. This is, in part, because the snap-through for thicker sheets happens at a reduced natural curvature. At some point, the energy of the thicker plates becomes higher. Consequently, one can control the energy release at snap-through by tailoring the in-plane strain and the thickness of the sheet. However, control of the physical response resulting from the snap-through is not trivial, as there will also be considerations such as energy dissipation in the various cases. Exploring the complication of effects relating to thickness and modulus grading experimentally, we fabricate LCEs with variation in the layering of the two material compositions. We see that by introducing more high modulus material to an LCE with equivalent overall thickness to the original laminates, leaping still occurs, but with significantly reduced height (Figure 5.4C). When total thickness is reduced and there is equivalent depth of high and low modulus material incorporated through the cross-section, we observe a slightly slower snap-through with no leaping (Figure 5.4D). When thickness is increased by adding an additional low modulus layer, we see rapid snap through followed by slow deformation to the final stable state (Figure 5.3E). These results confirm the complexity of the snap-through phenomenon in the LCEs relative to the material thickness and grading of modulus.

5.6 Directional LCE leaping

With fundamental understanding of the snap-through mechanism produced in these materials, we sought to introduce directional leaping to mimic the locomotion of organisms that utilize stored elastic energy. Taking a bio-inspired approach, we fabricated materials with “legs” that are longer on one edge of the material than the other (Figure 5.5A,B), giving the material a biased launching platform. The longer back legs offer a higher point of contact than the shorter back legs, causing the snap-through force to lift the material at an angle as depicted in Figure 5.5D. The angled snap-through resulted in leaping to the left as shown in Figure 5.5C, and gives the LCE the ability to jump a lateral distance of 10 mm as compared to

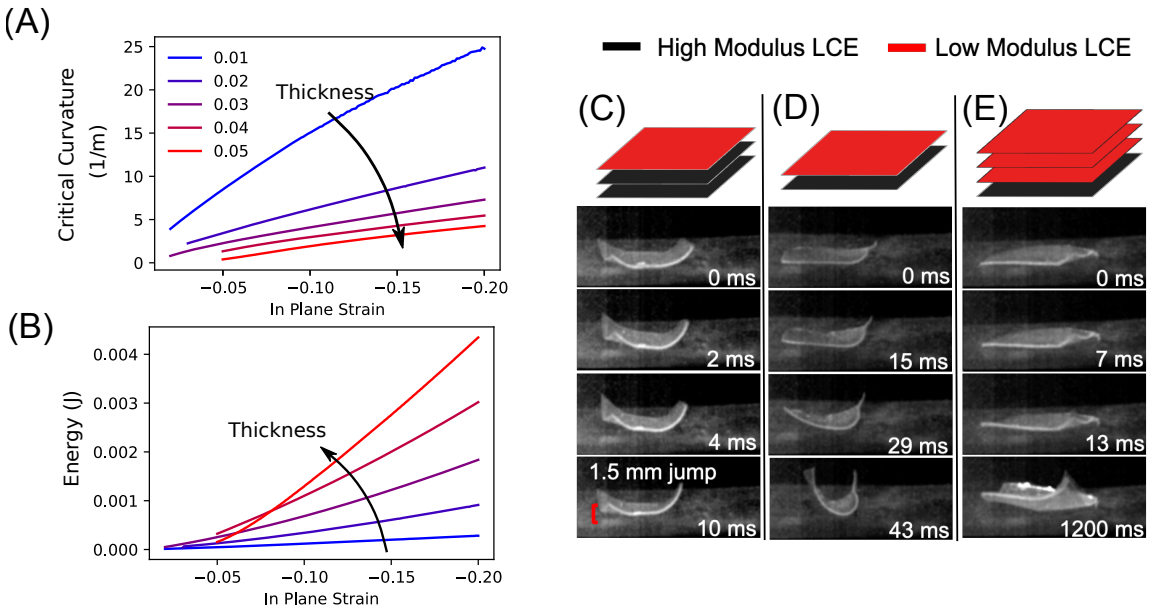

Figure 5.4: Through-thickness variation. (A) The critical curvature and (B) energy released in the snap-through event is predicted for LCE laminates with varying thickness-to-width as a function of in-plane strain. A schematic of each of three laminate variations and corresponding high-speed imagery of response is shown for variations of thickness and modulus gradient by combining (C) two high and one low modulus film, (D) one low modulus film and one high modulus film, and (E) three low modulus films and one high modulus film.

the original material that is confined to approximately 2 mm. We further explored the dependence of angle and leg length in relation to jumping ability and, much like defect offsets and layer variation, found that energy dissipation and curvature biases are extremely sensitive. If the legs are too long, the material favors initial deformation to the downward stable state, likely due to lack of surface contact on the edges to allow for upward curvature first (Figure 5.5F). If the angle is too steep, but surface contact is allowed, snap-through occurs but only leaves the surface on the side in contact (Figure 5.5G). Figure 5.5H shows a combination of moderate angle with long legs on one side, resulting in snap-through but immediate conversion to the second stable state with no leaping. Thus, we confirm that through careful balance of biased launch platform and the previously discussed material properties, bio-inspired directional leaping is feasible and effective.

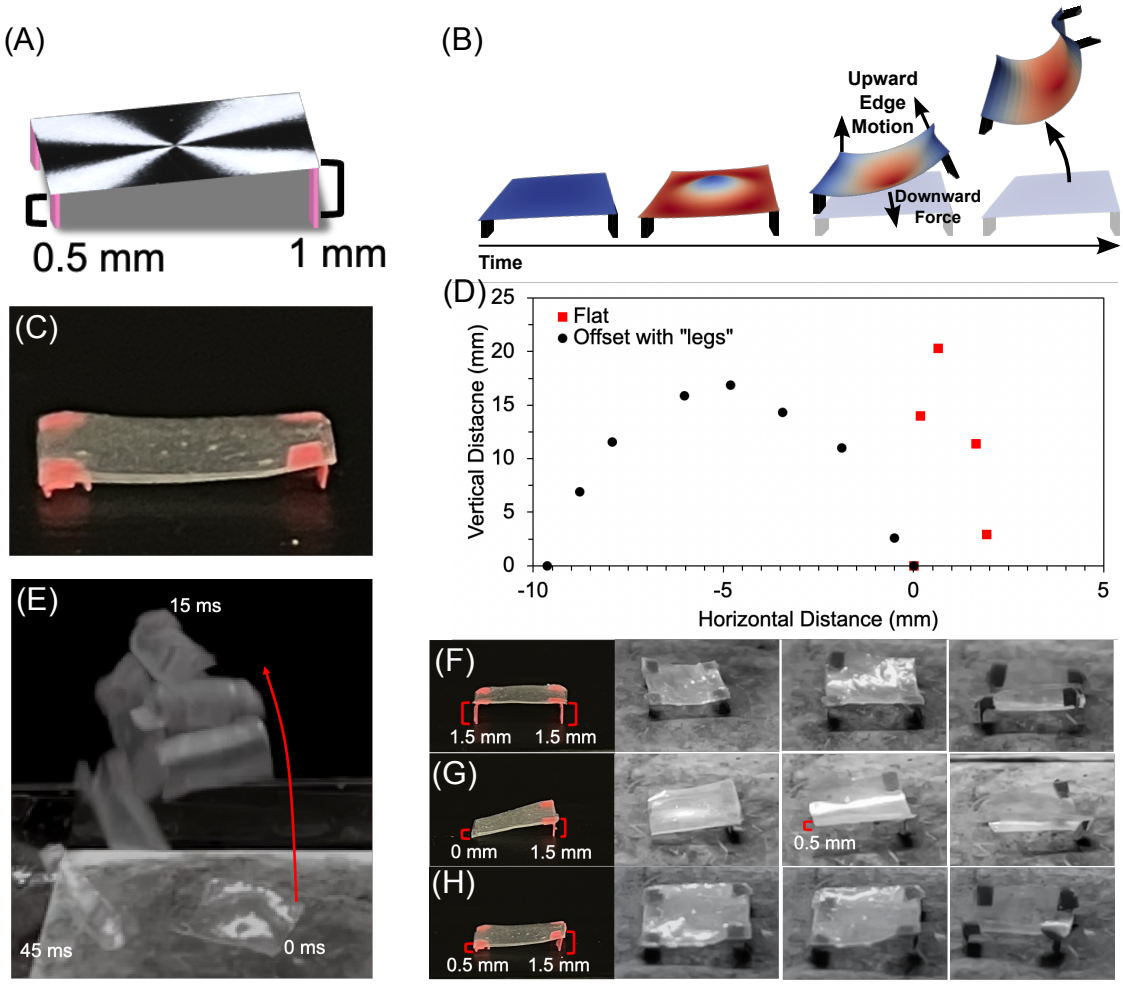

Figure 5.5: Leaping forward. (A) To facilitate directionality, the LCE laminate was prepared with legs. (B) When the legs are offset in length, the model predicts that the LCE laminate will directionally leap. (C) The LCE laminate was prepared with adhered legs. (D) The trajectory of the leaping of the LCE laminate with direct contact (red squares) is contrasted to that trajectory of the LCE laminate with legs (black circles). (E) Overlaid time-lapse images of the LCE with offset leaping direction upon exposure to heat. The lateral change was nearly 1 cm. (F,G,H) The leaping motion of the LCE laminates is dependent on the difference in leg height.

5.7 Conclusion

We have demonstrated the ability to generate leaping as a result of thermally-induced snap through in LCEs that is dependent upon a modulus discrepancy through the thickness of the material. We have shown simulation of the snap-through using theoretical considerations to elucidate strain and energy profiles associated with this behavior. Due to a delicate dissipation of energy upon snap through, the leaping phenomenon has been shown to be relatively restricted by the physical material parameters such as defect position and layer variations. If tuned properly, this behavior can be harnessed to achieve directional leaping and holds promise in bio-inspired applications, such as pumps, motors, and many other devices.

Additionally, the ability to design the cross sectional material properties to induce a two phase behavior is novel. This technique can be utilized as a method of breaking symmetry with dynamic materials in order to bias the deformation where bifurcations exist. This has tremendous application for thin sheets. One example is in origami, where fold patterns naturally induce two deformation modes. By patterning the material, particularly at the hinge location, we can bias each hinge individually to ensure the deformation follows the proper pathway to achieve the folded shape.

We discuss a methodology for modeling the deformations of Föppl-von Kármán plates using the augmented Lagrangian method. This allows us to naturally incorporate effects of higher order derivatives, allowing for solutions of non-linear curvature based systems. The methods developed are not specific to Föppl-von Kármán plates and can be generalized to solve for a large variety of systems that include second (or higher) derivatives in the energy.

Chapter 6

CONCLUSION AND FUTURE DIRECTIONS

6.1 Summary of findings

In this thesis, we present solutions to problems involving reduced dimensional structures. We particularly study beams, rods, ribbons, and sheets reacting to various forms of external stimuli. For many of these problems, we developed novel computational methods to find deformations and deformation pathways to lead to interesting behaviors with many potential applications in locomotion.

Photo-mechanical beams

In Chapter 3, we derive an equation that couples the illumination conditions of photo-mechanical thin films with the spontaneous curvature. We then study how the deformation of a beam develops over time considering large deformations and reorientation of the surface normal relative to the illumination. We demonstrated how illumination of a ring of photo-mechanical material can induce a continuous rolling behavior. We illustrate this through direct computation of the solution as well as a linear perturbation analysis with excellent agreement in the proper regimes. We additionally validate the flapping behavior of a double clamped beam as explored experimentally by [22]. Motivated by the snap-through of this doubly clamped configuration, we explore using directed beams of light to induce snap-through. We explore the configuration space of the system to determine under what conditions inversion occurs. Because of the energy barrior between the snapped configurations, the snapped configuration gets locked in. This system has potential to be used as a sensor due to the "memory" involved in the deformation.

Novel deformation measures for discrete elastic rods

In Chapter 4, we develop a novel method of discretizing rods with a direct relation to the continuous strain energy. Specifically, we define a set of deformation measures which directly correlate to the continuous rotation gradient. We then calculate the variations of the curvature measures as a series of sequential mappings. Due to the decoupling of the constitutive equations from the deformation measures, we can quickly and easily implement a large variety of different physical systems. We demonstrate consistency of the model with traditional buckling solutions, calculating

both the critical buckling loads and the post-buckled deformations. We then study more complicated 3D deformations including overcurved rings, pseudo-ribbons, and geometrically isometric Möbius strip. In each of these cases, we discuss the model and implementation, and compare to known solutions. The novelty of this work is in the development of the computational method which allows us to directly define discrete curvatures and calculate first and second variations for efficient computation.

Leaping liquid crystal elastomer films

In Chapter 5 we study the case of a laminate of liquid crystal elastomer sheets with drastically different material properties. When placed on a hot plate, the sheet would contract, form a conical shape, then rapidly invert, causing the sheet to jump off the plate. We identify the root cause of this behavior as the transient heat absorption through the thickness. The developing temperature profile interacts with the variation in spontaneous stretches through the thickness inducing a change in in-plane strain as well as curvature. As heat saturates the sheet, the curvature inverts and causes a snap-through behavior. In addition to the experiments, we study this system computationally by developing a method of calculating in-plane strain and curvature for highly anisotropic cross sections experiencing spontaneous stretches. We then calculate equilibrium configurations by utilizing an augmented Lagrangian approach to utilize traditional finite element formulations for use in mechanical systems involving second derivatives in the energy.

There are a few aspects of this work that introduce novel methods. First, we demonstrate a method of biasing the deformation of a sheet, which traditionally has multiple bifurcation modes, into a particular energy well by patterning the cross-sectional material properties. In particular, this deformation pathway does not need to be monotonic, as demonstrated by the sheet snapping through. This has many potential applications, particularly in the realm of actuating foldable structures. In addition, we utilize the augmented Lagrangian optimization structure in the context of sheet problems in order to study the effects of curvatures. We use this methodology to solve the Föppl-von Kármán plate equations; however, the formulation is generalizable to any problems involving second dervatives in the energy.

6.2 Future directions

This thesis presents various problems with reduced dimensional structures. As a result, this work invites many potential avenues for development.

The configurations studied in Chapter 3 are only a small subset of the potential configurations which are possible; therefore, there are many other configurations of beams which could allow for cyclic or continuous behaviors. In addition, the coupling of illumination with the evolution of spontaneous curvature is only valid in the small penetration regime. Many experimental systems demonstrate effects which are not captured by the model such as deep penetration or bleaching and need to be considered when developing an entire theory of photo-mechanical actuation.

With regards to the rod model developed in Chapter 4, a rigorous proof of convergence is necessary to mathematically prove the consistency with the continuous system, although there some work in that direction (for example see [96]). In addition, we mention that the model can be extended to extensible rods and ribbons. A careful treatment of this case must be considered, especially when studying viscoelastic rods with significant extension. Another avenue of exploration is in the behavior of rods under various forms of spontaneous curvatures. In particular, we could study the behavior shown in [25] where a flat ribbon deforms into a cylindrical shape and rolls under illumination. Because we developed the formulation for modeling such systems, there are many ways this can be applied to study and develop engineering systems.

Chapter 5 studies a configuration of LCE laminates that induces a snap-through instability. We only studied a few different types of laminates and configurations for material. Because of this, there are a large variety of different shapes and configurations that can be studied when implementing this effect. Additionally, we can study the effects that cuts in the domain can have in the snap-through.

We can open ourselves up to even more development if we look beyond the regime of flat sheets. In particular, one system of interest is in non-flat sheets, formally known as shells. Due to the development of techniques in 3D printing, we not only design the shape of a structure, but the liquid crystal alignment and material properties. A demonstration of this idea is shown in [97]. In this work, they 3D printed shells of liquid crystal elastomers that can be actuated upon heating. In most cases, the systems were cylindrically symmetric about a vertical axis. The direction of printing controls the direction of activation of the sponanous in-plane stretch and curvature. The shells are then placed into an oil bath. Heating the oil induces the

the nematic/isotropic transition, causing a change in spontaneous in-plane strain and curvature, causing a change in shape as a result.

Their experiments also demonstrate a snap-through deformation in a curled structure. As the curled structure deforms, its preferential state is a conical shape; however, the deformation pathway locks in a highly curled state. With sufficient spontaneous activation due to the the heating through oil, the highly curled configuration loses stability and snaps to the more conical configuration. Additionally, the snap-through itself presents some interesting properties. Both the configurations before and after the snap-through are symmetric; however, the system presents an asymmetric form between these two. This implies that, even though the initial and final configurations are symmetric, the bifurcation from one state to the next might not be. This invites the study of asymmetric bifurcation modes of symmetric bodies. This has important implications for actuation of symmetric bodies because it can significantly reduce the spontaneous strains at which bifurcations and snap-through occurs.

Ultimately, the models we have developed in this thesis improve our ability to model and study various configurations of dimensionally reduced systems such as beams, rods, ribbons, and sheets. By developing computationally efficient methods, we can rapidly study the design space, vastly reducing experimental costs and production times. This work opens up many avenues for studying these systems under complex loading conditions and spontaneous strains. By utilizing the non-linear characteristics of these systems, such as those demonstrated in this manuscript, many modes of motion and energy release can be realized for use in biological modeling, robotics, and actuation.

BIBLIOGRAPHY

[1] Basile Audoly and Yves Pomeau. “Elasticity and Geometry: From hair curls to the nonlinear response of shells”. In: (Dec. 2009), pp. 1–622.

[2] Raph Levien. “The elastica: a mathematical history”. In: 2008.

[3] Michael Sadowsky. “Die Differentialgleichungen des Möbiusschen Bandes”. In: *Jahresbericht der Deutschen Mathematiker-Vereinigung* 39 (2. Abt. Heft 5/8 Sept. 1929), pp. 49–51.

[4] W Wunderlich. “Über ein abwickelbares Möbiusband.” In: *Monatshefte für Mathematik* 66 (1962), pp. 276–289. URL: http://eudml.org/doc/177173.

[5] Marcelo A Dias et al. *Wunderlich, meet Kirchhoff; A general and unified description of elastic ribbons and thin rods*. 2014. URL: https://arxiv.org/pdf/1403.2094.pdf.

[6] Mark Warner and Eugene Terentjev. *Liquid Crystal Elastomers*. Vol. 120. Oct. 2003. ISBN: 9780198527671.

[7] Jürgen Küpfer and Heino Finkelmann. “Nematic liquid single crystal elastomers”. In: *Die Makromolekulare Chemie, Rapid Communications* 12 (12 Dec. 1991), pp. 717–726. ISSN: 0173-2803. DOI: 10.1002/MARC.1991.030121211. URL: https://onlinelibrary.wiley.com/doi/full/10.1002/marc.1991.030121211%20https://onlinelibrary.wiley.com/doi/abs/10.1002/marc.1991.030121211%20https://onlinelibrary.wiley.com/doi/10.1002/marc.1991.030121211.

[8] Jürgen Küpfer and Heino Finkelmann. “Liquid crystal elastomers: Influence of the orientational distribution of the crosslinks on the phase behaviour and reorientation processes”. In: *Macromolecular Chemistry and Physics* 195 (4 Apr. 1994), pp. 1353–1367. ISSN: 1521-3935. DOI: 10.1002/MACP.1994.021950419. URL: https://onlinelibrary.wiley.com/doi/full/10.1002/macp.1994.021950419%20https://onlinelibrary.wiley.com/doi/abs/10.1002/macp.1994.021950419%20https://onlinelibrary.wiley.com/doi/10.1002/macp.1994.021950419.

[9] Pierluigi Cesana, Paul Plucinsky, and Kaushik Bhattacharya. “Effective Behavior of Nematic Elastomer Membranes”. In: *Archive for Rational Mechanics and Analysis 2015 218:2* 218 (2 May 2015), pp. 863–905. ISSN: 1432-0673. DOI: 10.1007/S00205-015-0871-0. URL: https://link.springer.com/article/10.1007/s00205-015-0871-0.

[10] Yanlei Yu, Makoto Nakano, and Tomiki Ikeda. “Directed bending of a polymer film by light”. In: *Nature 2003 425:6954* 425 (6954 Sept. 2003), pp. 145–145.

ISSN: 1476-4687. DOI: 10.1038/425145a. URL: https://www.nature.com/articles/425145a.

[11] Miguel Camacho-Lopez et al. "Fast liquid-crystal elastomer swims into the dark". In: *Nature Materials* 3 (5 Apr. 2004), pp. 307–310. ISSN: 14761122. DOI: 10.1038/nmat1118. URL: www.nature.com/naturematerials.

[12] Timothy J. White and Dirk J. Broer. "Programmable and adaptive mechanics with liquid crystal polymer networks and elastomers". In: *Nature Materials 2015 14:11* 14 (11 Oct. 2015), pp. 1087–1098. ISSN: 1476-4660. DOI: 10.1038/nmat4433. URL: https://www.nature.com/articles/nmat4433.

[13] John David Crawford. "Introduction to bifurcation theory". In: *Reviews of Modern Physics* 63 (4 Oct. 1991), p. 991. ISSN: 00346861. DOI: 10.1103/RevModPhys.63.991. URL: https://journals.aps.org/rmp/abstract/10.1103/RevModPhys.63.991.

[14] Victoria Lee and Kaushik Bhattacharya. "Actuation of cylindrical nematic elastomer balloons". In: *Journal of Applied Physics* 129 (11 Mar. 2021), p. 114701. ISSN: 0021-8979. DOI: 10.1063/5.0041288. URL: https://aip.scitation.org/doi/abs/10.1063/5.0041288.

[15] Ellis Harold Dill. "Kirchhoff's Theory of Rods". In: *Archive for History of Exact Sciences* 44 (1 1992), pp. 1–23. ISSN: 00039519, 14320657. URL: http://www.jstor.org/stable/41133926.

[16] J. L. Zajac. "SOME INVESTIGATIONS OF PERCEPTION OF MOVEMENT AND RELATED DEPTH PHENOMENA". In: *British Journal of Psychology* 53 (2 May 1962), pp. 117–128. ISSN: 2044-8295. DOI: 10.1111/J.2044-8295.1962.TB00818.X. URL: https://onlinelibrary.wiley.com/doi/full/10.1111/j.2044-8295.1962.tb00818.x%20https://onlinelibrary.wiley.com/doi/abs/10.1111/j.2044-8295.1962.tb00818.x%20https://bpspsychub.onlinelibrary.wiley.com/doi/10.1111/j.2044-8295.1962.tb00818.x.

[17] W. R. Bauer, R. A. Lund, and J. H. White. "Twist and writhe of a DNA loop containing intrinsic bends". In: *Proceedings of the National Academy of Sciences of the United States of America* 90 (3 1993), pp. 833–837. ISSN: 00278424. DOI: 10.1073/PNAS.90.3.833. URL: https://www.pnas.org.

[18] T. McMillen and A. Goriely. "Tendril Perversion in Intrinsically Curved Rods". In: *Journal of Nonlinear Science 2002 12:3* 12 (3 May 2002), pp. 241–281. ISSN: 1432-1467. DOI: 10.1007/S00332-002-0493-1. URL: https://link.springer.com/article/10.1007/s00332-002-0493-1.

[19] Kevin Korner et al. "A nonlinear beam model of photomotile structures". In: *Proceedings of the National Academy of Sciences* (Apr. 2020). ISSN: 0027-8424. DOI: 10.1073/PNAS.1915374117. URL: https://www.pnas.org/content/early/2020/04/15/1915374117.

[20] Chen Tian et al. “Harnessing bistability for directional propulsion of soft, untethered robots”. In: *Proceedings of the National Academy of Sciences* 115 (22 May 2018). doi: 10.1073/pnas.1800386115, pp. 5698–5702. DOI: 10.1073/pnas.1800386115. URL: https://doi.org/10.1073/pnas.1800386115.

[21] T. (Timothy) White. *Photomechanical materials, composites, and systems : wireless transduction of light into work*. 2017. ISBN: 9781119123309. URL: https://www.wiley.com/en-us/Photomechanical+Materials%2C+Composites%2C+and+Systems%3A+Wireless+Transduction+of+Light+into+Work-p-9781119123309.

[22] Dirk Jan Mulder et al. “Making waves in a photoactive polymer film”. In: *Nature* 546 (7660 June 2017), pp. 632–636. ISSN: 0028-0836. DOI: 10.1038/nature22987. URL: http://www.nature.com/doifinder/10.1038/nature22987.

[23] Munenori Yamada et al. “Photomobile polymer materials: Towards light-driven plastic motors”. In: *Angewandte Chemie - International Edition* 47 (27 Mar. 2008). doi: 10.1002/anie.200800760, pp. 4986–4988. ISSN: 14337851. DOI: 10.1002/anie.200800760. URL: https://doi.org/10.1002/anie.200800760.

[24] Timothy J. White et al. “A high frequency photodriven polymer oscillator”. In: *Soft Matter* 4 (9 Aug. 2008), pp. 1796–1798. ISSN: 1744-6848. DOI: 10.1039/B805434G. URL: https://pubs.rsc.org/en/content/articlehtml/2008/sm/b805434g%20https://pubs.rsc.org/en/content/articlelanding/2008/sm/b805434g.

[25] Jeong Jae Wie, M. Ravi Shankar, and Timothy J. White. “Photomotility of polymers”. In: *Nature Communications* 7 (Nov. 2016), p. 13260. ISSN: 20411723. DOI: 10.1038/ncomms13260. URL: https://doi.org/10.1038/ncomms13260.

[26] D. Corbett and M. Warner. “Nonlinear photoresponse of disordered elastomers”. In: *Physical Review Letters* 96 (23 June 2006), p. 237802. ISSN: 00319007. DOI: 10.1103/PHYSREVLETT.96.237802/FIGURES/3/MEDIUM. URL: https://journals.aps.org/prl/abstract/10.1103/PhysRevLett.96.237802.

[27] Daniel Corbett, Chen Xuan, and Mark Warner. “Deep optical penetration dynamics in photobending”. In: *Physical Review E - Statistical, Nonlinear, and Soft Matter Physics* 92 (1 July 2015), p. 13206. ISSN: 15502376. DOI: 10.1103/PhysRevE.92.013206. URL: https://link.aps.org/doi/10.1103/PhysRevE.92.013206.

[28] Yin Lin, Lihua Jin, and Yongzhong Huo. “Quasi-soft opto-mechanical behavior of photochromic liquid crystal elastomer: Linearized stress-strain relations and finite element simulations”. In: *International Journal of Solids*

and Structures 49 (18 Sept. 2012), pp. 2668–2680. ISSN: 00207683. DOI: 10.1016/J.IJSOLSTR.2012.05.031.

[29] Matthew L. Smith et al. "Designing light responsive bistable arches for rapid, remotely triggered actuation". In: *Behavior and Mechanics of Multifunctional Materials and Composites 2014* 9058 (March 2014 2014), 90580F. DOI: 10.1117/12.2044906.

[30] M. R. Shankar et al. "Contactless, photoinitiated snap-through in azobenzene-functionalized polymers". In: *Proceedings of the National Academy of Sciences* 110 (47 Nov. 2013), pp. 18792–18797. ISSN: 0027-8424. DOI: 10.1073/pnas.1313195110. URL: http://www.ncbi.nlm.nih.gov/pubmed/24190994%20http://www.pubmedcentral.nih.gov/articlerender.fcgi?artid=PMC3839691%20http://www.pnas.org/cgi/doi/10.1073/pnas.1313195110.

[31] Amir Alipour Skandani et al. "Discrete-state photomechanical actuators". In: *Extreme Mechanics Letters* 9 (2016), pp. 45–54. ISSN: 23524316. DOI: 10.1016/j.eml.2016.05.002. URL: http://dx.doi.org/10.1016/j.eml.2016.05.002.

[32] Kevin Korner, Basile Audoly, and Kaushik Bhattacharya. "Simple deformation measures for discrete elastic rods and ribbons". In: *Proceedings of the Royal Society A* 27 (Dec. 2021), pp. 1–63. ISSN: 1364-5021. DOI: 10.1098/RSPA.2021.0561. URL: https://royalsocietypublishing.org/doi/abs/10.1098/rspa.2021.0561.

[33] Changyeob Baek and Pedro M. Reis. "Rigidity of hemispherical elastic gridshells under point load indentation". In: *Journal of the Mechanics and Physics of Solids* 124 (Mar. 2019), pp. 411–426. ISSN: 0022-5096. DOI: 10.1016/J.JMPS.2018.11.002.

[34] Julian Panetta et al. "X-Shells: a new class of deployable beam structures". In: *ACM Transactions on Graphics (TOG)* 38 (4 July 2019). ISSN: 15577368. DOI: 10.1145/3306346.3323040. URL: https://dl.acm.org/doi/abs/10.1145/3306346.3323040.

[35] Stuart Antman. *Nonlinear Problems of Elasticity*. 2nd ed. Springer-Verlag, 2005. DOI: 10.1007/0-387-27649-1.

[36] P. T. Brun, N. M. Ribe, and B. Audoly. "A numerical investigation of the fluid mechanical sewing machine". In: *Physics of Fluids* 24 (4 Apr. 2012), p. 043102. ISSN: 1070-6631. DOI: 10.1063/1.3703316. URL: https://aip.scitation.org/doi/abs/10.1063/1.3703316.

[37] Neil M. Ribe, Mehdi Habibi, and Daniel Bonn. "Liquid Rope Coiling". In: *http://dx.doi.org/10.1146/annurev-fluid-120710-101244* 44 (Dec. 2011), pp. 249–266. ISSN: 00664189. DOI: 10.1146/ANNUREV-FLUID-120710-101244. URL: https://www.annualreviews.org/doi/abs/10.1146/annurev-fluid-120710-101244.

[38] Bernard D. Coleman and Daniel C. Newman. “On the rheology of cold drawing. I. Elastic materials”. In: *Journal of Polymer Science Part B: Polymer Physics* 26 (9 1988), pp. 1801–1822. ISSN: 10990488. DOI: 10.1002/POLB.1988.090260901.

[39] Basile Audoly and John W. Hutchinson. “Analysis of necking based on a one-dimensional model”. In: *Journal of the Mechanics and Physics of Solids* 97 (Dec. 2016), pp. 68–91. ISSN: 0022-5096. DOI: 10.1016/J.JMPS.2015.12.018.

[40] Basile Audoly and John W. Hutchinson. “One-dimensional modeling of necking in rate-dependent materials”. In: *Journal of the Mechanics and Physics of Solids* 123 (Feb. 2019), pp. 149–171. ISSN: 00225096. DOI: 10.1016/J.JMPS.2018.08.005.

[41] Claire Lestringant and Basile Audoly. “A one-dimensional model for elastocapillary necking”. In: *Proceedings of the Royal Society A* 476 (2240 Aug. 2020), p. 20200337. ISSN: 1364-5021. DOI: 10.1098/RSPA.2020.0337. URL: https://royalsocietypublishing.org/doi/abs/10.1098/rspa.2020.0337.

[42] Claire Lestringant, Basile Audoly, and Dennis M. Kochmann. “A discrete, geometrically exact method for simulating nonlinear, elastic and inelastic beams”. In: *Computer Methods in Applied Mechanics and Engineering* 361 (Apr. 2020), p. 112741. ISSN: 0045-7825. DOI: 10.1016/J.CMA.2019.112741.

[43] E. L. Starostin and G. H.M. Van Der Heijden. “The shape of a Möbius strip”. In: *Nature Materials 2007 6:8* 6 (8 July 2007), pp. 563–567. ISSN: 1476-4660. DOI: 10.1038/nmat1929. URL: https://www.nature.com/articles/nmat1929.

[44] E. L. Starostin and G. H.M. van der Heijden. “Equilibrium Shapes with Stress Localisation for Inextensible Elastic Möbius and Other Strips”. In: *Journal of Elasticity* 119 (1-2 Apr. 2015), pp. 67–112. ISSN: 15732681. DOI: 10.1007/S10659-014-9495-0/FIGURES/28. URL: https://link.springer.com/article/10.1007/s10659-014-9495-0.

[45] Basile Audoly and Sébastien Neukirch. “A one-dimensional model for elastic ribbons: A little stretching makes a big difference”. In: *Journal of the Mechanics and Physics of Solids* 153 (Aug. 2021), p. 104457. ISSN: 0022-5096. DOI: 10.1016/J.JMPS.2021.104457.

[46] Miklós Bergou et al. “Discrete elastic rods”. In: 2008, pp. 1–12. DOI: 10.1145/1508044.1508058. URL: http://portal.acm.org/citation.cfm?doid=1508044.1508058.

[47] D. J. Steigmann and M. G. Faulkner. “Variational theory for spatial rods”. In: *Journal of Elasticity 1993 33:1* 33 (1 Oct. 1993), pp. 1–26. ISSN: 1573-

2681. DOI: 10.1007/BF00042633. URL: https://link.springer.com/article/10.1007/BF00042633.

[48] Florence Bertails et al. "Super-helices for predicting the dynamics of natural hair". In: *ACM Transactions on Graphics (TOG)* 25 (3 July 2006), pp. 1180–1187. ISSN: 07300301. DOI: 10.1145/1141911.1142012. URL: https://dl.acm.org/doi/abs/10.1145/1141911.1142012.

[49] Romain Casati and Florence Bertails-Descoubes. "Super space clothoids". In: *ACM Transactions on Graphics (TOG)* 32 (4 July 2013). ISSN: 07300301. DOI: 10.1145/2461912.2461962. URL: https://dl.acm.org/doi/abs/10.1145/2461912.2461962.

[50] Raphaël Charrondière et al. "Numerical modeling of inextensible elastic ribbons with curvature-based elements". In: *Computer Methods in Applied Mechanics and Engineering* 364 (June 2020), p. 112922. ISSN: 0045-7825. DOI: 10.1016/J.CMA.2020.112922.

[51] M. Khalid Jawed, Alyssa Novelia, and Oliver M. O'Reilly. "A Primer on the Kinematics of Discrete Elastic Rods". In: (2018). DOI: 10.1007/978-3-319-76965-3. URL: http://link.springer.com/10.1007/978-3-319-76965-3.

[52] M. Gazzola et al. "Forward and inverse problems in the mechanics of soft filaments". In: *Royal Society Open Science* 5 (6 June 2018). ISSN: 20545703. DOI: 10.1098/RSOS.171628. URL: https://royalsocietypublishing.org/doi/full/10.1098/rsos.171628.

[53] João Pedro Morais, Svetlin Georgiev, and Wolfgang Sprößig. "Real quaternionic calculus handbook". In: *Real Quaternionic Calculus Handbook* (Jan. 2014), pp. 1–216. DOI: 10.1007/978-3-0348-0622-0.

[54] Joachim Linn. "Discrete Cosserat Rod Kinematics Constructed on the Basis of the Difference Geometry of Framed Curves—Part I: Discrete Cosserat Curves on a Staggered Grid". In: *Journal of Elasticity 2019 139:2* 139 (2 July 2019), pp. 177–236. ISSN: 1573-2681. DOI: 10.1007/S10659-019-09744-W. URL: https://link.springer.com/article/10.1007/s10659-019-09744-w.

[55] Miklós Bergou et al. "Discrete viscous threads". In: *ACM SIGGRAPH 2010 Papers, SIGGRAPH 2010* (July 2010). ISSN: 07300301. DOI: 10.1145/1778765.1778853.

[56] B. Audoly et al. "A discrete geometric approach for simulating the dynamics of thin viscous threads". In: *Journal of Computational Physics* 253 (Nov. 2013), pp. 18–49. ISSN: 0021-9991. DOI: 10.1016/J.JCP.2013.06.034.

[57] Jorge Nocedal and Stephen J. Wright. *Numerical Optimization*. Springer New York, 2006. DOI: 10.1007/978-0-387-40065-5.

[58] Gaël Guennebaud, Benoît Jacob, et al. *Eigen v3*. 2010.

[59] Jinhye Bae et al. “Edge-defined metric buckling of temperature-responsive hydrogel ribbons and rings”. In: *Polymer* 55 (23 Nov. 2014), pp. 5908–5914. ISSN: 0032-3861. DOI: 10.1016/J.POLYMER.2014.08.033.

[60] Lorenzo Freddi et al. “A Corrected Sadowsky Functional for Inextensible Elastic Ribbons”. In: *Journal of Elasticity 2015 123:2* 123 (2 Oct. 2015), pp. 125–136. ISSN: 1573-2681. DOI: 10.1007/S10659-015-9551-4. URL: https://link.springer.com/article/10.1007/s10659-015-9551-4.

[61] Roberto Paroni and Giuseppe Tomassetti. “Macroscopic and Microscopic Behavior of Narrow Elastic Ribbons”. In: *Journal of Elasticity 2018 135:1* 135 (1 Dec. 2018), pp. 409–433. ISSN: 1573-2681. DOI: 10.1007/S10659-018-09712-W. URL: https://link.springer.com/article/10.1007/s10659-018-09712-w.

[62] Eusebius J. Doedel et al. “AUTO-07P: Continuation and bifurcation software for ordinary differential equations”. In: (2007). URL: http://citeseerx.ist.psu.edu/viewdoc/summary?doi=10.1.1.423.2590.

[63] E. L. Starostin and G. H.M. Van Der Heijden. “Force and moment balance equations for geometric variational problems on curves”. In: *Physical Review E* 79 (6 June 2009), p. 066602. ISSN: 15393755. DOI: 10.1103/PhysRevE.79.066602. URL: https://journals.aps.org/pre/abstract/10.1103/PhysRevE.79.066602.

[64] Pierre Olivier Mouthuy et al. “Overcurvature describes the buckling and folding of rings from curved origami to foldable tents”. In: *Nature Communications 2012 3:1* 3 (1 Dec. 2012), pp. 1–8. ISSN: 2041-1723. DOI: 10.1038/ncomms2311. URL: https://www.nature.com/articles/ncomms2311.

[65] Basile Audoly and Keith A. Seffen. “Buckling of Naturally Curved Elastic Strips: The Ribbon Model Makes a Difference”. In: *Journal of Elasticity 2015 119:1* 119 (1 Mar. 2015), pp. 293–320. ISSN: 1573-2681. DOI: 10.1007/S10659-015-9520-Y. URL: https://link.springer.com/article/10.1007/s10659-015-9520-y.

[66] Ansel Ugural and Saul Fenster. *Advanced Mechanics of Materials and Applied Elasticity*. 6th ed. 2020. URL: https://www.pearson.com/us/higher-education/program/Ugural-Advanced-Mechanics-of-Materials-and-Applied-Elasticity-6th-Edition/PGM1937691.html.

[67] Tomohiko G. Sano and Hirofumi Wada. “Twist-Induced Snapping in a Bent Elastic Rod and Ribbon”. In: *Physical Review Letters* 122 (11 Mar. 2019), p. 114301. ISSN: 10797114. DOI: 10.1103/PhysRevLett.122.114301.

[68] T. Yu and J. A. Hanna. “Bifurcations of buckled, clamped anisotropic rods and thin bands under lateral end translations”. In: *Journal of the Mechanics and Physics of Solids* 122 (Jan. 2019), pp. 657–685. ISSN: 0022-5096. DOI: 10.1016/J.JMPS.2018.01.015.

[69] Michael Gomez, Derek E. Moulton, and Dominic Vella. "Dynamics of viscoelastic snap-through". In: *Journal of the Mechanics and Physics of Solids* 124 (Mar. 2019), pp. 781–813. ISSN: 0022-5096. DOI: 10.1016/J.JMPS.2018.11.020.

[70] Marina Pilz da Cunha et al. "A Soft Transporter Robot Fueled by Light". In: *Advanced Science* 7 (5 Mar. 2020), p. 1902842. ISSN: 2198-3844. DOI: 10.1002/ADVS.201902842. URL: https://onlinelibrary.wiley.com/doi/full/10.1002/advs.201902842%20https://onlinelibrary.wiley.com/doi/abs/10.1002/advs.201902842%20https://onlinelibrary.wiley.com/doi/10.1002/advs.201902842.

[71] Shoue Chen et al. "Soft Crawling Robots: Design, Actuation, and Locomotion". In: *Advanced Materials Technologies* 5 (2 Feb. 2020), p. 1900837. ISSN: 2365-709X. DOI: 10.1002/ADMT.201900837. URL: https://onlinelibrary.wiley.com/doi/full/10.1002/admt.201900837%20https://onlinelibrary.wiley.com/doi/abs/10.1002/admt.201900837%20https://onlinelibrary.wiley.com/doi/10.1002/admt.201900837.

[72] Zhongsheng Liu et al. "Somatosensitive film soft crawling robots driven by artificial muscle for load carrying and multi-terrain locomotion". In: *Materials Horizons* 8 (6 June 2021), pp. 1783–1794. ISSN: 2051-6355. DOI: 10.1039/D1MH00457C. URL: https://pubs.rsc.org/en/content/articlehtml/2021/mh/d1mh00457c%20https://pubs.rsc.org/en/content/articlelanding/2021/mh/d1mh00457c.

[73] Silvan Gantenbein et al. "Three-dimensional printing of hierarchical liquid-crystal-polymer structures". In: *Nature 2018 561:7722* 561 (7722 Sept. 2018), pp. 226–230. ISSN: 1476-4687. DOI: 10.1038/s41586-018-0474-7. URL: https://www.nature.com/articles/s41586-018-0474-7.

[74] M. Pilz Da Cunha, M. G. Debije, and A. P.H.J. Schenning. "Bioinspired light-driven soft robots based on liquid crystal polymers". In: *Chemical Society Reviews* 49 (18 Sept. 2020), pp. 6568–6578. ISSN: 1460-4744. DOI: 10.1039/D0CS00363H. URL: https://pubs.rsc.org/en/content/articlehtml/2020/cs/d0cs00363h%20https://pubs.rsc.org/en/content/articlelanding/2020/cs/d0cs00363h.

[75] Elizabeth Queathem. "The ontogeny of grasshopper jumping performance". In: *Journal of Insect Physiology* 37 (2 Jan. 1991), pp. 129–138. ISSN: 0022-1910. DOI: 10.1016/0022-1910(91)90098-K.

[76] Henry C. Astley and Thomas J. Roberts. "Evidence for a vertebrate catapult: elastic energy storage in the plantaris tendon during frog jumping". In: *Biology Letters* 8 (3 June 2012), pp. 386–389. ISSN: 1744957X. DOI: 10.1098/RSBL.2011.0982. URL: https://royalsocietypublishing.org/doi/full/10.1098/rsbl.2011.0982.

[77] Henry C. Astley and Thomas J. Roberts. "The mechanics of elastic loading and recoil in anuran jumping". In: *Journal of Experimental Biology* 217 (24 Dec. 2014), pp. 4372–4378. ISSN: 14779145. DOI: 10.1242/JEB.110296/VIDEO-1. URL: https://journals.biologists.com/jeb/article/217/24/4372/12983/The-mechanics-of-elastic-loading-and-recoil-in.

[78] M. Janneke Schwaner, David C. Lin, and Craig P. McGowan. "Jumping mechanics of desert kangaroo rats". In: *Journal of Experimental Biology* 221 (22 Nov. 2018). ISSN: 00220949. DOI: 10.1242/JEB.186700/20745. URL: https://journals.biologists.com/jeb/article/221/22/jeb186700/20745/Jumping-mechanics-of-desert-kangaroo-rats.

[79] Yongjin Kim, Jay van den Berg, and Alfred J. Crosby. "Autonomous snapping and jumping polymer gels". In: *Nature Materials 2021 20:12* 20 (12 Feb. 2021), pp. 1695–1701. ISSN: 1476-4660. DOI: 10.1038/s41563-020-00909-w. URL: https://www.nature.com/articles/s41563-020-00909-w.

[80] Jisoo Jeon et al. "Continuous and programmable photomechanical jumping of polymer monoliths". In: *Materials Today* 49 (Oct. 2021), pp. 97–106. ISSN: 1369-7021. DOI: 10.1016/J.MATTOD.2021.04.014.

[81] Hiroki Arazoe et al. "An autonomous actuator driven by fluctuations in ambient humidity". In: *Nature Materials 2016 15:10* 15 (10 July 2016), pp. 1084–1089. ISSN: 1476-4660. DOI: 10.1038/nmat4693. URL: https://www.nature.com/articles/nmat4693.

[82] Benjamin Gorissen et al. "Inflatable soft jumper inspired by shell snapping". In: *Science Robotics* 5 (42 May 2020). ISSN: 24709476. DOI: 10.1126/SCIROBOTICS.ABB1967/SUPPL_FILE/ABB1967_SM.PDF. URL: https://www.science.org/doi/abs/10.1126/scirobotics.abb1967.

[83] Grietje N. Mol et al. "Thermo-Mechanical Responses of Liquid-Crystal Networks with a Splayed Molecular Organization". In: *Advanced Functional Materials* 15 (7 July 2005), pp. 1155–1159. ISSN: 1616-3028. DOI: 10.1002/ADFM.200400503. URL: https://onlinelibrary.wiley.com/doi/full/10.1002/adfm.200400503%20https://onlinelibrary.wiley.com/doi/abs/10.1002/adfm.200400503%20https://onlinelibrary.wiley.com/doi/10.1002/adfm.200400503.

[84] Kazuko Fuchi et al. "Topology optimization for the design of folding liquid crystal elastomer actuators". In: *Soft Matter* 11 (37 Sept. 2015), pp. 7288–7295. ISSN: 1744-6848. DOI: 10.1039/C5SM01671A. URL: https://pubs.rsc.org/en/content/articlehtml/2015/sm/c5sm01671a%20https://pubs.rsc.org/en/content/articlelanding/2015/sm/c5sm01671a.

[85] B. A. Kowalski et al. “Curvature by design and on demand in liquid crystal elastomers”. In: *Physical Review E* 97 (1 Jan. 2018), p. 012504. ISSN: 24700053. DOI: 10.1103/PHYSREVE.97.012504/FIGURES/5/MEDIUM. URL: https://journals.aps.org/pre/abstract/10.1103/PhysRevE.97.012504.

[86] Tyler Guin et al. “Layered liquid crystal elastomer actuators”. In: *Nature Communications 2018 9:1* 9 (1 June 2018), pp. 1–7. ISSN: 2041-1723. DOI: 10.1038/s41467-018-04911-4. URL: https://www.nature.com/articles/s41467-018-04911-4.

[87] Marina Pilz da Cunha et al. “Liquid Crystal Soft Robot: An Untethered Magnetic- and Light-Responsive Rotary Gripper: Shedding Light on Photoresponsive Liquid Crystal Actuators (Advanced Optical Materials 7/2019)”. In: *Advanced Optical Materials* 7 (7 Apr. 2019), p. 1970025. ISSN: 2195-1071. DOI: 10.1002/ADOM.201970025. URL: https://onlinelibrary.wiley.com/doi/full/10.1002/adom.201970025%20https://onlinelibrary.wiley.com/doi/abs/10.1002/adom.201970025%20https://onlinelibrary.wiley.com/doi/10.1002/adom.201970025.

[88] “Liquid Crystal Elastomers: Materials and Applications”. In: 250 (2012). Ed. by Wim H. de Jeu. DOI: 10.1007/978-3-642-31582-4. URL: http://link.springer.com/10.1007/978-3-642-31582-4.

[89] Taylor H. Ware et al. “Voxelated liquid crystal elastomers”. In: *Science* 347 (6225 Feb. 2015), pp. 982–984. ISSN: 10959203. DOI: 10.1126/SCIENCE.1261019/SUPPL_FILE/WARE-SM.PDF. URL: https://www.science.org/doi/abs/10.1126/science.1261019.

[90] Suk Kyun Ahn et al. “Photoinduced Topographical Feature Development in Blueprinted Azobenzene-Functionalized Liquid Crystalline Elastomers”. In: *Advanced Functional Materials* 26 (32 Aug. 2016), pp. 5819–5826. ISSN: 1616-3028. DOI: 10.1002/ADFM.201601090. URL: https://onlinelibrary.wiley.com/doi/full/10.1002/adfm.201601090%20https://onlinelibrary.wiley.com/doi/abs/10.1002/adfm.201601090%20https://onlinelibrary.wiley.com/doi/10.1002/adfm.201601090.

[91] Mark Warner. “Topographic Mechanics and Applications of Liquid Crystalline Solids”. In: *https://doi.org/10.1146/annurev-conmatphys-031119-050738* 11 (Mar. 2020), pp. 125–145. ISSN: 19475462. DOI: 10.1146/ANNUREV-CONMATPHYS-031119-050738. URL: https://www.annualreviews.org/doi/abs/10.1146/annurev-conmatphys-031119-050738.

[92] J. N. (Junuthula Narasimha) Reddy. *Mechanics of laminated composite plates and shells : theory and analysis*. CRC Press, 2004, p. 831. ISBN: 9780849315923. URL: https://www.routledge.com/Mechanics-of-Laminated-Composite-Plates-and-Shells-Theory-and-Analysis/Reddy/p/book/9780849315923.

[93] Charles Augarde. “Generation of shape functions for rectangular plate elements”. In: *Communications in Numerical Methods in Engineering* 20 (Aug. 2004). DOI: 10.1002/cnm.703.

[94] Olgierd Cecil Zienkiewicz and Robert Leroy Taylor. *The finite element method: solid mechanics*. Vol. 2. Butterworth-heinemann, 2000. ISBN: 0750650559.

[95] Daniel Arndt et al. “The deal.II Library, Version 9.3”. In: *Journal of Numerical Mathematics* 29 (3 2021), pp. 171–186. DOI: 10.1515/jnma-2021-0081. URL: https://dealii.org/deal93-preprint.pdf.

[96] Sebastian Scholtes, Henrik Schumacher, and Max Wardetzky. “Variational convergence of discrete elasticae”. In: *IMA Journal of Numerical Analysis* 42 (1 Jan. 2022), pp. 300–332. ISSN: 0272-4979. DOI: 10.1093/IMANUM/DRAA084. URL: https://academic.oup.com/imajna/article/42/1/300/6041855.

[97] Cedric P. Ambulo et al. “Four-dimensional Printing of Liquid Crystal Elastomers”. In: *ACS Applied Materials and Interfaces* 9 (42 Oct. 2017), pp. 37332–37339. DOI: 10.1021/ACSAMI.7B11851. URL: https://pubs.acs.org/doi/abs/10.1021/acsami.7b11851.

[98] Jernej Barbič and Yili Zhao. “Real-time Large-deformation Substructuring”. In: *ACM Trans. on Graphics (SIGGRAPH 2011)* 30 (4 2011), 91:1–91:7.

[99] Tayler S. Hebner et al. “Polymer Network Structure, Properties, and Formation of Liquid Crystalline Elastomers Prepared via Thiol-Acrylate Chain Transfer Reactions”. In: *Macromolecules* 54 (23 Dec. 2021), pp. 11074–11082. ISSN: 15205835. DOI: 10.1021/ACS.MACROMOL.1C01919/SUPPL_FILE/MA1C01919_SI_001.PDF. URL: https://pubs.acs.org/doi/abs/10.1021/acs.macromol.1c01919.

Appendix A

SUPPLEMENTARY MATERIAL

A.1 Supplement for Chapter 3

Computational Model

The numerical method is motivated by the discrete elastic rod model[1]. We partition the beam into $N-1$ segments $\mathcal{S}^i = (S_i, S_{i+1})$, $i = 1, \ldots, N-1$ which are all equal in arc-length by introducing N nodes: the ith node is at arc-length $S_i = (i-1)L/(N-1)$. We introduce the angle θ^i, $i = 1, \ldots, N-1$ to be the angle that the segment $\mathcal{S}^i$ makes to the horizontal as our main kinematic variable. We can then obtain the current position of the nth node by exploiting the inextensibility condition as follows:

$$\mathbf{x}_n = \mathbf{x}_1 + \sum_{i=2}^{n} (S_i - S_{i-1}) \left(\cos\theta^{i-1}\mathbf{e}_1 + \sin\theta^{i-1}\mathbf{e}_2 \right).$$

The curvature is carried at the nodes and defined as $\kappa_i = \theta^i - \theta^{i-1}$ so that the total bending energy of the beam (discrete equivalent to (3.15)) is given by

$$E_B[\theta] = \sum_{i=2}^{N-1} \frac{1}{2} J_i (\theta^i - \theta^{i-1} - \kappa_i^0)^2, \tag{A.1}$$

where J_i is a bending modulus and κ_i^0 is the discrete natural curvature at the ith node.

We obtain the equilibrium equation (discrete equivalent to (3.12)) by taking the variation of E_B with respect to θ^j:

$$\frac{\partial E_B}{\partial \theta^j} = J_j(\theta^j - \theta^{j-1} - \kappa_j^0) - J_{j+1}(\theta^{j+1} - \theta^j - \kappa_{j+1}^0) = 0. \tag{A.2}$$

Given the spontaneous curvatures $\{\kappa_j^0\}$, we solve these equations for $\{\theta^j\}$ subject to appropriate boundary conditions. In order to improve the stability and convergence, it is convenient to have the Hessian,

$$\frac{\partial^2 E_B}{\partial \theta^j \partial \theta^k} = -J_j \delta_k^j + (J_j + J_{j+1})\delta_k^j - J_{j+1}\delta_k^{j+1}.$$

[1] Miklós Bergou, Max Wardetzky, Stephen Robinson, Basile Audoly, and Eitan Grinspun. Discrete elastic rods. ACM Transactions on Graphics, 27(3):63:1 – 63:12, August 2008.

It remains to specify the spontaneous curvature. This evolves according to (3.13) whose discrete version is given by the set of ordinary differential equations:

$$\frac{\mathrm{d}\kappa_i^0}{\mathrm{d}t} + \kappa_i^0 = \Lambda f(\theta_i - \theta_I), \tag{A.3}$$

where $f(\theta_i - \theta_I)$ is as defined in Equation 3.13 and $\theta_i = (ave)(\theta^i, \theta^{i-1})$ is defined as the angle of the tangent of the ith node.

Equation (A.3) is discretized in time using an explicit Newton time stepping algorithm. Time dependent solutions are obtained by alternating the elastic relaxation in equation (A.2) and evolving of natural curvatures κ_i^0 based on equation (A.3) over a time step.

Elastic Ring

In Section 3.3, we analyzed rolling rings. They can be simulated by adapting the general numerical procedure outlined above as follows. The closure of the ring is imposed by the following constraints:

$$\theta^1 = 0 \qquad \mathbf{x}_1 = \mathbf{x}_{N-1} \qquad \mathbf{x}_2 = \mathbf{x}_N\,,$$

The first of these can be implemented explicitly by freezing that degree of freedom and represents that the point of contact is tangent to the surface.

The last two enforce the closure constraint. The system is initialized by assuming a constant curvature which makes the last two nodes coincident with the first two. Then the system is relaxed by minimizing the energy while imposing the constraints. In order to stabilize the point of contact when the system is circular, a small amount of gravity is initially added and removed once the natural curvature deviates from its initial state.

The algorithm for calculating the translation and rotation of the system is as follows. Initially, the point of contact is defined to be the first and second nodes (second to last and last due to constraints). Then, given a natural curvature, κ_j^0, the energy is minimized to find the new configuration. The natural curvature is then updated using the explicit forward Euler scheme according to (A.3). Then, using a small window near the first and second nodes (which wraps around to nodes on the far end of the beam), the closest node to the calculated center of mass is found. Then, the nodes on either side of that node are tested to find the closest to the center of mass. This then forms an ordered pair of nodes $(\mathbf{x}_i, \mathbf{x}_{i+1})$ which defines the segment

closest to the center of mass. Then, by shifting the minimized curvature $\theta^i \rightarrow \theta^1$, $\theta^{i+1} \rightarrow \theta^2$, etc in a cyclic manner (so the quantities at end points get wrapped around the beam). Similar transformations are done to the natural curvature ($\kappa_i^0 \rightarrow \kappa_{N-1}^0$, $\kappa_{i+1}^0 \rightarrow \kappa_2^0$). Note that these transformations are done in such a way that the ordering of the nodes is preserved and wrapped. At this point, the updated points of contact are now the 1st and 2nd nodes and the algorithm can be repeated to integrate the system in time. This solves for the rotation of the system while the translation can be found by using the rolling contact condition. Using the convention before, we had set $\mathbf{x}_1 = \mathbf{0}$. We can set this to be the relative position where the true position of node i is defined as $\tilde{\mathbf{x}}_i = \mathbf{x}_{S_c} + \mathbf{x}_i$ where $\mathbf{x}_{S_c}$ is the position of the point of contact. $\mathbf{x}_{S_c}$ is found using the rolling condition. Let $\mathbf{x}_{S_c}^k$ be the position of the point of contact at time step k and i be the shift necessary to establish that the point of contact is vertically aligned with the center of mass. Then,

$$\mathbf{x}_{S_c}^{k+1} = \begin{cases} \mathbf{x}_{S_c}^k + (S_i - S_1)\mathbf{E}_1 & \text{if } i \in [1, Ns] \\ \mathbf{x}_{S_c}^k + (S_i - S_{N-1})\mathbf{E}_1 & \text{if } i \in [N - Ns, N - 1] \end{cases},$$

where N_s is a small window (usually set to $N/20$). If i is not in the range of values defined above, then the time discretization is made finer in order to ensure that the rotations induced in each time step correlate with a small translation. The results for various angles of incidence of light and intensities are given in Movie S1 in the supplementary material. The "velocity" of the system is then found by finding the distance the point of contact travels over a small time window. Steady state velocities are found by iterating the time stepping procedure until the velocity reaches a steady value.

Doubly Clamped Beam

The doubly clamped system can be solved by setting up the following constraints:

$$\theta^1 = 0 \qquad \theta^{N-1} = 0 \qquad \mathbf{x}_N = l_f \mathbf{e}_1 \,,$$

where $l_f < L$ is the distance between the two endpoints. As before, the first of these two constraints can be implemented explicitly by freezing those degrees of freedom and requires no special treatment, while the latter two constraints need to be implemented in the optimization engine. The initial solution is obtained numerically by decreasing l_f from 1 to its actual value in small steps. The system is integrated in time by alternating between relaxing the elastic energy and updating

the natural curvature using an explicit Newton time stepping method. The results for various angles of incidence of light and intensities are given in Movie S2 in the supplementary material.

Equilibrium and Stability Analysis

Investigation of the snapping instabilities from Section 3.4 requires obtaining the second variation of the energy $\mathcal{E}(\theta)$ in the presence of m constraints $c_i(\theta) = 0$, $i = 1, 2, ..., m$, where $\theta \in \mathbb{R}^n$ is the set of degrees of freedom. Denote the feasible set $C = \{\theta \in \mathbb{R}^n \text{ s.t. } c_i(\theta) = 0\}$. We are interested in solutions $\bar{\theta} \in C \subset \mathbb{R}^n$ such that

$$\mathcal{E}\left(\bar{\theta} + \varepsilon u + \frac{1}{2}\varepsilon^2 w\right) \geq \mathcal{E}(\bar{\theta}), \quad \forall u, w \in \mathbb{R}^n,$$

satisfying $\bar{\theta} + \varepsilon u + \frac{1}{2}\varepsilon^2 w \in C$, with $\varepsilon \to 0$. Expanding each of these out to first order and simplifying gives,

$$\nabla\mathcal{E}(\bar{\theta}) \cdot u = 0,$$

$$\nabla c_i(\bar{\theta}) \cdot u = 0,$$

where ∇ denotes the gradient operator relative to the degrees of freedom of the function ($(\nabla E)_i = \frac{\partial E}{\partial \theta_i}$). This gives the equilibrium condition,

$$\nabla\mathcal{E}(\bar{\theta}) + \sum_{i=1}^{m} \lambda_i \nabla c_i(\bar{\theta}) = 0,$$

where the parameters λ_i are Lagrange multipliers.

For stability, we require that any perturbation which satisfies the constraints will increase the energy. To do this, we expand our system to second order in ε and simplify:

$$u \cdot \nabla^2\mathcal{E}(\bar{\theta})u + \nabla\mathcal{E}(\bar{\theta}) \cdot w \geq 0,$$

$$u \cdot \nabla^2 c_i(\bar{\theta})u + \nabla c_i(\bar{\theta}) \cdot w = 0,$$

where ∇^2 is the Hessian operator which returns the symmetric matrix of second derivatives. Using the equilibrium condition, we have

$$\nabla\mathcal{E}(\bar{\theta}) \cdot w = -\sum_{i=1}^{m} \lambda_i \nabla c_i(\bar{\theta}) \cdot w = u \cdot \sum_{i=1}^{m} \lambda_i \nabla^2 c_i(\bar{\theta}) u.$$

Plugging this into the above inequality, we have the stability condition that

$$u \cdot \left(\nabla^2\mathcal{E}(\bar{\theta}) + \sum_{i=1}^{m} \lambda_i \nabla^2 c_i(\bar{\theta})\right) u \geq 0,$$

for all u such that

$$\nabla c_i(\bar{\theta}) \cdot u = 0\,.$$

To determine whether a configuration satisfies this condition, we want to project $\mathbb{R}^n$ onto the space tangent to the constraints. This is done by a Gram-Schmidt process where

$$v_1 = \frac{\nabla c_1(\bar{\theta})}{\|\nabla c_1(\bar{\theta})\|}\,,$$

$$v_k = \frac{\nabla c_k(\bar{\theta}) - \sum_{i=1}^{k-1}(\nabla c_k(\bar{\theta}) \cdot v_i)v_i}{\|\nabla c_k(\bar{\theta}) - \sum_{i=1}^{k-1}(\nabla c_k(\bar{\theta}) \cdot v_i)v_i\|}\,,$$

$$P = I - \sum_{i=1}^{m} v_i \otimes v_i\,.$$

The stability analysis then boils down to calculating the eigenvalues of

$$P\left(\nabla^2 \mathcal{E}(\bar{\theta}) + \sum_{i=1}^{m} \lambda_i \nabla^2 c_i(\bar{\theta})\right) P\,.$$

Due to the projection, there will be m zero eigenvalues and stability is implied when all other eigenvalues are greater than zero. This analysis determines if there exists feasible paths which locally lowers the energy; therefore, the existence of a non-positive eigenvalue implies a loss of stability of the configuration.

Experimental Methods

Materials The monomers 1,4-Bis[4-(6-acryloyloxyhexyloxy)benzoyloxy]-2-methylbenzene (RM82) and 4,4'-Bis(6-acryloyloxyhexyloxy)azobenzene (Azo-6) were purchased from Synthon Chemicals and the photoinitiator phenylbis(2,4,6-trimethylbenzoyl)phosphine oxide) (Irgacure 819) was purchased from Sigma Aldrich. All chemicals were used as received. The polyimide alignment layer Elvamide was donated by Dupont.

Synthesis of LCN Beams Planar nematic LCN films were prepared following the procedure of Gelebart et al. (1) with modification. To synthesize films with the a penetration depth at 365 nm of 1.5 m, a formulation of 9.2 : 90.8 by weight of Azo-6 : RM82 was used, with 2.5 wt% of photoinitiator with respect to the total monomer weight. In a typical sample preparation, 4.6 mg Azo-6, 45.4 mg RM82, and 1.25 mg Irgacure 819 were melted together in a vial and vortexed repeatedly to ensure mixing. The molten monomer mixture was then infiltrated via capillary action into alignment cells on a hot plate at 100°C. The alignment cells were prepared by spin-coating

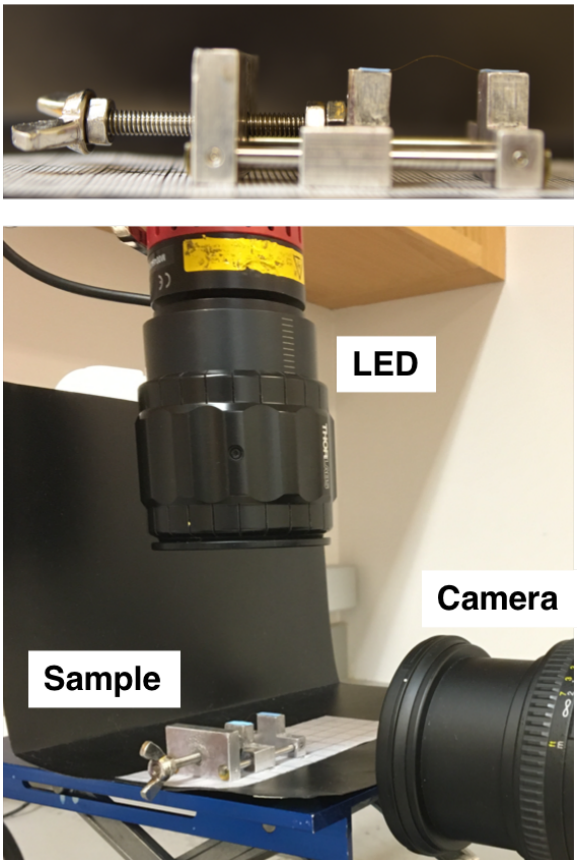

Figure A.1: (Top) The sample is fixed at the ends in a home-made compression device. (Bottom) Experimental set-up is composed of a beam illuminated overhead by a UV LED and imaged from the side by a camera.

Elvamide onto clean glass slides, rubbing the slides with a velvet cloth, and gluing the two Elvamide sides facing each other with epoxy mixed with 15 m glass beads. The filled cells were subsequently cooled to 80°C, held isothermal for 5 minutes to induce alignment of the liquid crystalline mesogens, and photopolymerized for 30 minutes with 405 nm light. Following photopolymerization, samples were post-cured at 120°C for 10 minutes and the 15m thick LCNs were harvested by cracking open the alignment cells with a razor blade. Finally, beams of 1 mm in width were cut from the film with the nematic director along the long axis of the strip.

Photoactuation Experiments Buckled beams with dimensions 1 mm x 15 mm x 50 m were prepared by clamping the ends of the film in a home-made film clamp device and compressed to an end-to-end distance of Lfinal/Linitial = 0.95. The buckled film was subsequently illuminated from above with a 365 nm LED (Thor-Labs) equipped with a Guassian profile focused onto the sample via an adjustable

focusing lens. Each experiment is recorded using a camera (Nikon 5500) fitted with a macrolens operating at a recording speed of 60 frames per second.

A.2 Supplement for Chapter 4

Plot of function ψ

The function $\psi(t)$ from equation (4.18) is plotted in figure A.2.

Detailed derivation of the strain gradients

In this appendix, we provide a detailed derivation of the first and second gradients of the strain appearing in section 4.3.

To derive the first gradient, we continue to use the conventions of section 4.3: we use a perturbation $\delta \boldsymbol{X}$ of the degrees of freedom, and we denote by $\delta \boldsymbol{y} = \boldsymbol{f}'(\boldsymbol{x}) \cdot \delta \boldsymbol{x}$ the first variation of a generic quantity $\boldsymbol{y} = \boldsymbol{f}(\boldsymbol{x})$ entering in the reconstruction of the discrete strain, where $\boldsymbol{x}$ depends indirectly on the degrees of freedom $\boldsymbol{X}$.

For the second variation, however, we work here in a slightly more general setting than in the main text, as we consider two *independent* perturbations $\delta_1 \boldsymbol{X}$ and $\delta_2 \boldsymbol{X}$ of the degrees of freedom. We denote by $\delta_1 \boldsymbol{x}$ and $\delta_2 \boldsymbol{x}$ the corresponding perturbations to the variable $\boldsymbol{x}$, and by $\delta_1 \boldsymbol{y}$ and $\delta_2 \boldsymbol{y}$ the first-order variations of the functions: $\delta_1 \boldsymbol{y} = \boldsymbol{f}'(\boldsymbol{x}) \cdot \delta_1 \boldsymbol{x}$ and $\delta_2 \boldsymbol{y} = \boldsymbol{f}'(\boldsymbol{x}) \cdot \delta_2 \boldsymbol{x}$ are simply obtained by replacing the generic increment $\delta \boldsymbol{x}$ appearing in the first order variation $\delta \boldsymbol{y}$ with $\delta_1 \boldsymbol{x}$ and $\delta_2 \boldsymbol{x}$, respectively. To obtain the second variation, we perturb the argument $\boldsymbol{x}$ appearing in $\delta_1 \boldsymbol{y} = \boldsymbol{f}'(\boldsymbol{x}) \cdot \delta_1 \boldsymbol{x}$ as $\boldsymbol{x} + \delta_2 \boldsymbol{x}$, leaving $\delta_1 \boldsymbol{x}$ untouched, and we expand the result to first order in $\delta_2 \boldsymbol{x}$. This yields a quantity denoted as $\delta_{12} \boldsymbol{y}$, which we can write formally as $\delta_{12} \boldsymbol{y} = \boldsymbol{f}''(\boldsymbol{x}) : (\delta_1 \boldsymbol{x} \otimes \delta_2 \boldsymbol{x})$, where $\boldsymbol{f}''(\boldsymbol{x})$ is the Hessian. By a classical result in the calculus of variations, the quantity $\delta_{12} \boldsymbol{y}$ is bilinear and symmetric with respect

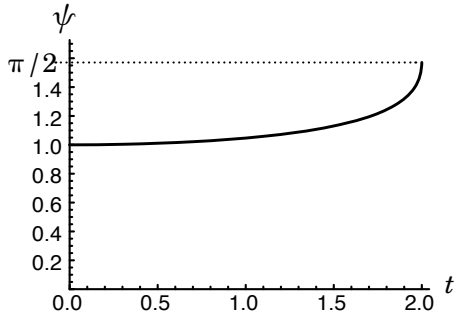

Figure A.2: Function $\psi(t)$ from equation (4.18) used to adjust the norm of the strain $\boldsymbol{\kappa}_i$ with $t = |\boldsymbol{\kappa}_i|$, see equation (4.19).

to $\delta_1 \boldsymbol{x}$ and $\delta_2 \boldsymbol{x}$. The second variation $\delta^2 \boldsymbol{y}$ given in the main text is the quadratic form obtained by ultimately condensing the variations $\delta_1 \boldsymbol{x}$ and $\delta_2 \boldsymbol{x}$ appearing in $\delta_{12} \boldsymbol{y}$ into a single perturbation $\delta \boldsymbol{x} = \delta_1 \boldsymbol{x} = \delta_2 \boldsymbol{x}$.

Infinitesimal rotation vectors

As an important preliminary result, we show that the first variation of a rotation represented by a unit quaternion s can be characterized by means of first-order *vector-valued* increment $\delta\hat{\boldsymbol{s}} \in \mathbb{R}^3$, and that the second variation of s can be represented by means of a second-order *vector-valued* increment $\delta_{12}\hat{\boldsymbol{s}} \in \mathbb{R}^3$. These vectors will be referred as the *infinitesimal rotation vectors*. They are connected to the variations δs and $\delta_{12} s$ of the quaternion by

$$\begin{aligned} \delta s &= \tfrac{1}{2}\, \delta\hat{\boldsymbol{s}}\, s \\ \delta_{12} s &= \left(\tfrac{1}{2}\, \delta_{12}\hat{\boldsymbol{s}} - \tfrac{1}{4}\, \delta_1\hat{\boldsymbol{s}} \cdot \delta_2\hat{\boldsymbol{s}} \right) s. \end{aligned} \tag{A.4}$$

The increment $\delta\hat{\boldsymbol{s}}$ is linear with respect to the variation $\delta \boldsymbol{X}$ of the degrees of freedom, and the increment $\delta_{12}\hat{\boldsymbol{s}}$ is bilinear with respect to the independent variations $\delta_1 \boldsymbol{X}$ and $\delta_2 \boldsymbol{X}$ of the degrees of freedom. As usual in our notation, $\delta_1\hat{\boldsymbol{s}}$ and $\delta_2\hat{\boldsymbol{s}}$ denote the first-order variation $\delta\hat{\boldsymbol{s}}$, evaluated on the increment $\delta_1 \boldsymbol{X}$ and $\delta_2 \boldsymbol{X}$, respectively. This representation of the first and second variations of a parameterized quaternion is equivalent to that proposed by [98].

The proof is as follows. By taking the first variation of the condition $2\ (s\,\overline{s} - 1) = 0$ that s is a unit quaternion, we have $0 = 2\,\delta s\,\overline{s} + 2\,s\,\overline{\delta s} = 2\,\delta s\,\overline{s} + \overline{2\,\delta s\,\overline{s}}$. This shows that the quaternion $2\,\delta s\,\overline{s}$ is a pure vector: this the vector $\delta\hat{\boldsymbol{s}}$ introduced in equation (A.4) above. Now, by inserting the increment $\delta_1 \boldsymbol{X}$ in the relation just derived, we have $2\,\delta_1 s\,\overline{s} \in \mathbb{R}^3$; perturbing this expression as $s \leftarrow s + \delta_2 s$, one shows that the following quaternion is a pure vector: $2\,\delta_{12} s\,\overline{s} + 2\,\delta_1 s\,\overline{\delta_2 s} = 2\,\delta_{12} s\,\overline{s} + \frac{1}{2}\ (\delta_1\hat{\boldsymbol{s}}\, s)\ \overline{(\delta_2\hat{\boldsymbol{s}}\, s)} = 2\,\delta_{12} s\,\overline{s} - \frac{1}{2}\,\delta_1\hat{\boldsymbol{s}}\,\delta_2\hat{\boldsymbol{s}} = 2\,\delta_{12} s\,\overline{s} + \frac{1}{2}\,\delta_1\hat{\boldsymbol{s}} \cdot \delta_2\hat{\boldsymbol{s}} - \frac{1}{2}\,\delta_1\hat{\boldsymbol{s}} \times \delta_2\hat{\boldsymbol{s}}$; here, the quaternion product $\delta_1\hat{\boldsymbol{s}}\,\delta_2\hat{\boldsymbol{s}}$ has been evaluated using the definition (4.4). Adding the vector quantity $\frac{1}{2}\,\delta_1\hat{\boldsymbol{s}} \times \delta_2\hat{\boldsymbol{s}}$, the quantity $2\,\delta_{12} s\,\overline{s} + \frac{1}{2}\,\delta_1\hat{\boldsymbol{s}} \cdot \delta_2\hat{\boldsymbol{s}}$ appears to be another pure vector: this is the vector $\delta_{12}\hat{\boldsymbol{s}}$ introduced in equation (A.4).

The second-order infinitesimal rotation vector $\delta_{12}\hat{\boldsymbol{s}}$ can be calculated directly from the first-order one $\delta\hat{\boldsymbol{s}}$ as

$$\delta_{12}\hat{\boldsymbol{s}} = \frac{\delta_1(\delta_2\hat{\boldsymbol{s}}) + \delta_2(\delta_1\hat{\boldsymbol{s}})}{2}. \tag{A.5}$$

Here, $\delta_1(\delta_2\hat{\boldsymbol{s}})$ denotes the first-order variation of $\delta_2\hat{\boldsymbol{s}}$ when s is perturbed into $s + \delta_1 s$; this quantity is *not* symmetric with respect to the perturbations $\delta_1 s$ and $\delta_2 s$.

Similarly, $\delta_2(\delta_1\hat{\boldsymbol{s}})$ denotes the first-order variation of $\delta_1\hat{\boldsymbol{s}}$ when s is perturbed into $s + \delta_2 s$.

The proof of equation (A.5) is as follows. Take the second variation of $\delta_1 s = \frac{1}{2}\,\delta_1\hat{\boldsymbol{s}}\; s$ from equation (A.4) as

$$\delta_{12}s = \frac{1}{2}\,\delta_2(\delta_1\hat{\boldsymbol{s}})\; s + \frac{1}{4}\,\delta_1\hat{\boldsymbol{s}}\;\delta_2\hat{\boldsymbol{s}}\; s = \left(\frac{1}{2}\,\delta_2(\delta_1\hat{\boldsymbol{s}}) - \frac{1}{4}\,\delta_1\hat{\boldsymbol{s}}\cdot\delta_2\hat{\boldsymbol{s}} + \frac{1}{4}\,\delta_1\hat{\boldsymbol{s}}\times\delta_2\hat{\boldsymbol{s}}\right) s\,.$$

The left-hand side is symmetric with respect to the perturbations $\delta_1 s$ and $\delta_2 s$, by definition of the second variation. Symmetrizing the right-hand side, we obtain $\delta_{12}s = \left(\frac{\delta_1(\delta_2\hat{\boldsymbol{s}})+\delta_2(\delta_1\hat{\boldsymbol{s}})}{4} - \frac{\delta_1\hat{\boldsymbol{s}}\cdot\delta_2\hat{\boldsymbol{s}}}{4}\right) s$. The infinitesimal rotation vector $\delta_{12}\hat{\boldsymbol{s}}$ can then be identified from equation (A.4), which yields the result stated in equation (A.5).

In the following sections, the first and second variations of the rotations that enter into the Discrete elastic rod model, such as the parallel transport p^i and the director rotation d^i, will be systematically represented using the corresponding infinitesimal rotation vectors, such as $\delta\hat{\boldsymbol{p}}^i$, $\delta_{12}\hat{\boldsymbol{p}}^i$, $\delta\hat{\boldsymbol{d}}^i$, and $\delta_{12}\hat{\boldsymbol{d}}^i$.

Variation of parallel transport

We start by deriving the variations of the parallel transport $p_{\boldsymbol{a}}^{\boldsymbol{b}}$ from the unit vector $\boldsymbol{a}$ to the unit vector $\boldsymbol{b}$ defined in equation (4.6), assuming $\boldsymbol{b} \neq -\boldsymbol{a}$. As $\boldsymbol{a}$ represents the fixed unit tangent $\boldsymbol{T}^i$ in reference configuration, it remains unperturbed,

$$\delta\boldsymbol{a} = \boldsymbol{0} \qquad \delta_{12}\boldsymbol{a} = \boldsymbol{0}.$$

Since $\boldsymbol{b}$ remains a unit vector during the perturbation, we have $\frac{1}{2}\,(|\boldsymbol{b}|^2 - 1) = 0$. Taking the first and second variation of this constraint, we have

$$\boldsymbol{b}\cdot\delta\boldsymbol{b} = 0 \qquad \boldsymbol{b}\cdot\delta_{12}\boldsymbol{b} + \delta_1\boldsymbol{b}\cdot\delta_2\boldsymbol{b} = \boldsymbol{0}.$$

First variation of parallel transport

As a preliminary step, we consider the case of parallel transport from $\boldsymbol{b}$ to its perturbation $\boldsymbol{b} + \delta\boldsymbol{b}$. Using $\boldsymbol{b}\cdot\delta\boldsymbol{b} = 0$, we find from equation (4.6),

$$p_{\boldsymbol{b}}^{\boldsymbol{b}+\delta\boldsymbol{b}} = 1 + \frac{\boldsymbol{b}\times\delta\boldsymbol{b}}{2} + O(|\delta\boldsymbol{b}|^2).$$

We now return to the calculation of $p_{\boldsymbol{a}}^{\boldsymbol{b}+\delta\boldsymbol{b}}$. Following the work of [46], as well as equations [3.7] and [A.2] from [42], one can use a holonomy reasoning to shows that, to first order in $\delta\boldsymbol{b}$,

$$p_{\boldsymbol{a}}^{\boldsymbol{b}+\delta\boldsymbol{b}} = p_{\boldsymbol{b}}^{\boldsymbol{b}+\delta\boldsymbol{b}}\; p_{\boldsymbol{a}}^{\boldsymbol{b}}\, r_{\boldsymbol{a}}\left(-\frac{\boldsymbol{a}\times\boldsymbol{b}}{1+\boldsymbol{a}\cdot\boldsymbol{b}}\cdot\delta\boldsymbol{b}\right) + O(|\delta\boldsymbol{b}|^2).$$

We rewrite this as

$$p_{\boldsymbol{a}}^{\boldsymbol{b}+\delta\boldsymbol{b}} = p_{\boldsymbol{b}}^{\boldsymbol{b}+\delta\boldsymbol{b}}\, p_{\boldsymbol{a}}^{\boldsymbol{b}}\, r_{\boldsymbol{a}}(\delta\theta) + O(|\delta\boldsymbol{b}|^2), \tag{A.6}$$

where $\delta\theta = -\frac{\boldsymbol{k}}{2}\cdot\delta\boldsymbol{b}$ and $\boldsymbol{k}$ is the scaled binormal that characterizes the holonomy (see [46]),

$$\boldsymbol{k} = \frac{2\,\boldsymbol{a}\times\boldsymbol{b}}{1+\boldsymbol{a}\cdot\boldsymbol{b}}. \tag{A.7}$$

The infinitesimal rotation $r_{\boldsymbol{a}}(\delta\theta)$ from equation (A.6) can be found from equation (4.5) as

$$\begin{aligned} r_{\boldsymbol{a}}(\delta\theta) &= 1 + \boldsymbol{a}\,\tfrac{\delta\theta}{2} + O(\delta\theta^2) \\ &= 1 - \tfrac{\boldsymbol{k}\cdot\delta\boldsymbol{b}}{4}\,\boldsymbol{a} + O(\delta\theta^2) \\ &= 1 - \tfrac{\boldsymbol{a}\otimes\boldsymbol{k}}{4}\cdot\delta\boldsymbol{b} + O(\delta\theta^2). \end{aligned} \tag{A.8}$$

Equation (A.6) is then rewritten with the help of the operator $\boldsymbol{b}_\times$ from equation (4.24) as

$$\begin{aligned} p_{\boldsymbol{a}}^{\boldsymbol{b}+\delta\boldsymbol{b}} &= \left(1 + \tfrac{\boldsymbol{b}_\times}{2}\cdot\delta\boldsymbol{b}\right)\, p_{\boldsymbol{a}}^{\boldsymbol{b}}\, \left(1 - \tfrac{\boldsymbol{a}\otimes\boldsymbol{k}}{4}\cdot\delta\boldsymbol{b}\right) + O(|\delta\boldsymbol{b}|^2) \\ &= \left(1 + \tfrac{\boldsymbol{b}_\times}{2}\cdot\delta\boldsymbol{b} - \tfrac{(p_{\boldsymbol{a}}^{\boldsymbol{b}}*\boldsymbol{a})\otimes\boldsymbol{k}}{4}\cdot\delta\boldsymbol{b}\right)\, p_{\boldsymbol{a}}^{\boldsymbol{b}} + O(|\delta\boldsymbol{b}|^2) \\ &= \left(1 + \tfrac{2\,\boldsymbol{b}_\times - \boldsymbol{b}\otimes\boldsymbol{k}}{4}\cdot\delta\boldsymbol{b}\right)\, p_{\boldsymbol{a}}^{\boldsymbol{b}} + O(|\delta\boldsymbol{b}|^2). \end{aligned}$$

In view of this, the first order variation of parallel transport writes as

$$\delta p_{\boldsymbol{a}}^{\boldsymbol{b}} = \frac{1}{2}\left(\left(\boldsymbol{b}_\times - \frac{\boldsymbol{b}\otimes\boldsymbol{k}}{2}\right)\cdot\delta\boldsymbol{b}\right)\, p_{\boldsymbol{a}}^{\boldsymbol{b}}.$$

Identifying with equation (A.4), we find that it is captured by the infinitesimal rotation vector

$$\delta\hat{\boldsymbol{p}}_{\boldsymbol{a}}^{\boldsymbol{b}} = \left(\boldsymbol{b}_\times - \frac{\boldsymbol{b}\otimes\boldsymbol{k}}{2}\right)\cdot\delta\boldsymbol{b}. \tag{A.9}$$

Second variation of parallel transport

From equation (A.9), we have

$$\begin{aligned} \delta_2(\delta_1\hat{\boldsymbol{p}}_{\boldsymbol{a}}^{\boldsymbol{b}}) &= \left((\delta_2\boldsymbol{b})_\times - \tfrac{\delta_2\boldsymbol{b}\otimes\boldsymbol{k}+\boldsymbol{b}\otimes\delta_2\boldsymbol{k}}{2}\right)\cdot\delta_1\boldsymbol{b} + \left(\boldsymbol{b}_\times - \tfrac{\boldsymbol{b}\otimes\boldsymbol{k}}{2}\right)\cdot\delta_{12}\boldsymbol{b} \\ &= \delta_2\boldsymbol{b}\times\delta_1\boldsymbol{b} - \tfrac{1}{2}\delta_2\boldsymbol{b}\,(\boldsymbol{k}\cdot\delta_1\boldsymbol{b}) - \tfrac{\boldsymbol{b}}{2}\,\delta_2\boldsymbol{k}\cdot\delta_1\boldsymbol{b} + \left(\boldsymbol{b}_\times - \tfrac{\boldsymbol{b}\otimes\boldsymbol{k}}{2}\right)\cdot\delta_{12}\boldsymbol{b}\,. \end{aligned} \tag{A.10}$$

Using equation (A.7), the variation of the binormal is found as

$$\begin{aligned} \delta_2\boldsymbol{k} &= \tfrac{2\,\boldsymbol{a}\times\delta_2\boldsymbol{b}}{1+\boldsymbol{a}\cdot\boldsymbol{b}} - \tfrac{2\,\boldsymbol{a}\times\boldsymbol{b}}{(1+\boldsymbol{a}\cdot\boldsymbol{b})^2}\,\boldsymbol{a}\cdot\delta_2\boldsymbol{b} \\ &= \tfrac{2}{1+\boldsymbol{a}\cdot\boldsymbol{b}}\,\left(\boldsymbol{a}\times\delta_2\boldsymbol{b} - \tfrac{\boldsymbol{k}}{2}(\boldsymbol{a}\cdot\delta_2\boldsymbol{b})\right) \\ &= \tfrac{2}{1+\boldsymbol{a}\cdot\boldsymbol{b}}\,\left(\boldsymbol{a}_\times - \tfrac{\boldsymbol{k}\otimes\boldsymbol{a}}{2}\right)\cdot\delta_2\boldsymbol{b}\,. \end{aligned}$$

Inserting into equation (A.10) and reordering the terms, we find

$$\begin{aligned}\delta_2(\delta_1\hat{\boldsymbol{p}}_a^{\boldsymbol{b}}) =&\delta_2\boldsymbol{b}\times\delta_1\boldsymbol{b}+\left(\boldsymbol{b}_\times-\frac{\boldsymbol{b}\otimes\boldsymbol{k}}{2}\right)\cdot\delta_{12}\boldsymbol{b}\\&-\frac{\boldsymbol{b}}{(1+\boldsymbol{a}\cdot\boldsymbol{b})}\left(\delta_1\boldsymbol{b}\cdot\left(\boldsymbol{a}_\times-\frac{\boldsymbol{k}\otimes\boldsymbol{a}}{2}\right)\cdot\delta_2\boldsymbol{b}\right)-\frac{\delta_2\boldsymbol{b}\otimes\delta_1\boldsymbol{b}}{2}\cdot\boldsymbol{k}\,.\end{aligned}$$

In view of equation (A.5), we can obtain the second-order infinitesimal rotation vector by symmetrizing this with respect to the increments $\delta_1\boldsymbol{b}$ and $\delta_2\boldsymbol{b}$:

$$\begin{aligned}\delta_{12}\hat{\boldsymbol{p}}_a^{\boldsymbol{b}} &= \tfrac{\delta_2(\delta_1\hat{\boldsymbol{p}}_a^{\boldsymbol{b}})+\delta_1(\delta_2\hat{\boldsymbol{p}}_a^{\boldsymbol{b}})}{2}\\&= \left(\boldsymbol{b}_\times-\tfrac{\boldsymbol{b}\otimes\boldsymbol{k}}{2}\right)\cdot\delta_{12}\boldsymbol{b}+\left(\delta_1\boldsymbol{b}\cdot\tfrac{\boldsymbol{k}\otimes\boldsymbol{a}+\boldsymbol{a}\otimes\boldsymbol{k}}{4\,(1+\boldsymbol{a}\cdot\boldsymbol{b})}\cdot\delta_2\boldsymbol{b}\right)\boldsymbol{b}-\tfrac{(\delta_1\boldsymbol{b}\otimes\delta_2\boldsymbol{b}+\delta_2\boldsymbol{b}\otimes\delta_1\boldsymbol{b})}{2}\cdot\tfrac{\boldsymbol{k}}{2}\,.\end{aligned}\tag{A.11}$$

Application to a Discrete elastic rod

In a Discrete elastic rod, the transport is from the undeformed tangent $\boldsymbol{a}=\boldsymbol{T}^i$ to the deformed tangent $\boldsymbol{b}=\boldsymbol{t}^i$, see equation (4.12). Equation (A.7) then yields the definition of the binormal $\boldsymbol{k}^i$ announced in equation (4.25), and equation (A.9) yields the expression for $\delta\hat{\boldsymbol{p}}^i$ announced in equation (4.23). In equation (A.11), condensing the independent variations as $\delta_1\boldsymbol{b}=\delta_2\boldsymbol{b}=\delta\boldsymbol{t}^i$ and identifying $\delta_{12}\hat{\boldsymbol{p}}_a^{\boldsymbol{b}}=\delta^2\hat{\boldsymbol{p}}^i$ and $\delta_{12}\boldsymbol{b}=\delta^2\boldsymbol{t}^i$ yields the expression of $\delta^2\hat{\boldsymbol{p}}^i$ announced in equation (4.23).

Variation of unit tangents

With $\boldsymbol{E}^i=\boldsymbol{x}_{i+1}-\boldsymbol{x}_i$ as the segment vector, the variation of the unit tangent $\boldsymbol{t}^i=\boldsymbol{E}^i/|\boldsymbol{E}^i|$ from equation (4.9) writes

$$\begin{aligned}\delta\boldsymbol{t}^i &= \tfrac{\delta\boldsymbol{E}^i}{|\boldsymbol{E}^i|}-\boldsymbol{E}^i\tfrac{\delta(|\boldsymbol{E}^i|)}{|\boldsymbol{E}^i|^2}\\&= \tfrac{\delta\boldsymbol{E}^i}{|\boldsymbol{E}^i|}-\boldsymbol{E}^i\tfrac{(\boldsymbol{E}^i\cdot\delta\boldsymbol{E}^i)}{|\boldsymbol{E}^i|^3}\\&= \tfrac{\boldsymbol{I}-\boldsymbol{t}^i\otimes\boldsymbol{t}^i}{|\boldsymbol{E}^i|}\cdot\delta_1\boldsymbol{E}^i,.\end{aligned}$$

With $\delta\boldsymbol{E}^i=\delta\boldsymbol{x}_{i+1}-\delta\boldsymbol{x}_i$, this is the expression of the first variation announced in equation (4.22).

Next, the second variation is calculated as

$$\delta_{12}\boldsymbol{t}^i=\left(-\frac{\delta_2\boldsymbol{t}^i\otimes\boldsymbol{t}^i+\boldsymbol{t}^i\otimes\delta_2\boldsymbol{t}^i}{|\boldsymbol{E}^i|}-\frac{(\boldsymbol{I}-\boldsymbol{t}^i\otimes\boldsymbol{t}^i)}{|\boldsymbol{E}^i|^2}\,\frac{\boldsymbol{E}^i\cdot\delta_2\boldsymbol{E}^i}{|\boldsymbol{E}^i|}\right)\cdot\delta_1\boldsymbol{E}^i.$$

Here, we have used $\delta_{12}\boldsymbol{E}^i=\boldsymbol{0}$ since $\boldsymbol{E}^i=\boldsymbol{x}_{i+1}-\boldsymbol{x}_i$ depends linearly on the degrees of freedom. Inserting the expression of the first variations from equation (4.22), the second variation $\delta_{12}\boldsymbol{t}^i$ can be rewritten as

$$\begin{aligned}
\delta_{12}\boldsymbol{t}^i &= \left(-\frac{((\boldsymbol{I}-\boldsymbol{t}^i\otimes\boldsymbol{t}^i)\cdot\delta_2\boldsymbol{E}^i)\otimes\boldsymbol{t}^i+\boldsymbol{t}^i\otimes((\boldsymbol{I}-\boldsymbol{t}^i\otimes\boldsymbol{t}^i)\cdot\delta_2\boldsymbol{E}^i)}{|\boldsymbol{E}^i|^2} - \frac{(\boldsymbol{I}-\boldsymbol{t}^i\otimes\boldsymbol{t}^i)}{|\boldsymbol{E}^i|^2}\boldsymbol{t}^i\cdot\delta_2\boldsymbol{E}^i\right)\cdot\delta_1\boldsymbol{E}^i \\
&= -\frac{\tau^i_{IKJ}+\tau^i_{JKI}+\tau^i_{IJK}}{|\boldsymbol{E}^i|^2}\,(\delta_1E^i)_J\,(\delta_2E^i)_K\,\boldsymbol{e}_I \\
&= -\frac{((\boldsymbol{\tau}^i)^{T(132)}+(\boldsymbol{\tau}^i)^{T(231)}+\boldsymbol{\tau}^i)_{IJK}}{|\boldsymbol{E}^i|^2}\,(\delta_1E^i)_J\,(\delta_2E^i)_K\,\boldsymbol{e}_I \\
&= -\frac{\boldsymbol{\tau}^i+(\boldsymbol{\tau}^i)^{T(132)}+(\boldsymbol{\tau}^i)^{T(231)}}{|\boldsymbol{E}^i|^2} : ((\delta_1\boldsymbol{x}_{i+1}-\delta_1\boldsymbol{x}_i)\otimes(\delta_2\boldsymbol{x}_{i+1}-\delta_2\boldsymbol{x}_i)),
\end{aligned}$$

where the third-order tensor $\boldsymbol{\tau}^i = (\boldsymbol{I}-\boldsymbol{t}^i\otimes\boldsymbol{t}^i)\otimes\boldsymbol{t}^i$ and its generalized transpose are defined below equation (4.22). The expression of $\delta^2\boldsymbol{t}^i$ announced in equation (4.22) is obtained by condensing $\delta_1\boldsymbol{x}_i = \delta_2\boldsymbol{x}_i = \delta\boldsymbol{x}_i$ and identifying $\delta^2\boldsymbol{t}^i = \delta_{12}\boldsymbol{t}^i$.

Variation of directors rotation

In view of equation (A.4), the infinitesimal rotation vector $\delta\hat{\boldsymbol{d}}^i$ associated with the directors rotation d^i is

$$\delta\hat{\boldsymbol{d}}^i = 2\,\delta d^i\,\overline{d}^i.$$

Differentiating the expression of d^i from equation (4.11), we have $\delta d^i = \delta\left(p^i\,r_{\boldsymbol{T}^i}(\varphi^i)\,D^i\right) = \delta p^i\,r_{\boldsymbol{T}^i}(\varphi^i)\,D^i + p^i\,\delta(r_{\boldsymbol{T}^i}(\varphi^i))\,D^i$. Equation (4.5) shows that, with a fixed unit vector $\boldsymbol{T}^i$, $\delta(r_{\boldsymbol{T}^i}(\varphi^i)) = \frac{1}{2}\left[\delta\varphi^i\,\boldsymbol{T}^i\right]\,r_{\boldsymbol{T}^i}(\varphi^i)$—here, the vector in square bracket is an infinitesimal rotation vector, see equation (A.4). This yields $\delta d^i = \delta p^i\,r_{\boldsymbol{T}^i}(\varphi^i)\,D^i + \frac{1}{2}\,p^i\,\delta\varphi^i\,\boldsymbol{T}^i\,r_{\boldsymbol{T}^i}(\varphi^i)\,D^i$. Inserting into the equation above, and using $\overline{d}^i = \overline{D}^i\,r_{\boldsymbol{T}^i}(-\varphi^i)\,\overline{p}^i$ from equation (4.11), we find

$$\begin{aligned}
\delta\hat{\boldsymbol{d}}^i &= \delta\varphi^i\,p^i\,\boldsymbol{T}^i\,r_{\boldsymbol{T}^i}(\varphi^i)\,D^i\,\overline{d}^i + 2\,\delta p^i\,r_{\boldsymbol{T}^i}(\varphi^i)\,D^i\,\overline{d}^i \\
&= \delta\varphi^i\,p^i\,\boldsymbol{T}^i\,\overline{p}^i + 2\,\delta p^i\,\overline{p}^i \\
&= \delta\varphi^i\,p^i * \boldsymbol{T}^i + \delta\hat{\boldsymbol{p}}^i \\
&= \delta\varphi^i\,\boldsymbol{t}^i + \delta\hat{\boldsymbol{p}}^i,
\end{aligned}$$

as announced in equation (4.26).

The second-order infinitesimal rotation vector is then obtained from equation (A.5) as

$$\begin{aligned}
\delta_{12}\hat{\boldsymbol{d}}^i &= \frac{1}{2}\left(\delta_2\left(\delta_1\varphi^i\,\boldsymbol{t}^i+\delta_1\hat{\boldsymbol{p}}^i\right)+\delta_1\left(\delta_2\varphi^i\,\boldsymbol{t}^i+\delta_2\hat{\boldsymbol{p}}^i\right)\right) \\
&= \frac{\delta_1\varphi^i\,\delta_2\boldsymbol{t}^i+\delta_2\varphi^i\,\delta_1\boldsymbol{t}^i}{2}+\delta_{12}\hat{\boldsymbol{p}}^i.
\end{aligned}$$

Here, we have used $\delta_{12}\varphi^i = 0$ as φ^i is a degree of freedom and the variations $\delta_1\varphi^i$ and $\delta_2\varphi^i$ are independent.

Upon condensation of the two variations, the equation leads to the expression of $\delta^2\hat{\boldsymbol{d}}^i$ announced in equation (4.26).

Rotation gradient

In view of equation (A.4), the infinitesimal rotation vector $\delta\hat{\boldsymbol{q}}_i$ associated with the rotation gradient $q_i = \overline{d^{i-1}}d^i$ from equation (4.14) writes

$$\begin{aligned}\delta\hat{\boldsymbol{q}}_i &= 2\,\delta q_i\,\overline{q_i} \\ &\quad \left(\overline{2\,\delta d^{i-1}}\,d^i + \overline{d^{i-1}}\,2\,\delta d^i\right)\,\overline{q_i} \\ &= \overline{d^{i-1}}\,(-\delta\hat{\boldsymbol{d}}^{i-1} + \delta\hat{\boldsymbol{d}}^i)\,d^{i-1}\end{aligned}$$

as announced in equation (4.27).

The following identity yields the variation of the vector $\overline{s} * \boldsymbol{u}$ obtained by applying the inverse $\overline{s}$ of a rotation s to a vector $\boldsymbol{u}$,

$$\begin{aligned}\delta(\overline{s} * \boldsymbol{u}) &= \delta\,(\overline{s}\,\boldsymbol{u}\,s) \\ &= \overline{\delta s}\,\boldsymbol{u}\,s + \overline{s}\,\boldsymbol{u}\,\delta s + \overline{s}\,\delta\boldsymbol{u}\,s \\ &= \tfrac{-\overline{s}\,\delta\hat{\boldsymbol{s}}\,\boldsymbol{u}\,\overline{s}+\overline{s}\,\boldsymbol{u}\,\delta\hat{\boldsymbol{s}}\,s}{2} + \overline{s} * \delta\boldsymbol{u} \\ &= \tfrac{-(\overline{s}*\delta\hat{\boldsymbol{s}})\,(\overline{s}*\boldsymbol{u})+(\overline{s}*\boldsymbol{u})\,(\overline{s}*\delta\hat{\boldsymbol{s}})}{2} + \overline{s} * \delta\boldsymbol{u} \\ &= -(\overline{s} * \delta\hat{\boldsymbol{s}}) \times (\overline{s} * \boldsymbol{u}) + \overline{s} * \delta\boldsymbol{u}.\end{aligned}$$

With $\delta = \delta_1$, $s = d^{i-1}$ and $\boldsymbol{u} = \delta_2\hat{\boldsymbol{d}}^i - \delta_2\hat{\boldsymbol{d}}^{i-1}$, we have $\overline{s} * \boldsymbol{u} = \overline{d^{i-1}} * (\delta_2\hat{\boldsymbol{d}}^i - \delta_2\hat{\boldsymbol{d}}^{i-1}) = \delta_2\hat{\boldsymbol{q}}_i$, see equation (4.27), and the identity above yields

$$\begin{aligned}\delta_1(\delta_2\hat{\boldsymbol{q}}_i) &= -(\overline{\overline{d^{i-1}} * \delta_1\hat{\boldsymbol{d}}^{i-1}}) \times \delta_2\hat{\boldsymbol{q}}_i + \overline{d^{i-1}} * (\delta_1(\delta_2\hat{\boldsymbol{d}}^i) - \delta_1(\delta_2\hat{\boldsymbol{d}}^{i-1})) \\ &= \overline{d^{i-1}} * (\delta_1(\delta_2\hat{\boldsymbol{d}}^i) - \delta_1(\delta_2\hat{\boldsymbol{d}}^{i-1})) + \delta_2\hat{\boldsymbol{q}}_i \times (\overline{d^{i-1}} * \delta_1\hat{\boldsymbol{d}}^{i-1})\end{aligned}.$$

Symmetrizing with respect to the independent variations δ_1 and δ_2 and using equation (A.5), we obtain the second infinitesimal vector as

$$\delta_{12}\hat{\boldsymbol{q}}_i = \overline{d^{i-1}} * \left(\delta_{12}\hat{\boldsymbol{d}}^i - \delta_{12}\hat{\boldsymbol{d}}^{i-1}\right) + \frac{\delta_1\hat{\boldsymbol{q}}_i \times (\overline{d^{i-1}} * \delta_2\hat{\boldsymbol{d}}^{i-1}) + \delta_2\hat{\boldsymbol{q}}_i \times (\overline{d^{i-1}} * \delta_1\hat{\boldsymbol{d}}^{i-1})}{2}.$$

Upon condensation of the two variations, the equation leads to the expression of $\delta^2\hat{\boldsymbol{q}}_i$ announced in equation (4.27).

Strain vector

Equation (4.16) can be rewritten as $\boldsymbol{\kappa}_i = 2\,\mathcal{I}(q_i)$, where $\mathcal{I}(q) = \frac{q-\overline{q}}{2}$ denotes the vector part of a quaternion. The operator $\mathcal{I}$ being linear, we have

$$\begin{aligned}\delta\boldsymbol{\kappa}_i &= 2\,\mathcal{I}(\delta q_i) \\ &= \mathcal{I}\left(\delta\hat{\boldsymbol{q}}_i\,q_i\right)\end{aligned}$$

as well as

$$\begin{aligned}\delta_{12}\boldsymbol{\kappa}_i &= 2\,\mathcal{I}\,(\delta_{12}q_i) \\ &= \mathcal{I}\left(\left(\delta_{12}\hat{\boldsymbol{q}}_i - \tfrac{\delta_1\hat{\boldsymbol{q}}_i\cdot\delta_2\hat{\boldsymbol{q}}_i}{2}\right)q_i\right),\end{aligned}$$

as announced in equation (4.28). In the equation above, the second variation of the unit quaternion $\delta_{12}q_i$ has been expressed using equation (A.4).

Numerical verification

We verify the gradient and Hessian of the elastic energy, by considering a Kirchhoff rod having 80 nodes. Starting from a straight rod, we increment the magnitude of the natural curvature, magnitude of gravity, and a point load applied at the ends over 100 iterations. At each iteration we compute the equilibrium, disabling the update of the reference configuration discussed in Section 4.2. This allows us to verify the gradient in the generic setting where the reference and current configurations differ significantly from each other. The computed equilibrium solution is denoted by the vector $\mathbf{X}$. We introduce a second configuration vector $\tilde{\mathbf{X}}$ by adding a random perturbation to $\mathbf{X}$ where each perturbation is chosen randomly between $(-0.1, 0.1)$. This magnitude of perturbation ensures that the configuration $\tilde{\mathbf{X}}$ is sufficienlty far from an equilibrium. By starting with the different equilibrium solutions $\mathbf{X}$, we ensure that the variations are taken at different locations in the configuration space.

The gradient of the discrete strain energy $\mathcal{E} = \sum_{i=1}^{N-1} E_i$ is evaluated at the point $\tilde{\mathbf{X}}$ either as $\nabla\mathcal{E}_a$ computed based on the analytical formula given in the main text, or as $\nabla\mathcal{E}_{fd}$ using finite differences as $(\nabla\mathcal{E}_{fd})_i = (\mathcal{E}(\tilde{\mathbf{X}} + h\mathbf{e}_i) - \mathcal{E}(\tilde{\mathbf{X}} + h\mathbf{e}_i))/2h$ where $h = 10^{-7}$ and $\mathbf{e}_i$ is a unit vector where the i^{th} component is 1.

We then calculate the relative gradient error as:

$$\|\nabla\mathcal{E}_{\text{err}}\| = \frac{\|\nabla\mathcal{E}_a - \nabla\mathcal{E}_{fd}\|_\infty}{\|\nabla\mathcal{E}_a\|_\infty}\,.$$

Similarly for the Hessian, we calculate the hessian $\nabla^2\mathcal{E}$ of the strain energy gradient at the point $\tilde{\mathbf{X}}$, either analytically ($\nabla^2\mathcal{E}_a$) using the methods described in the manuscript or using finite differences ($\nabla^2\mathcal{E}_{fd}$). We calculate $\nabla^2\mathcal{E}_{fd}$ using finite differences on the analytical form of the gradient. The relative hessian error is calculated as:

$$\|\nabla^2\mathcal{E}_{\text{err}}\| = \frac{\|\nabla^2\mathcal{E}_a - \nabla^2\mathcal{E}_{fd}\|_\infty}{\|\nabla^2\mathcal{E}_a\|_\infty}\,.$$

At every iteration, we calculate a different random perturbation and calculate the errors $\|\nabla\mathcal{E}_{\text{err}}\|$ and $\|\nabla^2\mathcal{E}_{\text{err}}\|$ at that point. The results are shown in Figure (A.3).

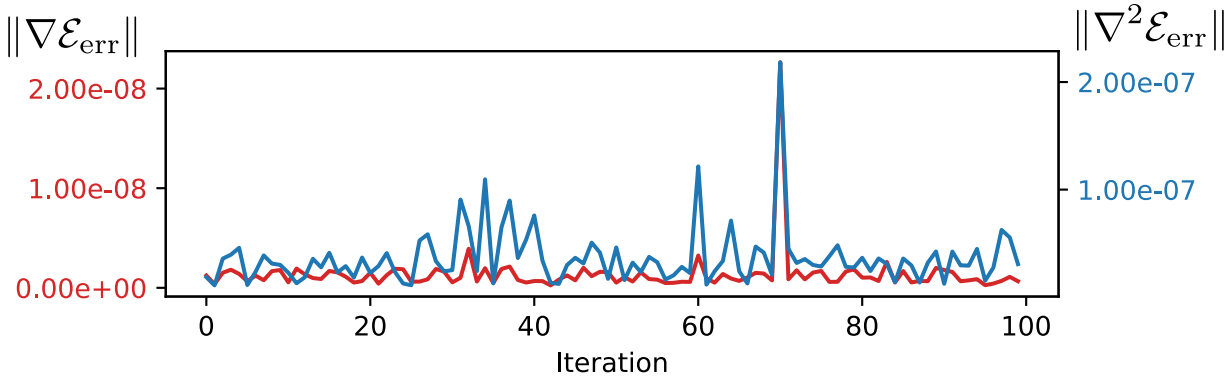

Figure A.3: Errors between the analytical and numerical calculations for gradients and hessians.

A.3 Supplement for Chapter 5

Materials and Methods

Mechanical instability in liquid crystalline elastomers

Liquid crystalline elastomers (LCEs) were prepared with spatial variation of the nematic director, described as a +1 topological defect. The brush-like pattern evident in Figure 5.1A is associated with the concentric rotation of the liquid crystalline molecules around a central point (Figure 5.1B). To introduce through-thickness variation in the timing and magnitude of stimuli-response, we laminated LCE films prepared with +1 director profiles. The laminates were prepared from 30 μm thick LCE films of two different compositions (Figure 5.1C). Stiffer LCEs were prepared by radical-mediated chain-transfer polymerization of C6M with BDMT (Figure 5.1C) in ratios of 1:0.5 acrylate:thiol. Softer LCE were prepared from a formulation mixed at 1:0.75 acrylate:thiol. The laminated elements were prepared (Figure 5.1D) by pressing LCE films together ensuring defect centers and edges of the squares were aligned. To improve adhesion between the stiff and soft LCE compositions, a thin layer of C6M and photoinitiator was applied and cured upon stacking [99]. The resulting mechanical elements prepared from the LCE layers had a stepwise variation in modulus through the thickness. In nearly all examinations detailed here, we use a three-layer laminate prepared from two of the softer 30 μm LCEs and one stiffer 30 μm LCE (Figure 5.1D).

When LCE laminates were placed with the high-modulus side down on a hot surface (160°C), the film first deformed upward into an out-of-plane dome. (Figure 5.1E,F) Subsequently, the curvature of the LCE inverts via mechanical instability resulting in a snap through deformation in the center of the element, forming an inverted

cone. The force and acceleration of this transition results in the LCE leaping from the surface in less than 6 ms, reaching a height of over 200 times the material thickness. The snap-through transition and the resulting "leap" is visualized in time sequenced images in Figure 5.1E.

To assess the distinctive stimulus response of these LCEs, we first characterized material properties in uniaxially aligned LCEs. Notably, the moduli of the LCEs parallel to the alignment was similar for the stiff (1:0.5) and soft (1:0.75) materials while the moduli in the perpendicular direction differed by a factor of 5 (Table A.1, Figure 5.2A). The variation in perpendicular modulus is particularly important, as the stimulus response of the LCE with a +1 topological defect will undergo out of plane deformation by stretching the concentrically packed mesogens along the perpendicular direction. The differences in modulus values correlate with a difference in Tg for the two compositions and both are attributable to a reduction in molecular weight between crosslinks (M_c) (Table A.1). Further, the actuation of the LCEs was characterized. Both LCEs exhibited a nematic-isotropic transition temperature (T_{ni}, Table A.1). However, the T_{ni} for the higher modulus LCE was over 50°C higher than the lower modulus LCE. Therefore, when subjected to thermal stimulus, the low modulus materials generate strain at a much faster rate than the high modulus materials for a given temperature (Figure 5.2B).

Composition (Acrylate:Thiol)	Modulus $\parallel$ (a) (MPa)	Modulus $\perp$ (a) (MPa)	M_c (b) (g/mol)	$T_{ni}(^\circ C)$ (c)	$T_g(^\circ C)$ (d)	Strain Rate at $160^\circ C$ $\parallel$ (e)
1 : 0.5	21 ± 0.6	17 ± 1	1000	> 225	22	0.05
1 : 0.75	18 ± 3	3.2 ± 0.3	4650	170	16	0.54

Table A.1: Material proerties for linearly aligned model LCE.

a Measured in linear strain $2-4\%$ of tensile curve

b Calculated using $M_c = 3RT/E'$ with E' measured at $100^\circ C$

c Calculated as inflection point of thermomechanical strain curve

d Calculated as peak of $\tan\delta$ curve

e Calculated as slope of thermomechanical strain curve from $155-165^\circ C$

Fabrication of Alignment Cells

Photopatterned cells with +1 topological defects were fabricated using glass slides coated with brilliant yellow (Sigma Aldrich). Two slides were adhered together with 30 μm glass spacers (SPI Supplies) and NOA-68 (Norland Optical Adhesives). Assembled cells were photopatterned using a 445 nm vertically polarized laser with a $q = 1/2$ waveplate (BEAM Co.) and a 7 mm square mask. Each defect was exposed for 3 minutes with laser intensity 5 mW/cm^2. Linearly aligned cells were fabricated using Elvamide-coated glass slides that were rubbed with velvet and adhered in anti-parallel alignment with NOA-68 and 30 μm glass spacers.

Synthesis of Liquid Crystalline Elastomers

Liquid crystalline polymers were synthesized using 1,4-Bis-[4-(6-acryloyloxyhexyloxy)benzoyloxy]-2-methylbenzene (C6M) (Wilshire Technologies) and benzenedimethanethiol (BDMT) (Tokyo Chemical Industry). C6M and BDMT were mixed in molar ratios (acrylate:thiol) of 1:0.5 and 1:0.75.Omnirad 819 was included (0.5 wt%) for initiation of photopolymerization. Mixtures were melted at 150°C and vortexed before capillary filling into 30 μm photopatterned +1 defect or linear alignment cells at 100°C. Once filled, cells were cooled to 30°C and held for 20 minutes to allow for alignment of liquid crystals. Materials were then photopolymerized with 365 nm light at 50 mW/cm^2 for 5 minutes and subsequently removed from cells.

Lamination

Films of equivalent modulus were laminated by stacking with defect centers aligned and pressing films together with gentle heating at 90°C. Each 7 mm defect square of contrasting modulus was placed on a glass slide and a spin coater was used to deposit C6M monomer and Omnirad 819 on the surface (60 s, 2000 rpm). C6M and Omnirad 819 were suspended in a solution of methanol and dichloromethane (5:1 MeOH:DCM, 10 mg/mL C6M, 0.25 mg/mL Omnirad 819). Coated sides of films were pressed together with defect centers aligned and the stacked films were heated at 90°C for 30 s before polymerization with 365 nm light at 50 mW/cm^2 for 1 minute. For laminated films with “legs”, small pieces of paper were cut to the appropriate size and attached to the bottom surface with Gorilla Super Glue.

Actuation

Films were placed with high modulus side in contact with a hot plate that had been preheated to $160°C$. Films were left free-standing on the hot plate until snap-through occurred. Snap-through deformations were recorded using a Photron FASTCAM SA3. Linearly aligned films were held at a constant force (0.0005 N) while temperature was ramped from $25°C$ to $225°C$ (DMA 850, TA Instruments). Strain generation was measured as a function of temperature.

Crosslink Density Measurments

Dynamic mechanical analysis was conducted on diacrylate films using an RSA-G2 DMA (TA Instruments). The temperature was ramped from -50°C to 150°C using 0.5% strain at 1 Hz frequency. T_g values were taken from the temperature corresponding to the maximum of $\tan\delta$ for the material. The molecular weight between crosslinks (M_c) was calculated using the storage modulus value of the rubbery plateau at 150°C and the equation $M_c = 3RT_d/E'$, where R is 8.314 $\mathrm{cm}^3 MPa \mathrm{mol}^{-1} K^{-1}$, T is the temperature, d is the density of the polymer network [1.2 g/cm^3 for all materials], and E' is the storage modulus at the corresponding temperature.

Tensile Measurements

Tensile tests were conducted on linearly aligned films in both parallel and perpendicular orientation relative to the alignment. Strips were cut from the material and strained at a rate of 5%/min (RSA-G2 DMA, TA Instruments). Elastic modulus was calculated from the linear region of the stress-strain curve (2-4%).